



**Self-Assembly in Metal-Organic Frameworks:
Monitoring the Established and Refining the Novel**

by

© **Amanda P. Parsons**

A thesis submitted to the School of Graduate Studies in
partial fulfillment of the requirements for the degree of
Master of Science.

Department of Chemistry

Memorial University of Newfoundland and Labrador

May 2025

St. John's, Newfoundland and Labrador

Abstract

Metal-organic frameworks (MOFs) are highly porous materials formed via the self-assembly of organic bridging ligands (linkers) to metallic nodes. The tunability and high surface areas of these crystalline materials provide them a wide range of possible applications, such as gas separation, catalysis, and drug delivery.

Despite the popularity of MOFs, the self-assembly process through which these materials form is underexplored, especially in the field of NMR spectroscopy. This is heavily owed to the high cost of the deuterated solvent found in most MOF syntheses making ^1H -NMR experiments expensive to prepare. In Chapter 2 of this work, the synthesis of a MOF called UiO-66 is followed via time-resolved in situ solution-phase ^2H -NMR spectroscopy, allowing inexpensive protonated solvents to be used. This work examines the differences in the synthesis of UiO-66 under the influence of different acidic modulators – namely, acetic acid (AA), hydrochloric acid (HCl), and benzoic acid (BA). By utilizing and following either $\text{H}_2\text{BDC-}d_4$, for information regarding linker concentration, or D_2O , for information regarding acidity and chemical exchange, defining features of the synthesis were observed. It was found that the choice of modulator had a significant effect on the behaviour of the reaction mixture in the form of producing different rate constants, different lengths of induction periods and different changes to solution acidity. The solvent appeared to participate in some syntheses far more than others, as the HCl and BA syntheses showed evidence of DMF hydrolysis, while the AA synthesis did not. It was found that thermally conditioning the solvent and modulator before the addition of the linker caused significant changes to the synthesis; it caused the rate constants for all three

syntheses to drop, but it accelerates the formation of MOF as determined by visual check. Data regarding the porosimetry of these materials was used alongside the ^2H -NMR data to create a proposed mechanism explaining this paradoxical behaviour.

New MOFs are always being developed, due in part to the ongoing invention of new organic bridging ligands. MOFs with linkers based on porphyrins are plentiful, but, despite their structural similarity to porphyrins, phthalocyanines are far less present in MOFs as linkers; this is largely due to the structural challenges associated with converting these macrocycles into symmetrical linkers. Previously in the Katz group, a new phthalocyanine linker that relied on benzimidazole groups to provide it symmetry was synthesized and incorporated into a MOF. In Chapter 3 of this work, various facets of the synthesis of a MOF with this phthalocyanine linker, called BzPcMOF in this work, are experimented with in order to enhance the replicability of the synthesis, as well as probe further the role of reagents in the synthesis. The concentration of HCl and metal salt used in the synthesis was found to have significant effects on the surface areas of MOF samples. The XRD, elemental composition, and surface area of BzPcMOF were obtained, and possible crystal structures of the MOF were explored. Investigations into the temporal and hydro stability of BzPcMOF produced intriguing results: Over time, the external surface area of samples of BzPcMOF increased significantly, with no penalty to total surface area. When one of these old samples of BzPcMOF was immersed in water, its external surface area decreased, again with no penalty to the total surface area.

Acknowledgements

None of the work contained within this thesis would have been possible without the support of others. I would first and foremost like to thank my supervisor, Dr. Michael Katz, for making research fun and rewarding. I am so lucky and so grateful to have had a supervisor who always believed in me, always spoke kindly to me, and always knew how to encourage me and inspire my curiosity. I have learned many skills and lessons in Dr. Katz's laboratory that I will carry with me for the rest of my life.

I would like to thank the other members of the Katz group for inspiring me, hyping me up, and providing me with essential guidance. Of the current members, thank you in particular to Etienne, for always making the lab feel welcoming, and to Rodney, for always making me laugh. I'd like to thank previous members of the Katz group, as well – thank you to Mason for answering all of my questions without ever making me feel stupid, and to Ellan, for inspiring me with his hard work, patience, and attention to detail. Thank you to all other current and former members of the Katz group and thank you to the future members who will continue investigating this fascinating class of porous materials.

I would like to thank my committee members, Dr. Huck Grover and Dr. Fran Kerton, for their invaluable feedback. I also offer my thanks and my deepest gratitude to Dr. Céline Schneider for her assistance with the ^2H -NMR spectroscopy that was so important to this research. Thank you as well to Dylan Goudie and Adam Beaton for their assistance with the SEM work and the TGA work, respectively.

I would like to thank the Department of Chemistry and the School of Graduate Studies for financial assistance, as well as Dr. Liqin Chen for the entrance scholarship and thesis writing scholarship. This assistance allowed me to focus on my research instead of focusing on trying to make ends meet.

I would like to thank my partner, Kaitlyn, for her unyielding well of support and compassion. I owe a great deal of my motivation to her, and her persistent belief in me, even when I was incapable of believing in myself. Thank you to my mother, Sharon, for encouraging my love of science from a young age, and thank you to my brothers, Grant and Craig, for always cheering me on.

Finally, my deepest thanks to my late father, Cyril, whose birthplace here in Newfoundland led me to Memorial University. Without his spirit guiding me, I wouldn't have met any of the fantastic folks here in St. John's, and I would have missed out on a wealth of amazing experiences.

Table of Contents

ABSTRACT	II
ACKNOWLEDGEMENTS	IV
TABLE OF CONTENTS	VI
LIST OF TABLES	X
LIST OF FIGURES	XII
LIST OF ABBREVIATIONS AND SYMBOLS	XVIII
CHAPTER 1 INTRODUCTION	1
1.1 Porous Materials.....	2
1.2 Metal-Organic Frameworks	3
1.2.1 Inorganic nodes	4
1.2.2 Organic linkers	6
1.2.3 The utility of reticular chemistry	12
1.2.4 Defects	14
1.3 MOF Synthesis.....	16
1.3.1 Modulators.....	17
1.4 Characterization/Analysis of MOFs.....	19
1.4.1 Adsorption analysis and isotherms	20
1.4.2 BET surface areas	22
1.4.3 Pore size distributions.....	25
1.4.4 Powder X-ray Diffraction.....	28
1.5 Motivation of this Thesis.....	29
STATEMENT OF CO-AUTHORSHIP	31
CHAPTER 2 EXPLORING MODULATED MECHANISM OF FORMATION OF UIO-66 VIA ²H-NMR	32
2.1 Introduction	32
2.1.1 Time-resolved ¹ H-NMR	36
2.1.2 ² H-NMR.....	39
2.1.3 UiO-66.....	40
2.1.4 Pre-conditioning reagents	42
2.1.5 Motivation of this research.....	44
2.2 Results and Discussion.....	45
2.2.1 UiO-66 characterization	45
2.2.2 ² H-NMR Linker data.....	51

2.2.2.1 ² H-NMR Linker data for UiO-66-AA	52
2.2.2.2 ² H-NMR Linker data for UiO-66-HCl	55
2.2.2.3 ² H-NMR Linker data for UiO-66-BA	57
2.2.3 Time-dependent visual inspection	58
2.2.4 D ₂ O data	64
2.2.4.1 ² H-NMR D ₂ O data for UiO-66-AA	65
2.2.4.2 D ₂ O data for UiO-66-HCl	68
2.2.4.3 D ₂ O data for UiO-66-BA	69
2.2.5 Defectivity	72
2.2.5.1 UiO-66-AA	73
2.2.5.2 UiO-66-HCl	75
2.2.5.3 UiO-66-BA	77
2.2.6 SEM	79
2.2.6.1 SEM of UiO-66-AA	79
2.2.6.2 SEM of UiO-66-HCl	81
2.2.6.3 SEM of UiO-66-BA	82
2.2.7 Reaction timelines	83
2.3 Proposed mechanisms for MOF formation	85
2.4 Conclusions	88
2.5 Experimental	89
2.5.1 Materials and methods	89
2.5.2 Synthesis of UiO-66-AA in bulk	90
2.5.2.1 Synthesis of UiO-66-AA for NMR analysis	90
2.5.3 Synthesis of UiO-66-HCl in bulk	90
2.5.3.1 Synthesis of UiO-66-HCl for NMR analysis	91
2.5.4 Synthesis of UiO-66-BA in bulk	91
2.5.4.1 Synthesis of UiO-66-BA for NMR analysis	91
2.5.5 Pre-conditioning solvent and modulator	92
2.5.6 Pre-conditioning ZrCl ₄ in solvent and modulator	92
2.5.7 High resolution ² H-NMR	93
2.5.8 Quantities of ² H reagents used	94
2.5.9 MOF activation	94
2.5.10 Nitrogen gas adsorption isotherms	95
2.5.11 Powder X-ray diffraction	95
2.5.12 Scanning electron microscopy	95
2.5.13 Thermogravimetric analysis	95
CHAPTER 3 REFINING AND EXPLORING THE SYNTHESIS OF A	
PHTHALOCYANINE MOF	96
3.1 Introduction	96
3.1.1 Porphyrins	97
3.1.2 Phthalocyanines	98
3.1.3 Phthalocyanine MOFs	100

3.1.4 Motivation of this work	105
3.2 Results and Discussion.....	107
3.2.1 Linker synthesis.....	107
3.2.2 Original Ni-BzPcMOF synthesis.....	110
3.2.3 Modified BzPcMOF synthesis.....	111
3.2.3.1 Ensuring replicability.....	112
3.2.3.2 Effects of changes to reagents	114
3.2.3.3 Effects of changes to procedure.....	117
3.2.4 MOF characterization.....	119
3.2.4.1 SEM-EDX.....	120
3.2.4.2 SEM visual assessment.....	123
3.2.4.3 PXRD.....	125
3.2.5 MOF stability.....	130
3.2.5.1 Temporal stability	131
3.2.5.2 Water stability.....	133
3.2.5.3 SEM of water stability test samples.....	138
3.3 Conclusions	141
3.4 Experimental	142
3.4.1 Materials and methods.....	142
3.4.2 Synthesis of adduct.....	142
3.4.3 Synthesis of benzimidazole	143
3.4.4 One-pot conversion of BZI to Ni-BzPcLinker	145
3.4.5 Synthesis of BzPcMOF	147
3.4.6 MOF activation.....	148
3.4.7 Gas adsorption	148
3.4.8 LDI-MS	148
3.4.9 SEM.....	149
CHAPTER 4 FUTURE WORK	150
4.1 Following MOF synthesis via ² H-NMR	150
4.1.1 Deuterated solvent	151
4.1.2 Deuterated modulator	154
4.2 Synthesizing phthalocyanine MOFs	156
4.2.1 Experiments with pre-conditioning	156
4.2.2 Alternate solvents	158
4.2.3 Growing a single crystal of MOF.....	159
REFERENCES.....	162
APPENDIX A	175
APPENDIX B	178
APPENDIX C	181

APPENDIX D..... 184

List of Tables

Table 2.1 pK _a s of the modulators explored in this work, alongside those of the protonated BDC linker and dimethylammonium.....	46
Table 2.2 Amounts and concentrations of reagents used in the synthesis of UiO-66-AA, UiO-66-HCl, and UiO-66-BA.	46
Table 2.3 BET-SA of samples of UiO-66 synthesized at 100 °C instead of the conventional 120 °C.	49
Table 2.4 BET-SA of samples of UiO-66 made via the synthesis with pre-conditioned ZrCl ₄ in DMF and modulator.....	51
Table 2.5 Summary of kinetic data for H ₂ BDC consumption in UiO-66-AA.....	53
Table 2.6 Summary of kinetic data for H ₂ BDC consumption in UiO-66-HCl.....	55
Table 2.7 Summary of kinetic data for H ₂ BDC consumption in UiO-66-BA.....	58
Table 3.1 BET-SA of samples of BzPcMOF made under the same conditions using the “4 drops” method of HCl addition.....	112
Table 3.2 BET-SA of samples of BzPcMOF made under the same conditions using the new method of HCl addition.	113
Table 3.3 Percent changes to surface area of samples of BzPcMOF under the effects of various changes to the reagents used in the synthesis.....	114
Table 3.4 Percent changes to surface area of samples of BzPcMOF made with various changes to the synthesis procedure.	117
Table 3.5 Average % compositions of elements in samples of BzPcMOF synthesized with varying amounts of ZrCl ₄	121

Table 3.6 Surface areas of a sample of BzPcMOF before and after it sat on the lab bench in a sealed vial for 6 months.	132
Table 3.7 Surface areas of a sample of fresh BzPcMOF before and after it was submerged in distilled water overnight.	134
Table 3.8 Surface areas of a sample of old BzPcMOF before and after it was submerged in distilled water for 1 week.....	136

List of Figures

Figure 1.1 Illustration of how a specific volume of material can have different external surface areas depending on how the volume is divided.....	1
Figure 1.2 Examples of how nodes and linker with various levels of connectivity can comprise different MOFs.....	4
Figure 1.3 Common inorganic nodes found in MOFs.....	5
Figure 1.4 The 1,4-benzenedicarboxylate dianion.....	7
Figure 1.5 BDC ²⁻ , BPDC ²⁻ , and TPDC ²⁻	7
Figure 1.6 The octahedral pore of UiO-66, UiO-67, and UiO-68.	8
Figure 1.7 NH ₂ -BDC ²⁻ , OH-BDC ²⁻ , and NO ₂ -BDC ²⁻	9
Figure 1.8 BTC ³⁻ , 1,3,5-tris(4-carboxyphenyl)benzene ³⁻	10
Figure 1.9 Three different organic linkers seen in MOFs with their sturdy cores and attachment points highlighted.	11
Figure 1.10 The linkers used in NU-109 and NU-110.....	12
Figure 1.11 The eight-connected clusters found in the Zn ₂ M family of MOFs.	13
Figure 1.12 Crystal structures of examples of a MOF with various defects.....	14
Figure 1.13 Common modulators used in MOF synthesis.	17
Figure 1.14 Examples of the two isotherm types that appear in this work.	21
Figure 1.15 Two simulated isotherms for a porous material, simulated isotherm for material with a 50/50 mixture of 2 pores, and simulated isotherms for material with varying ratios of 2 pores.....	26

Figure 1.16 A representation of how the experimental isotherm and theoretical isotherms are both used to calculate the PSD of the material.	27
Figure 1.17 Simulated pore size distributions of a porous material.	28
Figure 2.1 Crystal structure of UiO-66 presented to highlight the octahedral pore and tetrahedral pore.	41
Figure 2.2 Hydrolysis of DMF into formic acid and dimethylamine.	43
Figure 2.3 Powder X-ray diffractograms of UiO-66-AA and UiO-66-BA.	48
Figure 2.4 Powder X-ray diffractograms of UiO-66 synthesized using pre-conditioned ZrCl ₄ in DMF and modulator.....	50
Figure 2.5 Concentration of linker over time for various UiO-66-AA syntheses.	52
Figure 2.6 Concentration of linker over time for various UiO-66-HCl syntheses.	55
Figure 2.7 Concentration of linker over time for various UiO-66-BA syntheses.....	57
Figure 2.8 Photo images taken at intervals during the synthesis of UiO-66-AA under various conditions.	59
Figure 2.9 Photo images taken at intervals during the synthesis of UiO-66-AA with pre-conditioned ZrCl ₄ in DMF and AA under various headspace volumes.....	60
Figure 2.10 Photo images taken at intervals during the synthesis of UiO-66-HCl under various conditions.	61
Figure 2.11 Photo images taken at intervals during the synthesis of UiO-66-BA under various conditions.	62
Figure 2.12 FWHM of D ₂ O peak over time for UiO-66-AA experiments.	65
Figure 2.13 Chemical shift of D ₂ O peak over time for UiO-66-AA experiments.....	67

Figure 2.14 Chemical shift of D ₂ O peak over time for UiO-66-HCl experiments.	68
Figure 2.15 FWHM of D ₂ O peak over time for UiO-66-HCl experiments.	69
Figure 2.16 FWHM of D ₂ O peak over time for UiO-66-BA experiments.	70
Figure 2.17 Chemical shift of D ₂ O peak over time for UiO-66-BA experiments.	71
Figure 2.18 Pore size distribution for UiO-66-AA.	73
Figure 2.19 TGA of samples of UiO-66-AA.	74
Figure 2.20 Pore size distribution for UiO-66-HCl.	75
Figure 2.21 TGA of samples of UiO-66-HCl.	76
Figure 2.22 Pore size distribution for UiO-66-BA.	77
Figure 2.23 TGA of samples of UiO-66-BA.	78
Figure 2.24 Various SEM images of UiO-66-AA.	80
Figure 2.25 Various SEM images of UiO-66-HCl.	81
Figure 2.26 Various SEM images of UiO-66-BA.	82
Figure 2.27 A timeline summarizing the collected data regarding the standard synthesis of UiO-66-AA.	83
Figure 2.28 A timeline summarizing the collected data regarding the standard synthesis of UiO-66-HCl.	84
Figure 2.29 A timeline summarizing the collected data regarding the standard synthesis of UiO-66-BA.	85
Figure 2.30 Schematic of the proposed mechanisms for the formation of UiO-66 under the standard synthesis conditions.	85

Figure 2.31 Schematic of the proposed mechanisms for the formation of UiO-66 when the ZrCl ₄ has been pre-conditioned in DMF and modulator.	86
Figure 3.1 Metal-free porphine, the simplest porphyrin.	97
Figure 3.2 Two porphyrinic pro-linkers used in MOFs.	98
Figure 3.3 The chemical structures of the phthalocyanines used to give pigment to the oil paint colours known as phthalo blue and phthalo green.	99
Figure 3.4 Tetrakis (4-carboxyphenyl) porphyrin, a common porphyrinic linker, and a typical phthalocyanine.	101
Figure 3.5 The two existing phthalocyanine-based linkers that have appeared in MOFs in the literature.	103
Figure 3.6 The phthalocyanine linker synthesized by Dr. Shayan during his PhD.	104
Figure 3.7 The porphyrinic linker used in PCN-222 and the phthalocyanine linker synthesized by Dr. Shayan.	105
Figure 3.8 Synthesis roadmap of the Ni-BzPcLinker.	108
Figure 3.9 LDI mass spectrum of Ni-BzPcMOF.	109
Figure 3.10 Appearance of samples of BzPcMOF made in different solvents.	116
Figure 3.11 The sample of BzPcMOF made with 41.2 eq of ZrCl ₄ , as analyzed with SEM-EDX.	120
Figure 3.12 SEM images of BzPcMOF synthesized in different solvents viewed at 50× magnification.	124
Figure 3.13 SEM images of BzPcMOF synthesized in different solvents viewed at 150× magnification.	124

Figure 3.14 Hydrolysis of DMAc into acetic acid and dimethyl amine.	125
Figure 3.15 Powder X-ray diffractogram of BzPcMOF.	126
Figure 3.16 Experimental PXRDs of BzPcMOF compared against simulated diffractograms of MOF topologies containing the BzPcLinker.	128
Figure 3.17 Nitrogen gas adsorption isotherms of a sample of BzPcMOF before and after it sat on the lab bench in a sealed vial for 6 months.	131
Figure 3.18 PSDs of a sample of BzPcMOF before and after it sat on the lab bench in a sealed vial for 6 months.	132
Figure 3.19 Nitrogen gas adsorption isotherms for samples of freshly made BzPcMOF before and after being submerged in distilled water overnight.....	133
Figure 3.20 PSDs of a sample of BzPcMOF before and after it was exposed to distilled H ₂ O overnight.	135
Figure 3.21 Nitrogen gas adsorption isotherms for a sample of aged BzPcMOF before and after being submerged in distilled water for 1 week.....	136
Figure 3.22 PSDs of a sample of aged BzPcMOF before and after it was exposed to distilled H ₂ O for a week.....	137
Figure 3.23 SEM images taken at 50× magnification of a 6 month old sample of BzPcMOF before and after it was submerged in water for a week.	138
Figure 3.24 SEMs at 200× magnification of a 6 month old sample of BzPcMOF before and after it was submerged in water for a week.	139
Figure 3.25 SEM images of various samples of BzPcMOF at 100× magnification.	140

Figure 4.1 Relative DMF concentrations over time in various UiO-66 standard syntheses for UiO-66-AA, UiO-66-HCl, and UiO-66-BA.	152
Figure 4.2 Stacked ^2H -NMR spectra of the methyl- d_3 peaks of DMF- d_7 from the standard syntheses of UiO-66-AA, UiO-66-HCl, and UiO-66-BA.	153
Figure 4.3 Concentrations of modulator in the standard synthesis of UiO-66.	154
Figure 4.4 From left to right: <i>N,N</i> -dimethylformamide (DMF), <i>N,N</i> -dimethylacetamide (DMAc), <i>N,N</i> -dimethylnonanamide, <i>N,N</i> -dimethyldecanamide.	158

List of Abbreviations and Symbols

Abbreviation/Symbol	Meaning
AA	acetic acid
BA	benzoic acid
BET	Brunauer-Emmett-Teller
BZI	benzimidazole
D ₂ O	deuterium oxide
DBU	1,8-diazabicyclo(5.4.0)undec-7-ene
DFT	density functional theory
DMAc	<i>N,N</i> -dimethylacetamide
DMF	<i>N,N</i> -dimethylformamide
DMSO	dimethylsulfoxide
EDX	energy dispersive X-ray spectroscopy
FA	formic acid
FWHM	full width at half maximum
¹ H	protium
² H	deuterium
H ₂ BDC	1,4-benzenedicarboxylic acid

Abbreviation/Symbol	Meaning
HCl	hydrochloric acid
HOF	hydrogen-bonded organic framework
HWHM	half width at half maximum
Hz	hertz
LDI-MS	laser desorption ionization mass spectrometry
MOF	metal-organic framework
Me	methyl
NMP	<i>N</i> -methyl-2-pyrrolidone
NMR	nuclear magnetic resonance
Pc	phthalocyanine
PcMOF	phthalocyanine metal-organic framework
Ph	phenyl
ppm	parts per million
PSD	pore size distribution
PXRD	powder X-ray diffraction
SBU	secondary building unit
SEM	scanning electron microscopy

Abbreviation/Symbol	Meaning
SSA	specific surface area
THF	tetrahydrofuran
TMSP- <i>d</i> ₄	sodium 3-trimethylsilylpropionate-2,2,3,3- <i>d</i> ₄

Chapter 1

Introduction

The importance of surfaces in chemistry cannot be overstated¹ – they're the critical starting point for all chemical processes. The efficacy of a solid heterogeneous catalyst, when interacting with a dissolved reagent, is limited by the number of reactive sites on its surface.² The more adsorption sites there are on the catalyst, the more sites that reagents can bind to, which, in turn, leads to a higher reaction rate.³ This is why solid catalysts typically undergo grinding or other forms of dispersion before they are employed in a reaction mixture; a fine dispersal of small particles will provide more surface area than one large particle (Figure 1.1).⁴ With this in mind, methods of increasing surface area or methods of designing materials with a large amount of surface area are critical for various applications.

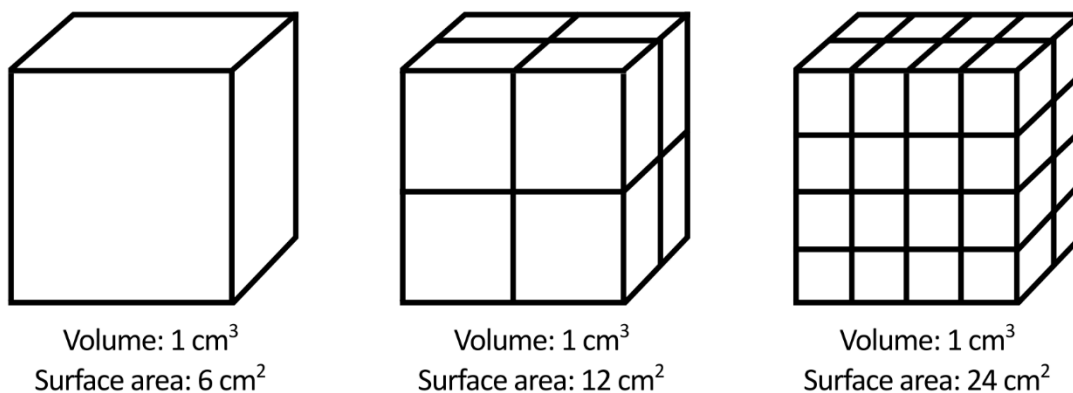


Figure 1.1 Illustration of how a specific volume of material can have different external surface areas depending on how the volume is divided.

As mentioned above, adsorption refers to the process by which molecules from a gas or liquid phase adhere (either physically or chemically) to the surface of a solid. The gas/liquid undergoing adsorption is the adsorbate, and the solid that it is adhering to is the adsorbent. Adsorption is a highly desirable process in many fields of study and industry.⁵ By exploiting a molecule's preference to adhere to some surfaces more than others, many processes can be enhanced, such as the safer storage of gases,⁶ the removal of contaminants like heavy metals from waterways,⁷ or the capture of water from air.⁸ Naturally, as adsorption is a surface phenomenon, a material's capacity for adsorption is related to the surface area of that material. That is, all else being equal, more surface permits more adsorption.

1.1 Porous Materials

When adsorption is a primary goal of a material, it follows that there is incentive to seek ways to maximize the surface area of that material.⁹⁻¹² The natural first instinct when increasing surface area is to minimize the particle size of the material. This maximizes the particle's surface area-to-volume ratio, but there is a risk that the physical properties of the material will change as the particle dimensions approach the nanometer scale.¹³ This is one of the reasons that solution-based homogeneous catalysts are so effective – they are the natural “limit” of grinding as they ideally exist as single molecules in solution. These solution-based homogeneous catalysts, however, are much harder to isolate and recover once they have served their purpose, making them poor options for large-scale use.

If we want the best of both worlds – the recoverability of a heterogeneous catalyst and the reactivity of a homogeneous catalyst – we must look for ways to add surface area to heterogeneous particles without changing their size. One must ask themselves at this point: “Where can we possibly generate more surface area?”. The answer lies within the particles, in the form of internal surface area. By creating voids within the particles, pores are formed, allowing the external dimensions of a material to remain the same while surface area increases. Such porous materials have been developed through many synthetic means and cover a wide range of applications. Among these porous materials are zeolites,¹⁴ activated carbon,¹⁵ and metal-organic frameworks (MOFs).¹⁶

1.2 Metal-Organic Frameworks

MOFs are a class of porous materials that are rapidly gaining interest. Since the advent of the millennium, these materials have steadily produced an increasing amount of literature as scientists uncover the complexities in their nature and the opportunities they provide therein.^{16–18}

MOFs are unique among porous materials in that they are made up of inorganic metal components (nodes; spheres in Figure 1.2) that are connected to one another by way of organic bridging ligands (linkers; Figure 1.2). Most often, these components form a crystalline structure that maintains open voids in the space between linkers and nodes. These open spaces (i.e., pores) are what afford MOFs their high surface area; the theoretical upper limit to MOF surface area is estimated to be 14600 m²/g,¹⁹ but most MOFs have surface areas between 500 and 3000 m²/g.²⁰

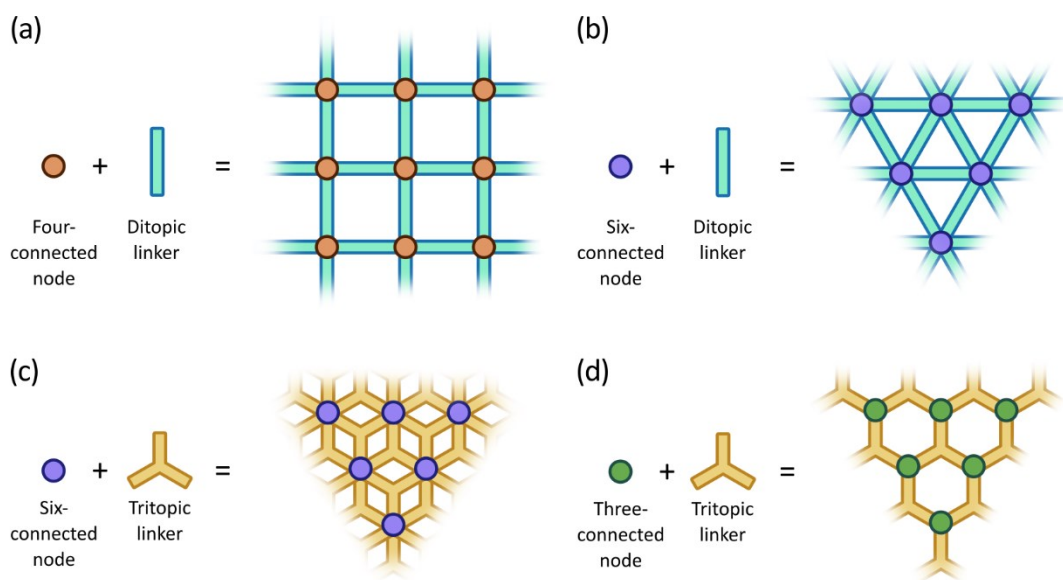


Figure 1.2 Examples of how nodes and linker with various levels of connectivity can comprise different MOFs. These are 2-dimensional illustrations for clarity, but MOFs are often 3-dimensional. (a) A four-connected node and a ditopic linker, (b) A six-connected node and a ditopic linker, (c) A six-connected node and a tritopic linker, (d) A three-connected node and a tritopic linker.

1.2.1 Inorganic nodes

The inorganic nodes in MOFs can be as simple as a single metal atom such as Cd^{2+} (Figure 1.3 (a)), or as complex as a zirconium cluster such as $[\text{Zr}_6\text{O}_4(\text{OH})_4]^{12+}$ (Figure 1.3 (d)). These nodes can be defined by the number of linkers that can attach to them; in this regard, $[\text{Zr}_6\text{O}_4(\text{OH})_4]^{12+}$ is a twelve-connected node as twelve linkers can connect to it. By far the most popular elements found in these inorganic nodes are d-block metals. Of the d-block metals, Zn(II) can be considered a pioneer in the field of MOF chemistry due to its early ubiquity and inclusion in crucial MOFs such as MOF-5,²¹ considered one of the earliest MOFs. Zn(II) can often be found in the form of a six-connected Zn_4O cluster (Figure 1.3 (c)), but it is also found as a four-connected node in non-cluster based MOFs such as

zeolitic imidazolate frameworks,²² (ZIFs) or as a chain-like node in MOF-74.²³ Although MOF-5 has had enormous success in pioneering gas adsorption properties in MOFs, its Zn-O bonds have been found to be susceptible to hydrolysis.²⁴ From an application point of view, the stability of MOF-5 with regard to water is poor, thereby limiting its real-world utilization; this is not to say that there is no value in studying MOF-5.²⁵

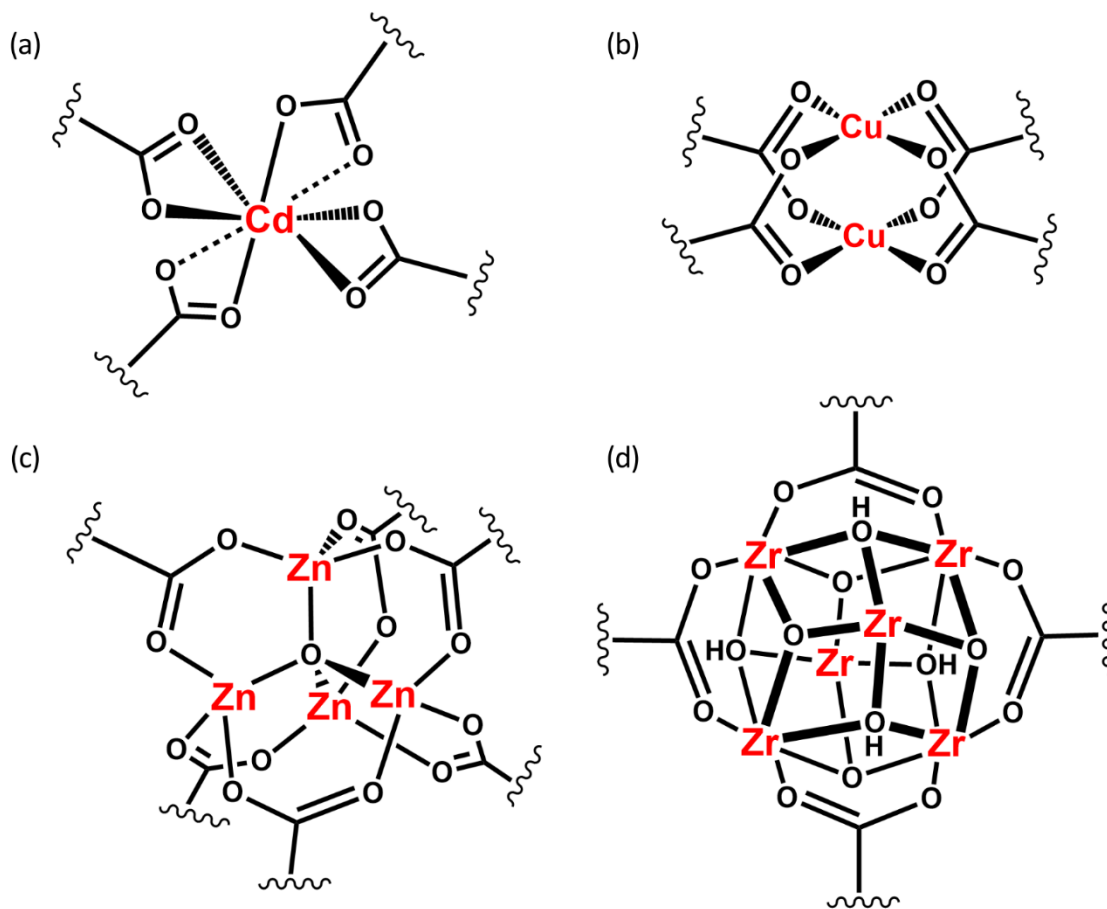


Figure 1.3 Common inorganic nodes found in MOFs. (a) a four-connected Cd(II) node, (b) a four-connected Cu₂ paddlewheel node, (c) a six-connected Zn₄O⁶⁺ node, (d) a twelve-connected [Zr₆O₄(OH)₄]¹²⁺ node; only four of the twelve linkers are shown.

Several approaches have been taken to address the stability issues related to the use of Zn and other metals that readily undergo hydrolysis in solution or under high relative humidity levels. One of the best solutions to the hydrolysis problem is the usage of group 4 metals. Group 4 metals such as zirconium, hafnium, and titanium have high charges, are extremely oxophilic, and have been observed in large coordination numbers. This often leads to high-nuclearity systems with strong M-O bonds, which have been observed to inhibit node-linker hydrolysis.^{26,27} Additionally, due to the oxophilic nature of these nodes, MOFs made with these metals often contain linkers with carboxylate groups. This can be seen in the wide variety of MOFs with Zr-containing nodes and carboxylate-containing linkers, such as, but not limited to, UiO-66,²⁸ PCN-222,²⁹ NU-1000,³⁰ and MOF-808.³¹ Zr-containing MOFs often fare much better in the presence of water than Zn-containing MOFs (though not without limit), thus providing them a wider potential range of applications.

1.2.2 Organic linkers

The organic linkers used to connect a MOF's inorganic nodes require two key characteristics to function effectively. The first is a sturdy core, and the second is the symmetric distribution of attachment sites around the core. The sturdy core is necessary for structural rigidity; this allows predictable behaviour of the linker in MOF formation. The attachment sites are necessary to connect nodes to one another, allowing the formation of the crystalline MOF.

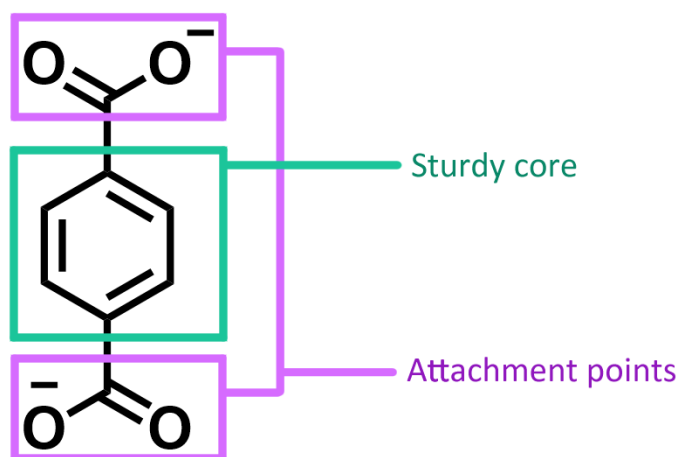


Figure 1.4 The 1,4-benzenedicarboxylate dianion (BDC^{2-}) pictured with its sturdy core (green) and its attachment points (purple).

Perhaps the simplest and most quintessential MOF linker is 1,4-benzenedicarboxylate (BDC^{2-} , Figure 1.4). BDC^{2-} contains a sturdy phenylene core and two symmetrically distributed (para-substituted) carboxylate groups. This makes the linker a two-connected linker (ditopic) as each of the two attachment points connects to a different node. How each carboxylate connects to the node often depends on the node.

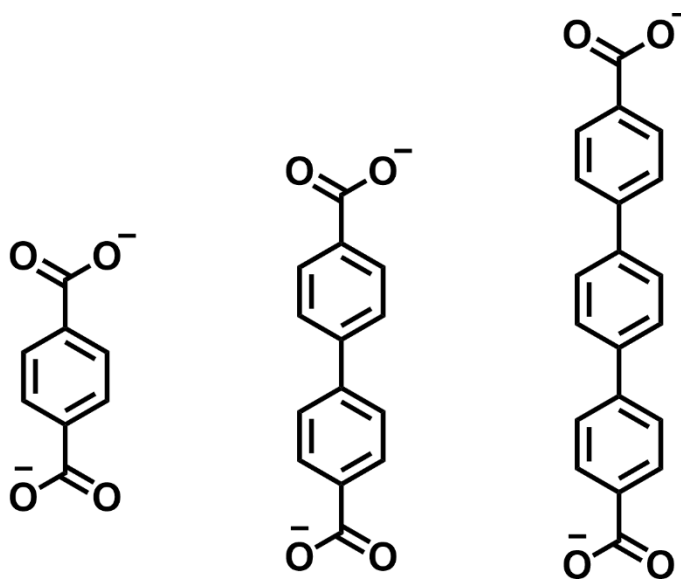


Figure 1.5 From left to right: BDC^{2-} , BPDC^{2-} , and TPDC^{2-} .

BDC^{2-} is highly successful as a linker, but it is admittedly short. This can limit the available surface area, the pore volume, or the aperture size of pores within the MOF, impacting the accessibility of its pores to various molecules. If one wanted a MOF with larger pores, one would need a longer linker. The next logical step is to elongate BDC^{2-} by adding a second phenylene ring.

This modification produces biphenyldicarboxylate (BPDC^{2-} , Figure 1.5 middle). This linker has a longer core but the same orientation and chemical composition of node attachment points. Likewise, terphenyldicarboxylate (TPDC^{2-} , Figure 1.5 right) is the extension of the BDC^{2-} core with 3 phenylene groups. In all three cases, the respective linkers are ditopic.

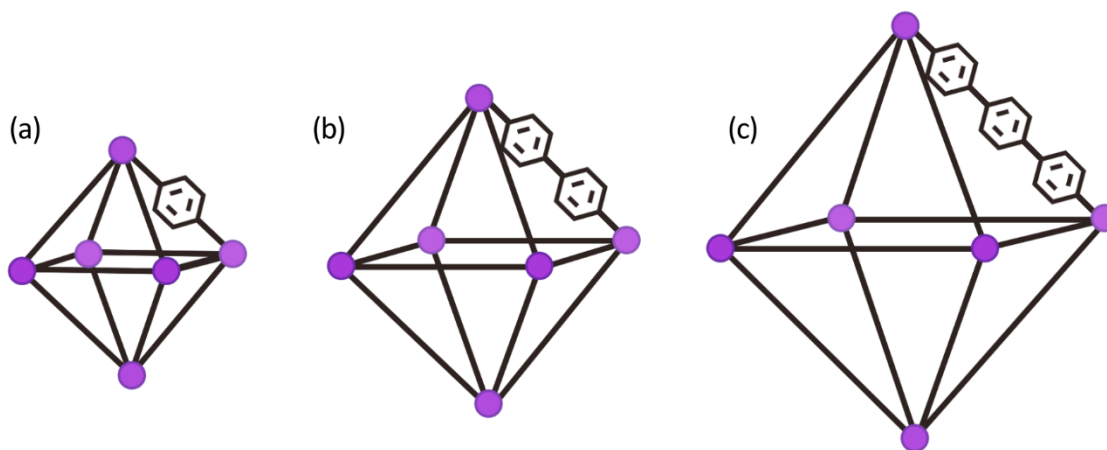


Figure 1.6 The octahedral pore of (a) UiO-66, (b) UiO-67, (c) UiO-68. Note how the nodes stay the same size in all structures, but the length of the linker changes, increasing the size of the pore.

An excellent example of how these three linkers can change a MOF is the UiO family of MOFs (Figure 1.6);³² UiO-66 will be covered more in detail in Chapter 2. UiO-66 is made

with the BDC^{2-} linker, and the size of its largest pore (i.e., its octahedral pore, seen in Figure 1.6) is 11 Å. When BPDC^{2-} is employed instead, the resulting MOF is termed UiO-67 and its largest pore size increases to 13 Å. The version that uses TPDC^{2-} is termed UiO-68, and its largest pore size is 17 Å. In all three UiOs, the topology of the MOF is the same, and only the pore size and pore aperture size change. This illustrates the isorecticular principle of MOF formation wherein MOFs can be generated with the same topological connectivity (topology) but with different pore sizes and aperture sizes that are dictated by the length of the linker.¹⁸

The carbon atoms in a phenylene ring make for excellent substitution sites, and BDC^{2-} is no different. Many derivatives exist, such as $\text{NH}_2\text{-BDC}^{2-}$, OH-BDC^{2-} , or $\text{NO}_2\text{-BDC}^{2-}$ (Figure 1.7), and naturally, if any one of these derivatives is incorporated into UiO-66, then the properties of the derivative will be imparted onto the resulting MOF. Using $\text{NH}_2\text{-BDC}^{2-}$ instead of BDC^{2-} in the synthesis of UiO-66, for example, will afford the MOF the ability to engage in hydrogen bonding via the NH_2 groups. This feature can be used to enhance adsorption in the pores,³³ or it can be used to allow MOF crystals to interact on their external surface with polymers to create strong and versatile mixed-matrix membranes.³⁴

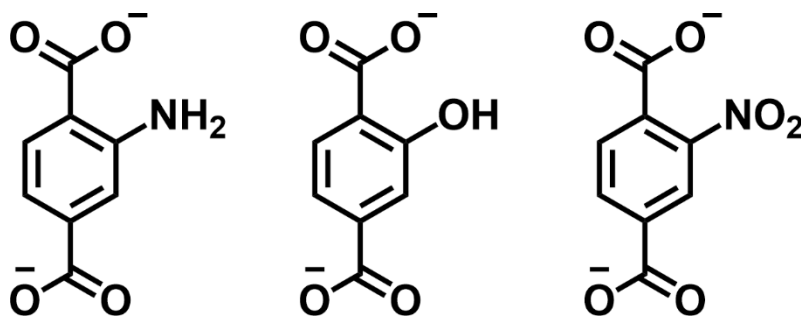


Figure 1.7 From left to right: $\text{NH}_2\text{-BDC}^{2-}$, OH-BDC^{2-} , and $\text{NO}_2\text{-BDC}^{2-}$.

Just as BDC^{2-} can have these functional groups (also called pendant groups), so too can BPDC^{2-} and TPDC^{2-} . This means that UiO-67 and UiO-68 can also benefit from the additional functionalities provided by these groups.^{35,36} Furthermore, due to the longer linker length, the pendant groups can be installed close to the node or at the centre of the linker.

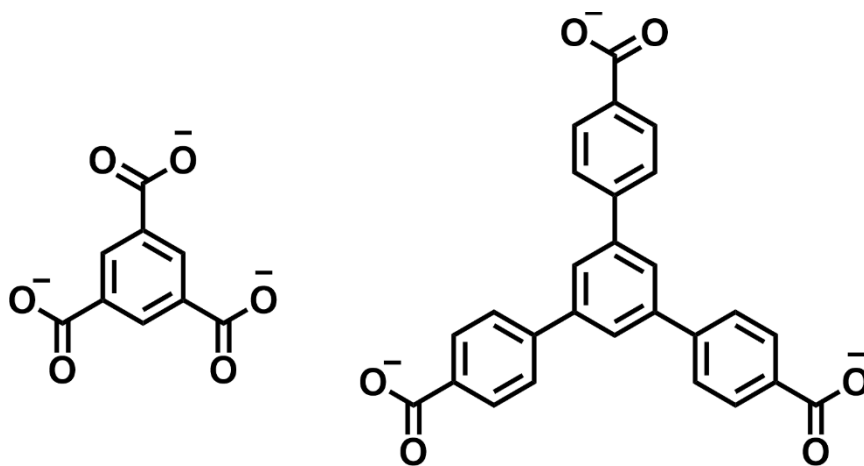


Figure 1.8 From left to right: BTC^{3-} , $1,3,5\text{-tris(4-carboxyphenyl)benzene}^{3-}$.

BDC^{2-} is just one example of how a core and its attachment groups can be altered and result in a large family of MOFs. Benzenetricarboxylate (BTC^{3-}) is a tritopic linker (Figure 1.8, left) which, like BDC^{2-} , uses a substituted benzene ring as its stable core. Its three symmetric attachment points allow it to produce MOFs with different topologies than BDC^{2-} does. BTC^{3-} , too, can be extended through additional phenylene rings (Figure 1.8, right) and have its functionality altered by the addition of pendant groups.

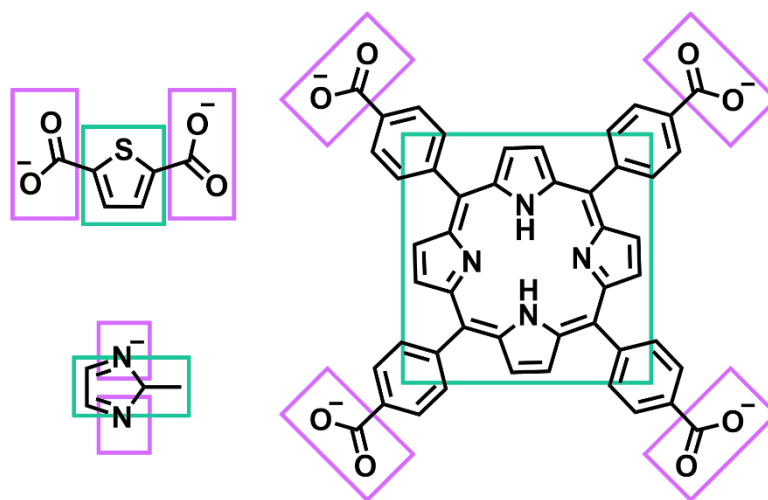


Figure 1.9 Three different organic linkers seen in MOFs with their sturdy cores (green) and attachment points (purple) highlighted.

The concept of using a rigid core with symmetric attachment points forms the basis of MOF design; there are many ligand families that can be developed from this approach. These include, but are not limited to, imidazoles³⁷ and porphyrins³⁸ (Figure 1.9). Some of these ligand families, such as imidazoles, cannot be lengthened, and other families may not have any substitution sites available for pendant groups, but MOFs containing these groups have still been utilized for many novel investigations. For example, ZIFs, which are formed from M^{2+} ($M = Zn$ is very common) and different imidazole linkers, have been found with a wide range of pore sizes, pore functionalities, and have even been featured in MOF glasses and amorphous MOFs.³⁹ Thus, although a linker system would ideally possess all of the properties described above, it is not always possible or necessary³⁸ for a linker to meet all of the ideal criteria. With a few exceptions,⁴⁰ as long as a molecule has a rigid core and a symmetric distribution of coordinating moieties, it is possible for it to be employed as a linker in a MOF.

1.2.3 The utility of reticular chemistry

Through the judicious choice of linkers and nodes, MOFs can be designed with intended properties in mind. This leads to the deliberate production of materials tailored to specific applications; this top-down design process is called “reticular chemistry”.⁴¹ The nature of MOF synthesis thus permits large changes to structures, as outlined above, but also changes at the sub-Ångstrom level.⁴² This provides tremendous range and precision in design.

This can be seen on a large scale in the use of specific linkers to mitigate the phenomenon of interpenetration in MOFs with large pores. Interpenetration refers to the behaviour where one crystal lattice will grow inside of another, effectively entangling the two structures. One recent approach to discouraging this behaviour is in the development of MOFs whose topology specifically prevents interpenetration.⁴³

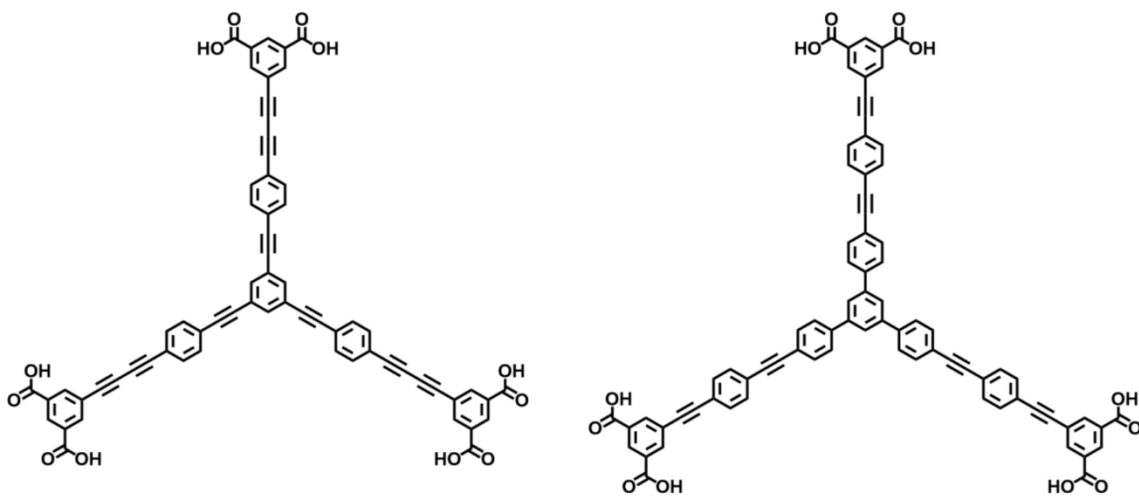


Figure 1.10 The linkers used in NU-109 (left) and NU-110 (right).

The *rht* topology is one such topology found in high surface area MOFs such as NU-109 and NU-110.¹⁹ This topology prevents interpenetration due to its geometry – a second

network is not able to weave itself into the first as they would bump into one another as opposed to nestling inside one another comfortably. The specific family of linkers used in the synthesis of these MOFs is what helps to provide this resistance to interpenetration, so new MOFs with the *rht* topology are developed by building new linkers with these structural features (Figure 1.10).

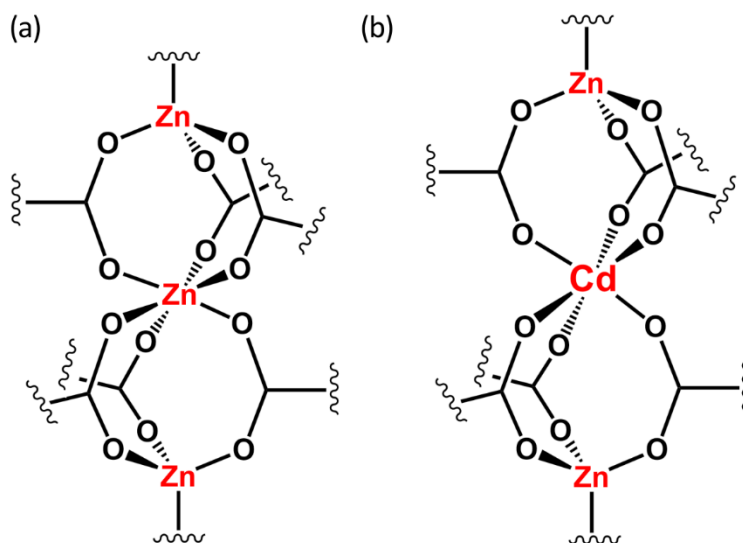


Figure 1.11 The eight-connected clusters found in the Zn_2M family of MOFs: (a) Zn_3 , (b) Zn_2Cd . Note how the increased atomic radius of Cd makes the Zn_2Cd cluster slightly longer.

At the other extreme is an example of sub-Ångstrom changes that can be seen in the Zn-based MOFs developed by previous students in the Katz group.⁴⁴ There are two MOFs in this family that share the same linkers, connectivity, etc., and differ only in the identity of the middle metal cation in their linear M_3 node (Figure 1.11). In the Zn_3 version of the MOF, the middle metal cation in the cluster is Zn(II) (Figure 1.11 (a)), and in the Zn_2Cd version, the middle metal cation is Cd(II) (Figure 1.11 (b)). The Zn_3 version of the MOF has small pore apertures that allow CO_2 to enter but not N_2 . Because Cd is larger than Zn, the Zn_2Cd version of the MOF has slightly larger pores, allowing N_2 and CO_2 to both enter

the MOF. The kinetic diameters of CO₂ and N₂ differ by only 0.34 Å⁴⁵ – that the change of a single atom in the MOF’s nodes can lead to the complete exclusion of N₂ speaks to the high level of atomic precision that MOFs such as these allow. This Zn₃ MOF is thus excellent for applications that involve gas separations, not storage, on a molecular scale (i.e., molecular sieving).⁴⁶

This tailorable and complex nature of MOFs allows for a broad range of applications, including molecular sieving,^{47,48} gas storage,^{49,50} removal of toxins from water systems,^{51,52} catalysis,^{53,54} medical imaging,^{55,56} and drug delivery.^{57,58} It is no wonder that this fascinating and diverse class of materials has prompted a great deal of research.

1.2.4 Defects

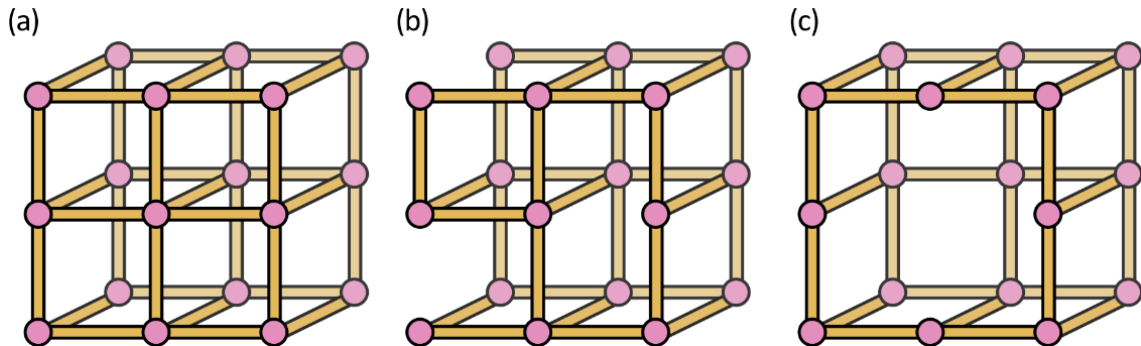


Figure 1.12 Crystal structures of examples of a MOF with various defects. (a) Pristine MOF, (b) MOF with missing linker defects, (c) MOF with a missing cluster defect, surrounded by missing linker defects.

In the enormous crystalline domain of the typical MOF, there are many opportunities for the periodic arrangement of atoms to be disrupted. Atoms/molecules/ions can be misplaced – a linker can end up sitting loose (i.e., uncoordinated) in a pore, for example – or they can be missing entirely. These locations where the “perfect” crystalline framework is disturbed

are called defects.⁵⁹ Either the organic linker or the inorganic node (or both) can be missing from the crystalline lattice, producing two different types of defects: missing linker defects, and missing cluster defects, respectively (Figure 1.12).

A missing linker defect occurs when a linker is not present to bridge the space between two nodes (Figure 1.12 (b)). The linkers that would normally coordinate to the node perform the act of charge balancing and/or satisfying the coordination chemistry of the metals in the node in doing so. Therefore, some other capping group or groups must take their place for the MOF to remain charge balanced or coordinatively saturated.⁶⁰ Thus, the coordination sites on the metal node will be occupied by ambient materials in the reaction mixture, such as water,⁶¹ modulators (further discussed in Section 1.3.1),⁶⁰ solvents,⁶² etc.⁶¹

Similarly, a missing cluster defect (Figure 1.12 (c)) occurs when the space that would normally be occupied by a node is unoccupied. While missing cluster defects can occur in the absence of missing linker defects, it is most often observed that missing cluster defects are a result of a critical concentration of missing linker defects.⁶³ That is, in most cases, all of the proximal sites around a missing cluster will have missing linker defects of their own.

The term ‘defect’ reflects the nature of these features, but not their desirability. Defects can afford many benefits to a MOF such as increased surface area,⁶⁴ enhanced catalytic activity,⁶⁵ and enhanced porosity.⁶⁴ Depending on the planned application for the MOF, chemists may attempt to synthesize MOFs that are defective in specific ways;⁵⁹ this deliberate manipulation of defects is called defect engineering.⁶⁶ Defects can be introduced through variations of reagent ratios, alterations to synthesis temperatures, synthesis in ionic

liquids, or the addition of reagents that will compete for coordination sites against the linker⁶⁷ (see the section on ‘modulators’ below).

There are near-infinite ways to arrange the atoms in a defective MOF given the scale of their domain, but there exists only one way to arrange the atoms in a pristine MOF. In this sense, defective MOFs are favoured entropically. Many MOF syntheses will produce defective MOFs by the sheer nature of the stochastic (i.e., random) process of crystallization in addition to the entropic favouring of their formation.

1.3 MOF Synthesis

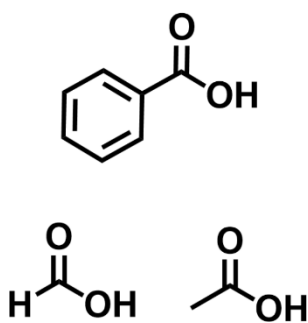
There are increasingly many possible routes to synthesize a MOF – among them are microwave-assisted synthesis,⁶⁸ electrochemical synthesis,⁶⁹ mechanochemical synthesis,⁷⁰ and sonochemical synthesis.⁷¹ Solvothermal synthesis, however, has remained the go-to synthetic approach for reasons such as its accessibility and ease of use, though there has been a shift away from solvothermal synthesis in recent years.⁷² In terms of equipment, all a chemist needs for solvothermal synthesis is a sealable container (jar, vial, or a Teflon-coated bomb digestion vessel) and an oven. In such syntheses, the reagents (i.e., a precursor for the metal node, the linker or linker precursor, the solvent, and potentially an acidic modulator) are added to the container, then the container is sealed and placed in the oven. After a length of time, typically 1-3 days, a MOF will have formed in the jar as either large crystals or a microcrystalline powder. After this, the MOF is “activated”,⁷³ which is a loose term for removing any pore-bound guests and ensuring that the structure doesn’t collapse prior to characterization or utilization. Activation is most

often done by first soaking the MOF in fresh solvent to remove any unwanted reagents – this is often the same solvent that the MOF was formed in – followed by exchanging the solvent for a more volatile one that will more readily leave the MOF pore. Then, the MOF is heated under vacuum. This is the typical approach, but there are other activation processes (e.g., drying with supercritical carbon dioxide).⁷⁴

It is worth stressing that it is most often the precursor for the metal node that is added to the reaction mixture and not the complete node itself. Indeed, just as MOFs assemble themselves from inorganic nodes and organic linkers, the inorganic nodes assemble themselves from metal precursors in the reaction mixture. The point in time at which these nodes assemble varies from MOF to MOF and is still highly contentious;⁷⁵ node assembly will be explored further in Chapter 2.

1.3.1 Modulators

Coordinating modulators



Non-coordinating modulators

HCl

HF

Figure 1.13 Common modulators used in MOF synthesis.

To better control MOF formation, a trend of employing compounds termed “modulators” in MOF synthetic procedures has emerged.⁷⁶ A modulator is typically an acidic solid or

liquid that is most often introduced into the reaction mixture at the same time as other reagents, and which influences the kinetics of MOF formation. Modulators with coordination groups imitating that of the organic linker (i.e., coordinating modulators) will compete with the linker for coordination sites on metal nodes. In some cases, the modulator will eventually dissociate, and a linker will take its place. In cases where the modulator remains bound in place of a linker as the MOF assembles around it, a defect is formed. The current understanding of MOF synthesis is that this competitive coordination slows down the rate of MOF formation,⁷⁷ which promotes a slower and more controlled crystallization process. Slower crystallization processes are associated with a lower number of defects and larger crystallite sizes.⁷⁸

Given that a coordinating modulator often needs to mimic the coordination chemistry of the linker, and many linkers are carboxylic acids, it is often the case that coordinating modulators are carboxylic acids as well. These acids must deprotonate in solution before they can coordinate to the node, and this deprotonation of the modulator will thus compete with deprotonation of the linker. As such, there is a “drop-off” point in the efficacy of modulators. Adding modulator past a certain point (either based on stoichiometry or concentration) will completely inhibit the self-assembly of the MOF.⁷⁹ Careful consideration of the quantity of modulator used is necessary, and finding this optimal quantity is often a trial-and-error process.⁷⁹⁻⁸¹

In addition to coordinating modulators, there exist non-coordinating modulators that influence MOF formation in other ways. For example, HCl is known to induce DMF hydrolysis, producing formic acid and dimethylamine in situ.^{82,83} The former can act as a

coordinating modulator and the latter can act as a base to any acid in solution (further discussed in Chapter 2). For MOFs with kinetically labile transition metal-based nodes, the presence of acid has been shown to increase crystal sizes by increasing the rate of node-linker substitution reactions, thereby slowing crystal growth. For kinetically inert transition metal-based nodes, this often ensures that node-linker substitution reactions are possible, thereby speeding up MOF formation and preventing the formation of ill-defined amorphous material. These are ultimately the same process but depend on the rates of node-linker substitution reactions.

The mechanism by which modulators affect the resulting MOF is not well-understood. There are significant differences in samples of the same MOF made with different modulators. For example, when UiO-66 is synthesized with HCl as a modulator, the resulting MOF forms quickly and with missing linker defects (ca. two missing linkers per formula unit).²⁶ Alternatively, when UiO-66 is synthesized with acetic acid as the modulator, then the MOF takes longer to form but contains few to no defects.⁸⁰

1.4 Characterization/Analysis of MOFs

As they are porous crystalline materials, the instrumental methods most associated with the characterization of MOFs are those that probe their surface area and crystallinity. Porosity is assessed by measuring how much gas is adsorbed onto a MOF (more accurately, the measurements determine how much gas is not adsorbed onto a MOF and the difference is assumed to be the quantity adsorbed on the MOF). Crystallinity is typically assessed using X-ray diffraction (powder or single crystal); powder X-ray diffraction (PXRD) is often

used for bulk purity characterization while single crystal X-ray diffraction is often used to obtain information regarding connectivity. There are many other characterization methods, such as atomic force microscopy and dynamic light scattering, but adsorption analysis and PXRD will be explored the most in this work.

1.4.1 Adsorption analysis and isotherms

The principal instrument for measuring the surface area of a material is a gas adsorption analyzer. Gas adsorption analyzers, such as the Micromeritics 3Flex and Micromeritics Tristar used in this research, work by dosing a porous material with a known quantity of a probe gas (such as N_2) at a fixed temperature (most often 77 K for N_2 gas). If the pressure of a known quantity of probe gas in a known volume is known (P_1V_1), and that gas is exposed to a new volume containing the porous material (P_2V_2), then we can determine the quantity of gas adsorbed by comparing these values (i.e., $P_1V_1 = P_2V_2 + \text{Quantity Adsorbed}$). The analytical measurements begin at a low pressure, and the pressure is increased after each measurement until the gas's saturation pressure is reached or the limit of the instrument is reached (ca. 1000 mmHg for the instrumentation used in this work). The resulting graph made by plotting the quantity adsorbed as a function of pressure (either absolute pressure, P ; or the ratio of the absolute pressure to the gas saturation pressure, P/P_0) is called an isotherm.

In this work, several isotherms will be compared and contrasted. Knowing this, it is beneficial to review the characteristic shapes of isotherms that appear in this work, as they will be used to differentiate materials in Chapter 3.

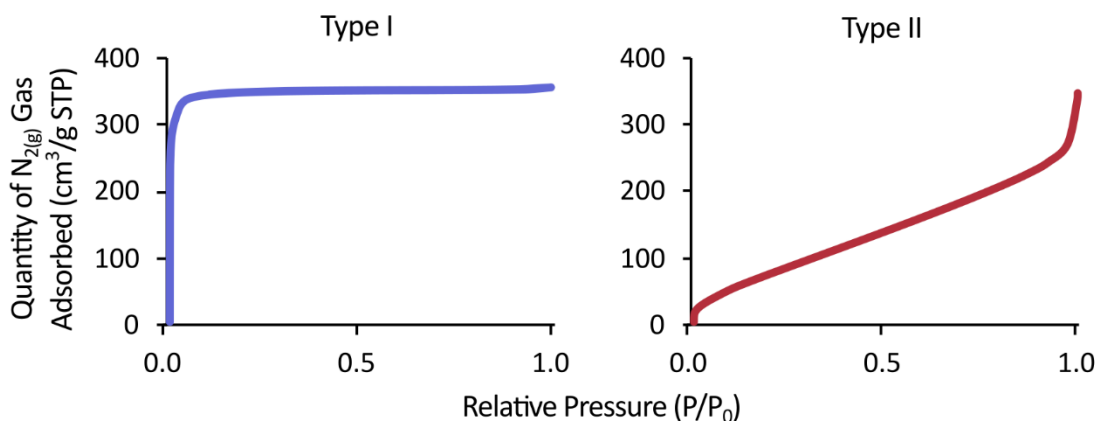


Figure 1.14 Examples of the two types of adsorption isotherms that appear in this work.

A Type I isotherm (Figure 1.14, left) is the quintessential isotherm, and is associated with porous materials that contain micropores (i.e., pores < 2 nm) and have low external surface areas. A Type I isotherm will be concave to the x axis at low pressures and then plateau after reaching a critical volume of adsorption. The point at which the plateau begins is associated with the material's adsorption sites becoming saturated, preventing any further gases from being taken up by the material.

At low pressures, a Type II isotherm (Figure 1.14, right) is concave to the x axis, much like a Type I isotherm, but then trends linearly upwards once it leaves the low-pressure region, after which it becomes convex to the x axis at high relative pressures. Type II isotherms are common in materials that contain macropores (i.e., pores > 50 nm) or that are altogether nonporous. In MOFs, a Type II isotherm (specifically its upward sloping region) is a common indicator that a sample has a high external surface area.

The low-pressure region, where the isotherm is concave to the x axis, is where the data used to calculate the porosity of the material can be found.

1.4.2 BET surface areas

Many theories to explain and model the process of adsorption have emerged (e.g., Langmuir, Freundlich, Toth),⁸⁴ but the most popular among them for MOF chemists is Brunauer-Emmett-Teller (BET) theory,^{85,86} which is used in the calculation of MOF surface areas.

$$\frac{P/P_0}{n(1 - P/P_0)} = \frac{C - 1}{n_m C} (P/P_0) + \frac{1}{n_m C} \quad (\text{Equation 1.1})$$

Equation 1.1 represents the BET equation in the linear form of $y = mx + b$, wherein $m = (C-1)/(n_m C)$, $x = P/P_0$, and $b = 1/(n_m C)$. In the equation, P is equilibrium pressure of the adsorbate, P_0 is the saturation pressure of the adsorbate, n is the quantity of gas adsorbed at P/P_0 , n_m is the monolayer capacity that relates to surface area for the adsorbed gas, and C is the BET constant. The monolayer capacity of the material (n_m) represents the volume of adsorbed gas necessary to cover the surface of the MOF in one layer of gas molecules. Knowing the volume of the probe gas as well as the cross-sectional area of the probe gas, the monolayer capacity will thus be used to calculate the surface area of the material. It is worth noting that the BET equation will not fit an entire isotherm because the BET equation has no limit as to how much gas can adsorb on a surface, but a MOF pore can be filled only until there is no room left to adsorb more gas. As such, it is important to ensure that the correct region of an isotherm is used in the BET calculations. To this end, the isotherm must be converted from the form in which it is collected (i.e., quantity adsorbed vs. pressure) to the linear form (Equation 1.1). From here, there should be a linear region observed in the low-pressure range of the isotherm. If a selection of points from the linear

region are correctly chosen, numerical values for the slope $\left(\frac{C-1}{n_m C}\right)$ and the intercept $\left(\frac{1}{n_m C}\right)$ can be extracted to solve for n_m and C . There are multiple criteria⁸⁷ that must be met for the BET analysis to be considered valid, however.

1. C must be positive. As C is related to the adsorption energy, C must be positive or else it would imply that gas molecules would prefer to remain in the gas phase than adsorb to the surface of the material, which, if true, would disallow the collection of the isotherm in the first place.
2. The region chosen for BET calculations must only include data points where $n(1-P/P_0)$ vs. P/P_0 is increasing. This plot of $n(1-P/P_0)$ vs. P/P_0 is another way of viewing the BET equation. In this frame of reference, the BET equation is increasing until n_m is reached, at which point the BET equation plateaus. Any collected datum that is not at a higher $n(1-P/P_0)$ than the previous datum indicates that the MOF is no longer filling in a fashion that is consistent with the BET equation, and thus these data cannot be used.
3. The pressure at which the monolayer quantity (n_m) is measured on the isotherm must occur in the linear region chosen for the fit. That is, if the data being fit are being used to determine the monolayer quantity, then the monolayer quantity should be part of the data being fit.
4. The relative pressure at which the monolayer quantity (n_m) is measured is equal to $\frac{1}{(\sqrt{C}+1)}$. If the calculated pressure is within ca. 10% of the measured pressure for n_m ,

then this point is satisfied. Given the approximate nature of this criterion, it is often the first to be neglected in a fit.

Since the monolayer capacity of the adsorbed gas, n_m , is a direct consequence of the surface area of the material, n_m can be used to solve for the total surface area (S_t) using Equation 1.2, where N is Avogadro's number, s is the cross-sectional area of the adsorbed gas molecule, and V is the molar volume of the adsorbed gas. The total surface area is then divided by the mass of the sample to give the specific surface area (SSA) in m^2/g .

$$S_t = \frac{n_m N s}{V} \quad (\text{Equation 1.2})$$

Realistically, the same MOF synthesis procedure can produce MOFs with a range of calculated surface areas that deviate from one another in either direction. This is what MOF chemists refer to as batch-to-batch variability, and it is typically accounted for when attempting replication of a MOF synthesis. To this end, for a MOF chemist synthesizing multiple samples of the same MOF, two surface areas within 10% of each other are considered to be equivalent.

There are many potential sources for this batch-to-batch variability, including the age of the reagents used (e.g., ZrCl_4 readily hydrolyzes into zirconyl chloride (i.e., ZrOCl_2 , which is more accurately described as $[\text{Zr}_4(\text{OH})_8(\text{H}_2\text{O})_{16}]\text{Cl}_8(\text{H}_2\text{O})_{12}$)), so purity of ZrCl_4 is compromised over time), the amount of water in the solvent (DMF is hygroscopic and will absorb atmospheric water), the region of the data chosen for BET surface area analysis (MOF chemists often report their regions to help with reproducibility), the number of

points on the isotherm used to calculate the surface area, or even just the fundamentally stochastic nature of MOF crystallization.

1.4.3 Pore size distributions

Much like how BET theory can be used to extract the surface area of a sample from its isotherm, density functional theory (DFT) can be used to extract the pore sizes of a sample from its isotherm.⁸⁸ It is important to note that DFT in this case refers to the density of the adsorbent and not the electronic configuration DFT that chemists often refer to; DFT for pore size evaluation constructs the theoretical adsorption isotherms belonging to ideal pore geometries using classical fluid density functional theory. Employing DFT on an isotherm produces a pore size distribution (PSD), which communicates the various sizes of the pores in the sample and the relative amounts of the overall volume that they constitute. It is easier to understand how PSDs are calculated if one understands why isotherms appear the way that they do.

An isotherm depicts the quantity of gas adsorbed over a pressure range, and the pressure at which an isotherm trends upwards is related to the point at which pores of a specific size are filled. Thus, the shape of an isotherm is a consequence of the pore sizes within the material. For example, imagine some generic porous material with only one single pore size of 2 Å. This material would produce an isotherm that looks like the pink line in Figure 1.15 (a). If that pore was 8 Å instead of 2 Å, then it would begin to adsorb at higher pressure and it would appear as the blue line in Figure 1.15 (a). If one had a material that had pore sizes of both 2 and 8 Å, then their isotherm would appear as though it were a combination

of the isotherms of those two pore sizes (Figure 1.15 (b)), and the nature of that combination would reflect how much of each pore was present (Figure 1.15 (c)).

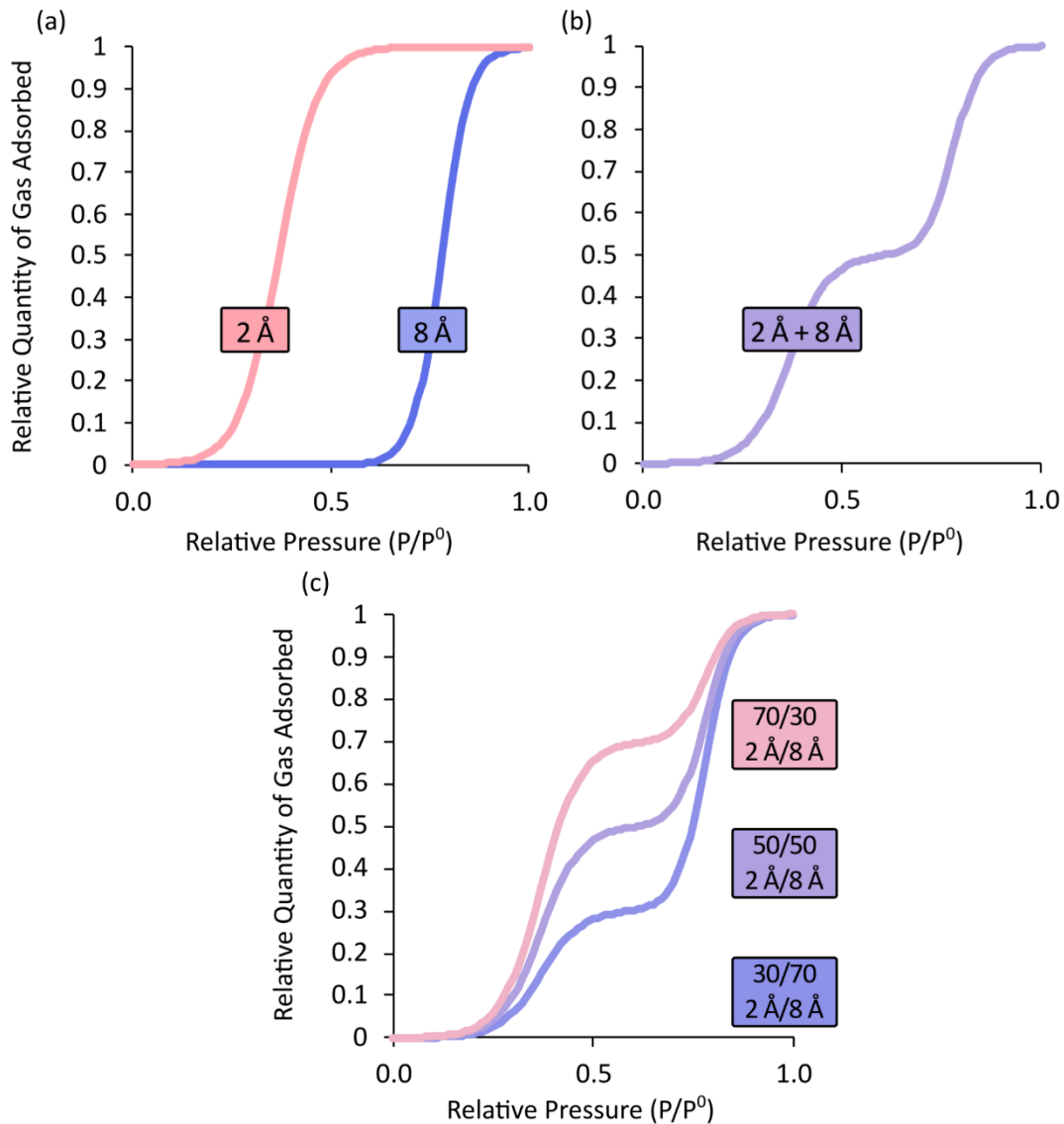


Figure 1.15 (a) Two simulated isotherms for a porous material. The pink line represents a material with pores of size 2 Å, and the blue line represents a material with pores of size 8 Å. (b) Simulated isotherm for material with a 50/50 mixture of 2 Å and 8 Å pores. (c) Simulated isotherms for material with varying ratios of 2 Å and 8 Å pores.

In this regard, an experimental isotherm can be seen as a convolution of several theoretical isotherms. That is, a real isotherm collected from an experiment can be modelled as though

multiple theoretical isotherms were combined to form it. If each of the theoretical isotherms that make it up is associated with a specific pore size, then one can tell what size of pores a MOF contains by which theoretical isotherms would have to be combined in order to reproduce its experimental isotherm.

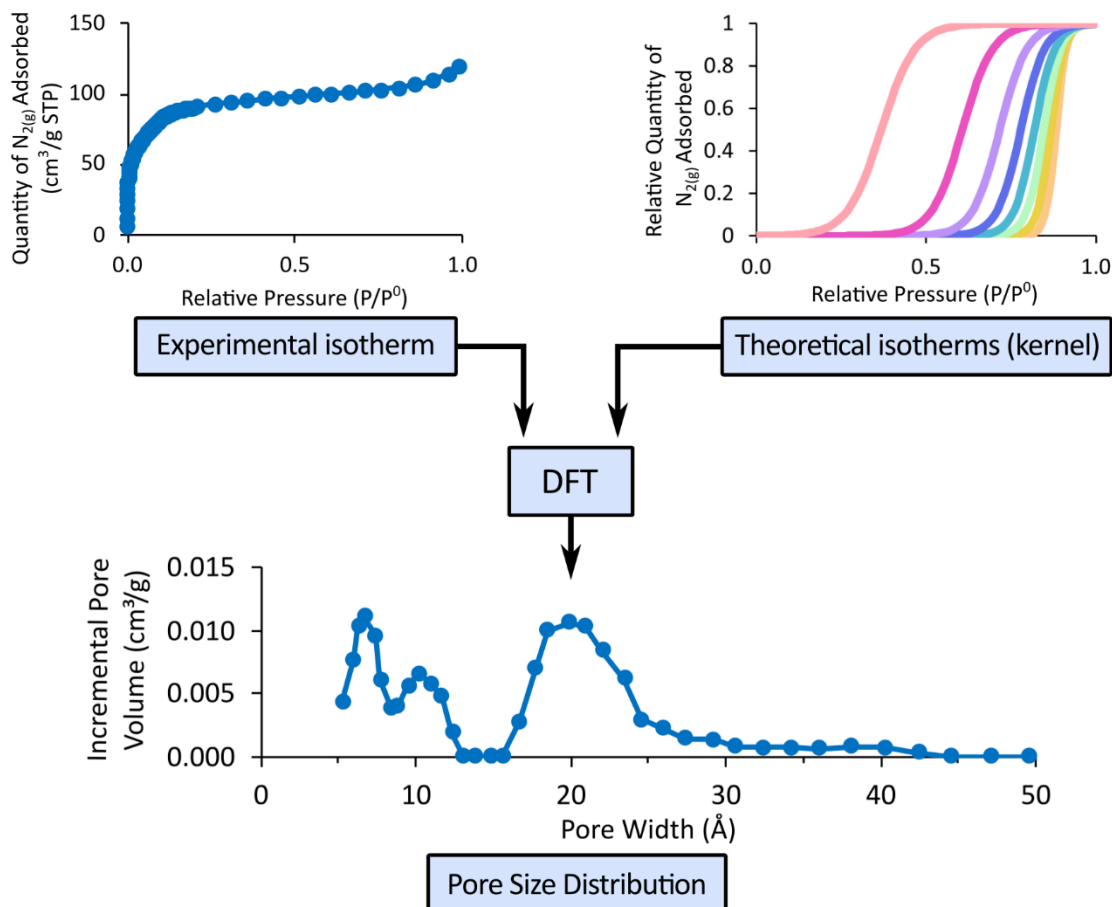


Figure 1.16 A representation of how the experimental isotherm and theoretical isotherms are both used to calculate the PSD of the material.

Of course, to break apart an experimental isotherm into multiple theoretical ones, the theoretical isotherms must exist. These sets of theoretical isotherms are called kernels, and they are unique to various materials, such as pillared clay or oxide surfaces. There are no kernels designed specifically for MOFs due to the sheer variety of linkers, nodes, and MOF

topologies. It is a tremendous task to attempt to account for all of the various linkers, topologies, nodes, etc. that are seen in MOFs; MOF kernels may have to be specific to each unique MOF family in order to be useful. As such, choosing a kernel for a MOF PSD is typically a matter of identifying the kernel that produces the lowest error.

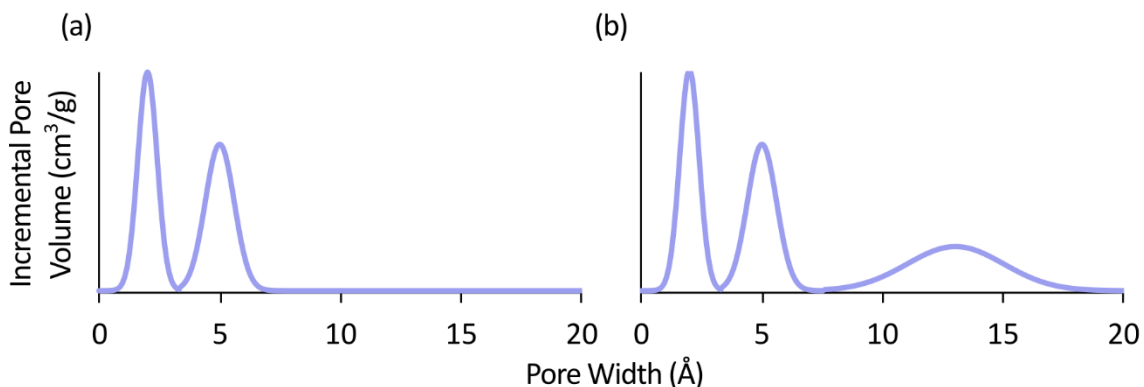


Figure 1.17 Simulated pore size distributions of a porous material. (a) A pristine material with pores of size 2 and 5 Å. (b) The same material with defects present.

It is important to note that the presence of defects in a MOF will alter the resulting PSD. As mentioned earlier, the absence of a linker between two pores causes the two pores to behave as though they are one singular larger pore. Depending on where these defects are placed and the topology of the MOF, this may cause additional “pores” to appear on the PSD at a larger size than the original pores that constitute the defect pore (Figure 1.17).

1.4.4 Powder X-ray Diffraction

Like other crystalline materials, MOFs are regular arrangements of atoms, which make them excellent candidates for analytical models relying on diffraction, such as PXRD. MOFs, with their variety of topologies and pore sizes, will produce diffractograms that are characteristic of their structure. A powder X-ray diffractogram can be used as a fingerprint

for a MOF – if an experimental sample produces the same diffractogram pattern as a known MOF, the sample must be that MOF or at least closely related to it. The intensities of the peaks on the diffractogram may be different from other samples as they are often affected by the presence of guest molecules (e.g., solvents) in the pores, but the peak positions will match if the materials are the same.

This ability to cross-check a MOF against a known diffractogram is often exploited by rendering simulated diffractograms from crystal structures and comparing experimental samples to these. Such simulated diffractograms are “idealized” fingerprints of the MOF, as they are not influenced by guest molecules.

1.5 Motivation of this Thesis

This thesis contains the research on two different, but related, MOF research projects. The initial research project I took on during my Master’s concerned the synthesis of a MOF with a novel tetratopic phthalocyanine-based linker that was previously discovered by a student in the Katz group (this work is found in Chapter 3). There are very few phthalocyanine-containing MOFs due to the challenges associated with installing attachment points on them, which is a shame as phthalocyanines are a fascinating group of macrocycles that offer a great deal of utility when installed in a MOF. The intent of this first project was to explore and refine the synthesis of this novel phthalocyanine MOF and obtain its crystal structure. Optimization of a MOF synthesis with a novel linker is especially difficult when most facets of the reaction are not thoroughly understood. For example, as mentioned earlier, the differences between how different modulators

contribute to MOF formation is poorly understood, so attempting to identify the ideal modulator for a MOF synthesis is more of a trial and error undertaking, rather than a rational or systematic approach. The amount of trial and error necessary to experiment with a reaction that was not well-understood led us to wonder if there was a better way to approach such syntheses in the future – was there a way we could learn more about what makes MOF syntheses tick and ameliorate some of the difficulties associated with refining a MOF synthesis?

This led to the development of the second MOF research project, which sought to use solution ^2H -NMR, heretofore unused in the field of monitoring MOF synthesis, to follow the self-assembly of UiO-66, one of the most popular MOFs (this work is found in Chapter 2). Despite the ubiquity of UiO-66, it suffers from many of the same gaps in insight that plague novel MOFs, such as the specific influence of each modulator, the extent of solvent participation, and the rate at which linker is incorporated into the MOF. ^1H -NMR would provide insight into the concentration of reagents in solution, the relative activity of water molecules, and changes to pH over the course of the reaction, but unfortunately, it has proven difficult to investigate MOF syntheses via ^1H -NMR due to the cost of necessary reagents (e.g., the exorbitant cost of $\text{DMF-}d_7$). We thus proposed and explored the idea of using ^2H -NMR to follow the formation of UiO-66, allowing us to gain much more robust insight into how the MOF synthesis changes under the influence of different coordinating and non-coordinating modulators.

Statement of Co-Authorship

Content from the following chapter appears in:

A.P. Parsons; C.M. Schneider; M.J. Katz. ^2H NMR as a Practical Tool for Following MOF Formation: A Case Study of UiO-66. *Angewandte Chemie (International ed. in English)*, 2025, 64(8), e202420157. © Copyright 2025 Wiley-VCH GmbH or related companies. All rights reserved, including rights for text and data mining and training of artificial intelligence technologies or similar technologies.

Author contributions: Amanda P. Parsons contributed to the majority of the manuscript by conducting the experimental work, processing and analysing the data, and preparing and editing the manuscript. Céline M. Schneider was responsible for oversight of the NMR spectrometer and the selection of parameters for the ^2H -NMR experiments. Michael J. Katz was the principal investigator for this project.

The manuscript has been reproduced in this chapter with modifications to provide an extended discussion of the obtained results.

Chapter 2

Exploring Modulated Mechanism of Formation of UiO-66 via $^2\text{H-NMR}$

2.1 Introduction

Despite the growing popularity of MOFs, very little is understood about the mechanism of self-assembly by which these crystalline sponges form. As new linkers and nodes are being explored for incorporation into MOFs, it often takes a great deal of trial and error to determine the optimal reaction conditions that allow for reproducible crystallinity and surface area. This brute-force trial-and-error method is time-consuming, requires a great deal of labour, and produces a large amount of chemical waste; such is one's lot without the ability to precisely identify how temperature, reactants, modulators, solvents, etc. relate to MOF formation. It would avail the scientific community greatly if the mechanism of formation of MOFs was better understood; knowing how each components of the reaction mixture affects the nucleation and growth process of a MOF and the associated crystallinity and surface area would allow for the synthesis of more finely-tuned materials, and would allow for a more precise determination of the cause of certain traits in MOFs (defectivity, crystallite size, etc.). As an example, one may find that their desired use case for a MOF requires a smaller particle size (e.g., for use in films, for drug delivery, etc.). If one knew which features of the reaction mixture produced smaller particles, and ideally why, then

they could tailor their synthesis accordingly and produce their desired MOF straight away, rather than having to attempt to adjust the particle size after the synthesis is complete. Essentially, if there was a full picture of the mechanism of MOF formation, including an understanding of the roles of reagents, then the synthesis of desired materials could be obtained much more logically, and there would be less reliance on brute-force trial-and-error methodology.

Ex-situ analytical methods such as X-ray diffraction (XRD),⁸⁹ scanning electron microscopy (SEM),⁹⁰ and atomic force microscopy⁹¹ have been utilized to probe the mechanism of MOF formation at various intervals. While this is informative, there are several limitations to this work. Depending on the method of retrieval, ex-situ work requires that the reaction is interrupted for sampling, which can change both the sample and the reaction mixture it was drawn from. For example, opening the reaction vessel for sample retrieval will flush the headspace, incite further evaporation of the reaction mixture, and allow heat to be lost to the room-temperature air that floods in. If volatile products are being produced as a product of DMF decomposition, these products being flushed from the headspace may alter the equilibrium of the reaction mixture, potentially urging further DMF decomposition and thereby altering the kinetics/thermodynamics. Alternatively, if one lets the reaction cool before retrieving the sample, the kinetics of the reaction are slowed, thus introducing a new variable that becomes increasingly hard to control for as more samples are taken. For sample retrieval methods that do not involve opening the reaction vessel (i.e., retrieval by canula or syringe), there is still the issue that many analytical instruments cannot immediately meet and maintain the conditions of the original

reaction mixture that the sample was drawn from. Changes in the amount of headspace in the vessel, the uniformity of heating, the chosen reaction temperature, and the material used as a vessel can lead to additional variables that could alter the data between sampling and analysis. If the sample in the instrument cannot be held at the same uniform temperature as the original mixture, then the kinetics of the reaction will be affected, and if it does not have the same amount of headspace as the original mixture, gaseous by-products will be present in different partial pressures. As an additional example, if mass spectrometry of the sample is desired,⁸² then dilution (often not in the synthesis solvent) of the original solution mixture is necessary for data collection. This all inherently changes the concentration and the chemistry of the reaction and thus introduces doubt into the validity of the results. Hence, one will find themselves with a sample that may no longer be representative of the original reaction mixture it was drawn from. In some cases, this difference between the sample and the original mixture may be small enough that the collected data are still of interest, but this is something that must be accounted for on a case-by-case basis, leading to the need for many control experiments to ensure data validity; these experiments may not be universally true for all MOF syntheses and thus every research group may have to repeat these (or related) experiments in order to use ex-situ techniques.

To obtain data that are truly representative of the reaction mixture at a point in time, in situ analytical methods are a much better option. In situ analysis allows one to obtain data from a sample that directly represents the reaction mixture it is from by performing real-time analysis on the original reaction mixture as the reaction takes place. The crystallinity and

surface area of the reaction mixture can be validated, thus providing a much clearer lens into the reaction proper.

In the literature, various in situ methods have been used to investigate MOF formation. Xu et al. used in situ pair distribution function analysis to probe the solvothermal synthesis of UiO-66.⁹² They saw the presence of the $[\text{Zr}_6\text{O}_4(\text{OH})_4]^{12+}$ cluster in the metal salt precursor solution at room temperature, before the ligand was ever added. Conversely, Semivrazhskaya et al. used in situ mass spectrometry and X-ray adsorption spectroscopy to come to the opposite conclusion: Their results suggested that, in the synthesis of UiO-66, the $[\text{Zr}_6\text{O}_4(\text{OH})_4]^{12+}$ cluster never fully forms alone in solution and is instead only formed when zirconium chloroterephthalates undergo solution-mediated hydrolysis and assemble into nodes.⁸²

The formation of the same $[\text{Zr}_6\text{O}_4(\text{OH})_4]^{12+}$ cluster was followed by Zavorotynska et al. using in situ X-ray adsorption spectroscopy.⁹³ They assessed the influence of water and coordinating modulators on the formation of the cluster, before and after the addition of a fumarate ligand. They saw that water was essential for the formation of the $[\text{Zr}_6\text{O}_4(\text{OH})_4]^{12+}$ cluster, and the formation of the MOF. That is, in the absence of water, cluster formation and MOF formation were not observed.

In situ Fourier transform infrared spectroscopy (FTIR) as well as in situ Raman spectroscopy were used by Embrechts et al. to follow the formation of MIL-53(Al).⁹⁴ They saw the formation of a prenucleation building unit which consisted of one linker molecule and one aluminum atom, and the subsequent assembly of these building units in solution

to produce MIL-53; the rate-limiting step was determined to be this arrangement of prenucleation building units.

What is particularly notable in the literature regarding in situ analysis of MOF formation is the underrepresentation of NMR spectroscopy as a method. There does exist in situ NMR spectroscopy work in the literature, but very little of it is ^1H -NMR spectroscopy. The reasons for this underrepresentation will be expanded below.

2.1.1 Time-resolved ^1H -NMR

Nuclear magnetic resonance (NMR) spectroscopy is popular for in situ analyses involving materials that contain NMR-active nuclei. The most common NMR active nucleus is the hydrogen atom/isotope, which has a high sensitivity to electromagnetic influence, a spin of $\frac{1}{2}$, and nearly 100% relative abundance. Other NMR active nuclei such as ^{31}P , ^{19}F , and ^{15}N have also been explored for similar reasons. All modern-day NMR spectrometers offer users the ability to queue multiple intermittent experiments over a prolonged period, so time-resolved analyses on reaction mixtures can be easily conducted. This has allowed chemists to successfully examine the in situ synthesis of compounds over time. If a spectrometer is equipped with variable temperature capabilities, then reaction kinetics and thermodynamics can be readily determined.⁹⁵ Combined, these features allow a chemist the ability to conduct time-resolved analysis on a chemical reaction that takes place above room temperature, making NMR an excellent tool for in situ analyses.

Despite its utility, NMR spectroscopy has been underutilized in the field of MOF chemistry since the complexity of the reaction mixture necessitates the use of many deuterated

materials, some expensive or difficult to acquire. The compound to be observed must be in its ^1H form, but every other component of the reaction mixture would have to be in its ^2H form or not contain any protons. This would include any modulators (which are present in great stoichiometric excess, obfuscating peaks of interest); linker; water; and, especially, solvent that needs to be “hidden” in order to monitor the reagent of choice. While this can be accessible with certain solvents, as in the case of synthesis in D_2O ,⁸⁹ the logistical and financial barriers associated with the more common solvents prevent this method from seeing wider use.

For solvothermal MOF syntheses ranging from 80 °C to 160 °C, the most commonly used solvent is *N,N*-dimethylformamide (DMF), often alongside water. To follow any of these syntheses that are formed in DMF via ^1H -NMR, one would need to purchase and employ deuterated DMF (DMF- d_7), which is far more expensive than regular, protonated DMF (\$70.66/mL for DMF- d_7 vs. \$0.22/mL for protonated DMF at the time of writing). One could attempt to measure the cost of one ^1H -NMR experiment in DMF- d_7 as the price of 700 μL of DMF- d_7 (i.e., a typical volume for NMR analysis), but this is disingenuous. Preparing such a small sample would necessitate the addition of miniscule amounts of reagents (e.g., < 3 mg of linker (H_2BDC) for UiO-66-HCl), which would negatively impact the consistency and reproducibility of the experiment given that such small quantities are challenging to accurately weigh out. Typically, larger samples are prepared and then a 700 μL aliquot is dispensed into the NMR tube. Thus, in order to prepare samples with reasonable analytical precision, one could expect to use 10 mL of DMF- d_7 for each sample. This cost rapidly adds up – to prepare and perform 21 experiments (i.e., this work), at

\$70.66/mL for DMF-*d*₇, one could expect to pay \$8340 for DMF-*d*₇ alone. Even for research groups with ample funding, this is a significant price tag if one is not sure whether they are even going to learn anything. This is to say nothing of any failed experiments or experiments that must be re-run. The true cost of performing 21 experiments may far outstrip the \$8340 estimate, severely limiting the potential scope of the work; many points of interest may end up being waylaid in the interest of limiting the cost.

In an ideal world, a researcher would never have to choose between science and their budget. Ideally, one would decide which experiments to perform based on the amount of information they feel they could acquire – not based on whether or not they can afford the reagents. This is sadly not the case in reality. There are many small labs that do not have the luxury of accessing expensive deuterated solvents, and in situ NMR work would be effectively off-limits to them until they could foot the bill.

To date, few in situ analyses of MOF formation via ¹H-NMR have been explored due to these restraints. In the analysis of syntheses performed in DMF, the groups employed DMF-*d*₇,^{96,97} suggesting that their funding could support such ventures, and they employed the use of solid-state NMR probes, which require different expertise that is not so easily found at all research institutes. Not all groups are so fortunate as to have such funding and expertise available, and more NMR analyses would likely be seen in the literature if these types of experiments were more accessible.

Protonated DMF (i.e., “regular” DMF), as mentioned above, is significantly cheaper than DMF-*d*₇, and if protonated DMF could be used for ¹H-NMR, then the 21 experiments above

would cost an order of magnitude less. Unfortunately, the solvent signal from using protonated DMF would massively eclipse any relevant peaks in any ^1H -NMR spectrum.

2.1.2 ^2H -NMR

In the typical chemical shifts of ^1H -NMR spectra, ^2H signals are not visible – it is this phenomenon that allows deuterated solvents to be used for ^1H -NMR analyses of protonated analytes. The reverse is also true: In the typical chemical shifts of ^2H signals, ^1H signals are not visible. This feature allows the ability to perform ^2H -NMR on a deuterated analyte in a protonated solvent. Incidentally, a spectrometer's lock channel, whose function is to monitor and correct for any drift of the spectrometer's magnetic field, functions by monitoring ^2H signals of deuterated solvents. The instrument's lock coil is tuned to ^2H by necessity, allowing one to alter its experimental purpose and use it to follow ^2H . This is the principal hook of ^2H -NMR for reaction monitoring; one will employ a deuterated analyte and follow it over the course of the analysis, and all other materials in the reaction mixture will be in their protonated forms, allowing their signals to be disregarded.

Many of the challenges seen with the use of ^1H -NMR for monitoring MOF formation can be mitigated through the application of ^2H -NMR instead. Large volumes of expensive deuterated solvents, deuterated water, and deuterated modulators are done away with entirely with ^2H -NMR – their protonated equivalents, which are likely already present in a MOF chemist's lab, can be used freely.

In order to follow the concentration of linker in the reaction mixture in such a ^2H -NMR experiment, one would need to employ a deuterated version of their linker. For structurally

simple linkers like benzenedicarboxylate (BDC^{2-}), deuterated versions of their acidic forms ($\text{H}_2\text{BDC-}d_4$) can be purchased from chemical retailers. While it is indeed the case that deuterated benzenedicarboxylic acid is more expensive than its regular, protonated counterpart (\$0.11/g for H_2BDC vs \$171/g for $\text{H}_2\text{BDC-}d_4$), this cost still pales in comparison to the cost of $\text{DMF-}d_7$. That is, it is significantly cheaper to perform $^2\text{H-NMR}$ with $\text{H}_2\text{BDC-}d_4$ than it is to perform $^1\text{H-NMR}$ with $\text{DMF-}d_7$. Approximately 800 MOFs use BDC^{2-} as their linker according to the CCDC,⁹⁸ which opens the door to many avenues of experimentation on how BDC-containing MOFs form with different cations, clusters, kinetically labile nodes, and kinetically inert nodes.

2.1.3 UiO-66

UiO-66 is a BDC-containing MOF, which makes it a great candidate for analysis via $^2\text{H-NMR}$. UiO-66 was discovered in 2008 by Cavka et al. at the University of Oslo (hence the name) and, in the time since, has become the subject of a great deal of research.³² UiO-66 consists of zirconium-containing nodes ($[\text{Zr}_6\text{O}_4(\text{OH})_4]^{12+}$) that are connected to 12 adjacent nodes via BDC^{2-} linkers.²⁸ This connectivity produces a topology with two types of pores (Figure 2.1). The larger of the two is the octahedral pore (11 Å, Figure 2.1 pink octahedron) and the smaller is the tetrahedral pore (8 Å, Figure 2.1 blue tetrahedron). The octahedral pore edges share with other octahedral pores, and the tetrahedral pores are face-sharing with the octahedral pores.

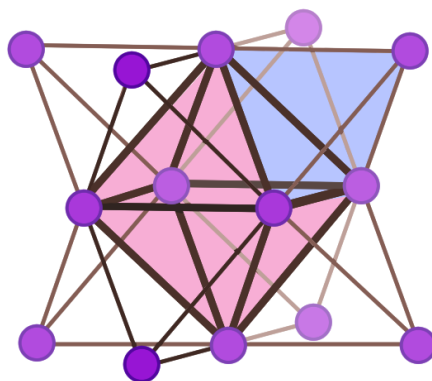


Figure 2.1 Crystal structure of UiO-66 presented to highlight the octahedral pore (red) and tetrahedral pore (blue). Purple circles represent the $[\text{Zr}_6\text{O}_4(\text{OH})_4]^{12+}$ nodes, and grey/black lines represent the BDC^{2-} linkers.

UiO-66's popularity as a subject of research can likely be attributed in part to the relative ease of its synthesis.^{32,99,100} The reagents required can be used as purchased, and the MOF itself forms quickly enough that overnight synthesis is standard. Despite how straightforward it is to produce a sample of UiO-66, precious little is understood about how UiO-66 forms.

At the time of its discovery, UiO-66 was synthesized without the use of any modulators (Section 1.3.1), but in the years since, a variety of acids have been used to influence the self-assembly of UiO-66; some common modulators include acetic acid,¹⁰¹ hydrochloric acid,⁹⁹ benzoic acid,⁷⁹ formic acid,¹⁰² and hydrofluoric acid.¹⁰³ These modulators are known to affect the resulting MOF in different ways. For example, acetic acid is known to produce samples of UiO-66 that are pristine (i.e., contain few to no defects) and which have an octahedral crystal morphology. Hydrochloric acid, by comparison, is known to produce samples of UiO-66 that contain many defects and have a spherical/clumpy visual morphology.

That the nature of the MOF is susceptible to such pronounced change under the influence of different modulators suggests that complex processes are taking place in the reaction mixture; this makes UiO-66 an ideal candidate for analysis via in situ ^2H -NMR.

2.1.4 Pre-conditioning reagents

Within the reaction space of UiO-66, there are alterations to the synthesis that can be made to elucidate further information. Typically, all of the reagents for the synthesis are present in the vial at the time the reaction mixture is placed in the oven, but this is not a strict rule. By pre-conditioning certain reagents (i.e., heating them for a specified period of time) in the oven together ahead of the synthesis proper, a greater understanding of the individual role of each reagent can be achieved. For example, pre-conditioning DMF with a modulator may allow the role of the solvent in the reaction to be further scrutinized. When in the presence of water and a strong acid, DMF is known to undergo hydrolysis to produce formic acid and dimethylamine (Figure 2.2). When a MOF is being synthesized, given the hygroscopic nature of DMF and the use of aqueous reagents (eg., $\text{HCl}_{(\text{aq})}$), water is usually present in the reaction mixture, and the modulators used in the synthesis are acidic. Thus, the necessary conditions are met for DMF hydrolysis to occur in situ during MOF formation. That the conditions are met does not guarantee that the process occurs in the time frame of the MOF synthesis, however. These hydrolysis products, if present, likely contribute to MOF formation.

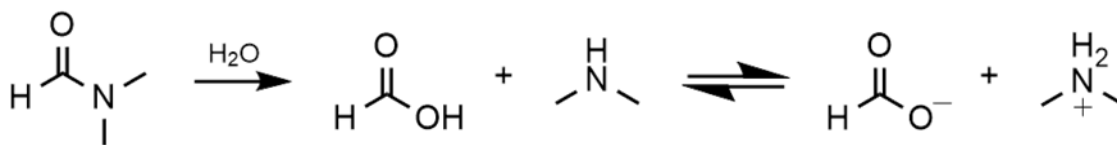


Figure 2.2 Hydrolysis of DMF into formic acid and dimethyl amine, which are in equilibrium with formate and dimethylammonium.

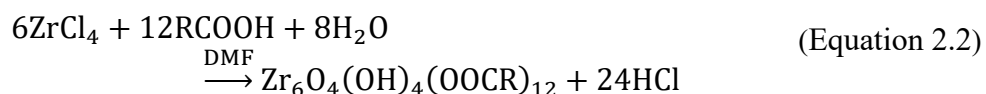
Formic acid, as previously mentioned, is a common modulator in MOF synthesis, so it is suspected that formate produced via hydrolysis fulfills the role of a modulator and competitively binds to the metal node.¹⁰⁴ Dimethylamine, being a relatively strong base (Table 2.1), is suspected to remove protons from solution during the reaction and shift the equilibrium to MOF formation (Equation 2.1). Given that the linker and modulators must be deprotonated before they can attach to the node, the presence of a base in the reaction mixture can prompt further deprotonation of carboxylic acids by removing protons from solution. Equation 2.1 shows an abridged version of the synthesis of the MOF from a metal chloride and a protonated linker, which leads to the production of HCl as a side product. As protons are removed from solution, the equilibrium can be shifted to the right in favour of further MOF production. Similarly, as discussed in Section 1.3.1, acid modulators could act to slow down the rate of MOF formation by shifting the equilibrium to the starting material.



To better understand this process in UiO-66, and, by extension (potentially), other MOFs, some of the following in situ ²H-NMR experiments will be performed using pre-conditioned DMF and modulator. That is, the DMF and chosen modulator will be placed in the oven at the reaction temperature and allowed to react for a length of time unique to

each modulator. Once the time has elapsed, the sample is removed from the oven and allowed to cool before the remaining reagents are added and the reaction mixture is returned to the oven for MOF formation. If the solvent is contributing to the MOF synthesis in any way, then the pre-conditioned sample should demonstrate different qualities than the standard synthesis sample. Samples made through this method will be referred to as “made with pre-conditioned DMF and [modulator]”.

In the literature, other groups have noted that pre-conditioning the solvent and modulator in the presence of the metal node precursor, (ZrCl₄ in this work) leads to differences in the synthesized samples of MOF. Taddei et al. saw that crystallite size for UiO-66 could be decreased by performing this pre-conditioning step.¹⁰⁵



Pre-conditioning the DMF and modulator in the presence of ZrCl₄ can pre-form the [Zr₆O₄(OH)₄]¹²⁺ cluster^{106,107} (Equation 2.2; R = H, Me, Ph) or potentially form a precursor to the node. To this end, pre-conditioning the solvent and modulator in the presence of ZrCl₄ will also be explored. Samples made through this method will be referred to as “made with pre-conditioned ZrCl₄ in DMF and [modulator]”.

2.1.5 Motivation of this research

To extract even one iota of insight into the reaction mixture of UiO-66 during MOF formation will contribute, proportionally, a significant amount of knowledge to the field of MOF synthesis. To conduct a battery of experiments under a series of different conditions

will produce a denser, more nuanced insight that allows for comparison between different reagents and techniques. This work seeks to learn more about the mechanistic differences between how different modulators behave in the reaction mixture, and how they contribute to self-assembly. This will be done by way of following the formation of UiO-66 under the influence of a selection of different modulators. Truly, anything learned through this method will provide valuable insight and generate an array of deeper questions regarding the nature of MOF formation.

2.2 Results and Discussion

2.2.1 UiO-66 characterization

In this work, UiO-66 was synthesized using three different, common modulators – namely, acetic acid (AA),¹⁰¹ benzoic acid (BA),⁷⁹ and hydrochloric acid (HCl).⁹⁹ While many other modulators have been successfully used,¹⁰⁸ they are less ubiquitous than the three chosen for study. As mentioned previously, AA is known to produce defect-free samples of UiO-66, and HCl produces samples with many defects. By employing and comparing the effects of modulators known to induce differences in the MOF, the nuances specific to these syntheses can be further identified. BA was chosen in addition to AA and HCl due to its ubiquity as a modulator in MOF synthesis, its existence as a solid (in opposition to AA and HCl being solution-phase), and its advantage of being an “innocent” modulator compared to AA (which is hygroscopic) and HCl (which is aqueous). Moreover, BA and AA have pKa values that straddle the pKa of HBDC⁻ (Table 2.1), permitting the further investigation of the competitive nature of the acid/base chemistry.

Table 2.1 pKas of the modulators explored in this work, alongside those of the protonated BDC linker and dimethylammonium.

	H ₂ BDC	Formic acid	Benzoic acid	HBDC ⁻	Acetic acid	(CH ₃) ₂ NH ₂ ⁺
pKa ^[a]	3.54	3.75	4.20	4.34	4.76	10.73

^[a] The values presented are aqueous values; these values are different in DMF.¹⁰⁹

The synthetic conditions for the synthesis under the influence of these chosen modulators are shown in Table 2.2.

Table 2.2 Amounts and concentrations of reagents used in the synthesis of UiO-66-AA, UiO-66-HCl, and UiO-66-BA.

	UiO-66-AA ^[a]		UiO-66-HCl ^[b]		UiO-66-BA ^[a]	
	mmol	M	mmol	M	mmol	M
H ₂ BDC	0.626	0.0125	0.752	0.0501	0.34	0.017
ZrCl ₄	0.635	0.0127	0.536	0.0357	0.34	0.017
AA	175	3.50 ^[c]	-	-	-	-
12 M HCl	-	-	12	0.75	-	-
BA	-	-	-	-	2.74	0.137

^[a] Synthesized in DMF. ^[b] Synthesized in water and DMF (0.25 mL of 12 M HCl in 3.75 mL of DMF; 0.75 M HCl and ca. 2.6 M water). ^[c] An estimated 0.03 M water is present from the acetic acid.

The UiO-66-AA and UiO-66-BA syntheses have similar concentrations of H₂BDC and ZrCl₄, but the UiO-66-HCl synthesis has a more concentrated (ca. 3.5x) reaction mixture than either of them. Due to the nature of aqueous HCl, the UiO-66-HCl synthesis also has the largest quantity of water present.

The HCl-modulated synthesis takes place at 80 °C, but the AA and BA syntheses typically take place at 120 °C. In the interest of ensuring the safety of the NMR spectrometer from any pressure buildup in the NMR tubes that were used, the AA and BA syntheses were performed at 100 °C instead of their conventional 120 °C. With that in mind, there is basis to suspect that a different material/crystallinity/surface area could form if two identical reaction mixtures were placed under two different thermal conditions,¹¹⁰ so it was necessary to first confirm that UiO-66-AA and UiO-66-BA could indeed be successfully synthesized at 100 °C – if not, then the research could not claim to be representative of conditions at 120 °C.

As per Chapter 1, given the crystalline and porous nature of UiO-66, powder X-ray diffraction and porosimetry can be used to determine whether 100 °C is a reasonable temperature for the syntheses. If the peaks on the diffractograms align and have similar breadth as those formed at elevated temperature, and if the surface areas are in relative agreement, then it can be confidently asserted that the samples constitute the same MOF at both temperatures. If there were a change to topology, the collected diffractogram would show different peak positions, and if there was a loss in quality of the MOF, then the powder X-ray diffractogram would likely be significantly broader, and the surface area would be noticeably lower than the values seen in the literature. It is possible that the powder X-ray diffractogram peaks could show broadening from other factors, such as small particle sizes, so both surface area and crystallinity must be assessed together for the clearest understanding of the MOF's nature.

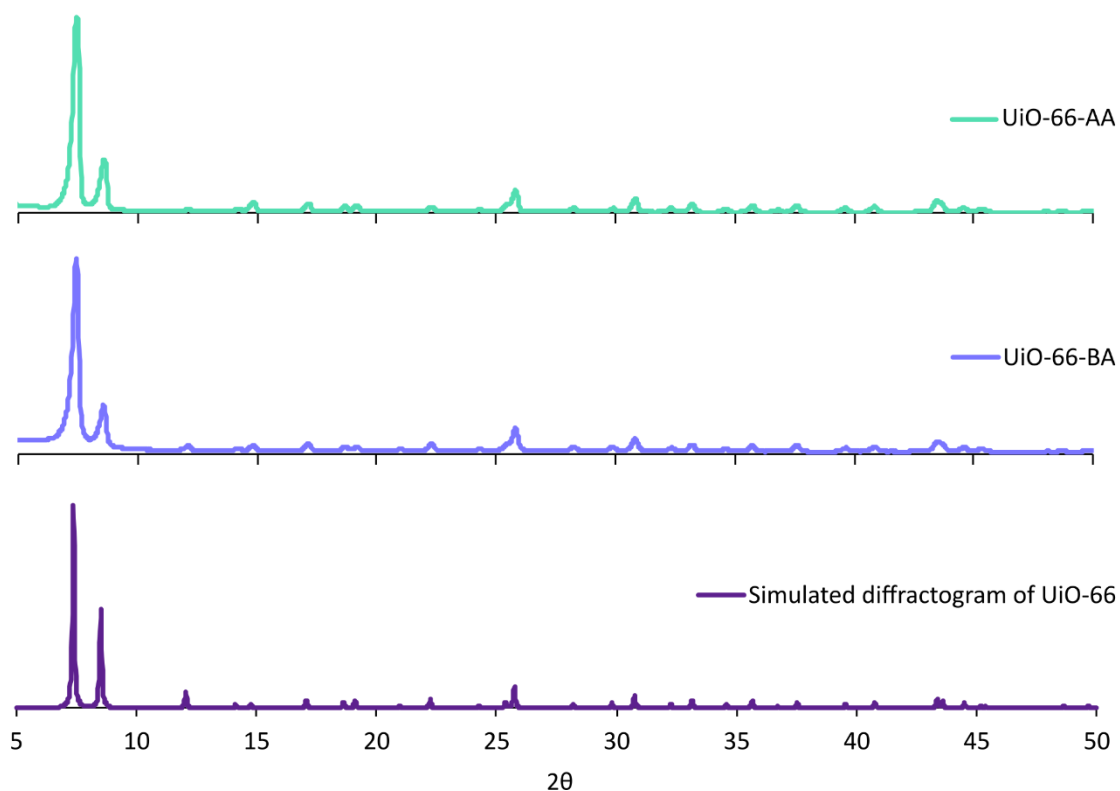


Figure 2.3 Powder X-ray diffractograms of UiO-66-AA and UiO-66-BA synthesized at 100 °C instead of the standard 120 °C, and a simulated diffractogram of UiO-66.

The powder X-ray diffractograms acquired for all samples agreed with the simulated diffractogram of UiO-66 (Figure 2.3), suggesting that all of the samples had the same crystal structure. The BET surface areas, calculated from the nitrogen gas adsorption isotherms at 77 K, were also all consistent with the known range of surface areas associated with UiO-66 (Table 2.3). Given that all important criteria are enforced by these experiments, it can be concluded that UiO-66 was successfully produced at 100 °C using AA and BA as the modulators.

Table 2.3 BET-SA of samples of UiO-66 synthesized at 100 °C instead of the conventional 120 °C.

	BET-SA (m ² /g)	
	Literature (120 °C)	Experimental (100 °C)
UiO-66-AA	1150 ¹⁰¹	1440
UiO-66-BA	1252 ⁷⁹	1720

The experiments involving the pre-conditioning processes could also be suspected of forming different materials, so the same characterization experiments were performed on samples of UiO-66 synthesized with pre-conditioned ZrCl₄ in DMF and modulator. It should be noted that the characterization was not performed for samples of UiO-66 synthesized with just pre-conditioned DMF and modulator – it was assumed that if pre-conditioned ZrCl₄, DMF, and solvent would produce UiO-66 with consistent crystallinity (peak width and position) and nitrogen gas accessible surface area, then pre-conditioned DMF and solvent alone would also produce typical UiO-66. This decision was made in the interest of minimizing waste, as the UiO-66-BA and UiO-66-AA syntheses had poor isolated yields at 100 °C, in part due to the challenge in isolating the MOFs (see Experimental Section 2.5.4).

The powder X-ray diffractograms for the samples synthesized with pre-conditioned ZrCl₄ in DMF and modulator were consistent with simulated diffractogram of UiO-66 (Figure 2.4). The diffractogram for UiO-66-BA does appear to demonstrate broader peaks, which may suggest smaller particle sizes in the BA prep compared to the AA or HCl preps. It could also be indicative of a higher mosaicity, which would suggest a larger number of

defects. However, based on the data below and the difficulty in isolating the product, I believe that it is due to smaller particle sizes.

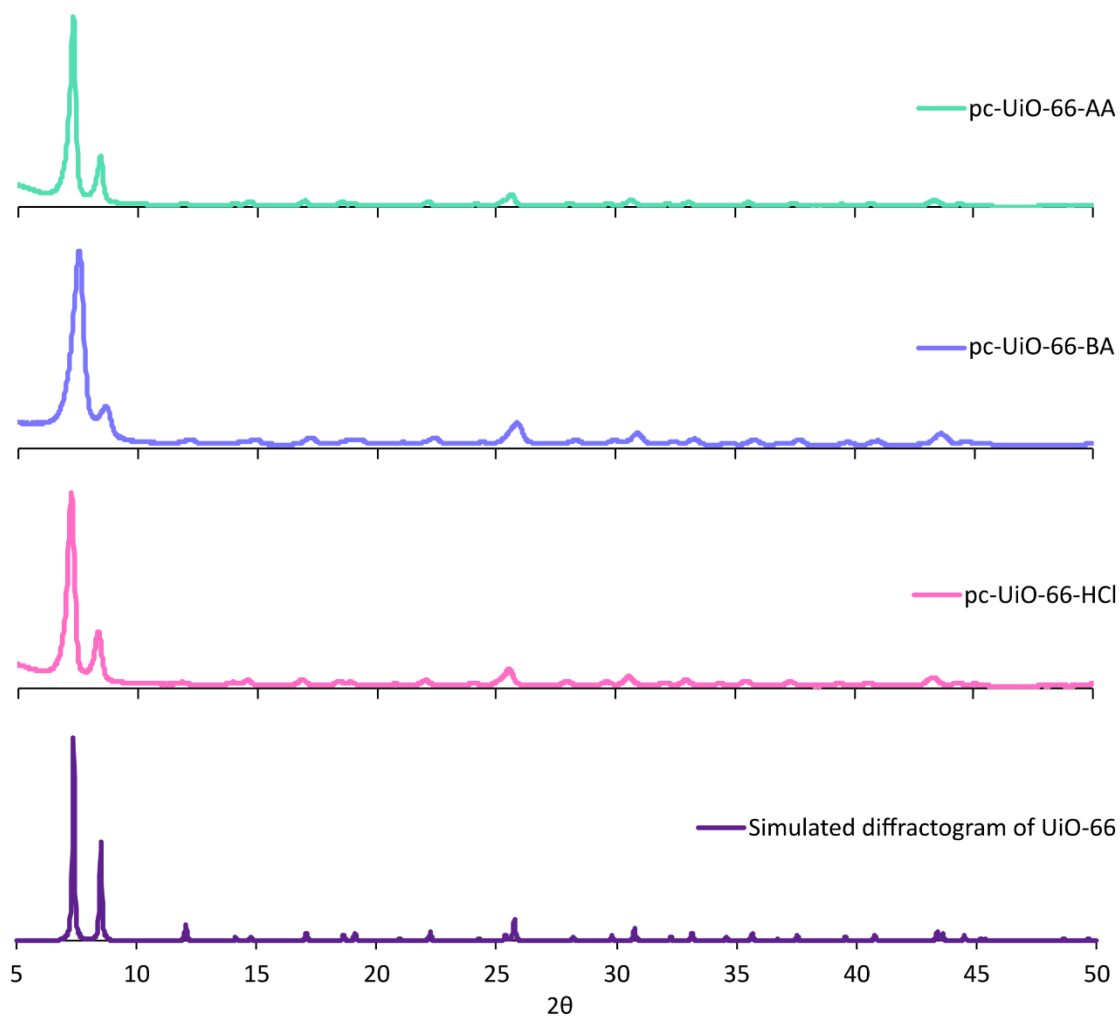


Figure 2.4 Powder X-ray diffractograms of UiO-66 synthesized using pre-conditioned $ZrCl_4$ in DMF and modulator, and a simulated diffractogram of UiO-66.

The calculated nitrogen gas accessible BET surface areas, measured at 77 K, were all consistent with the known range of surface areas associated with UiO-66 (Table 2.4). This suggests that these were indeed the intended MOF, confirming that the pre-conditioning process forms UiO-66, permitting us to evaluate the effect of this variation via 2H -NMR.

It is worth noting that the experimental surface areas seen in Table 2.4 do diverge from the reported values from the literature by more than 10%, however, these are values from other universities who may be using different qualities of reagents than us, who may be using reagents from different retailers than us, and who may be working under different ambient conditions than us. Any of these potential factors could have an impact on the BET-SA of the resulting material, and thus the direct comparison of surface areas is not as reliable a metric when attempting to recreate syntheses from other universities. What is important for confirmation of the successful formation of UiO-66 in our case is the agreement between the experimental and simulated PXRDs, and a surface area between 1000 and 1800 m²/g.

Table 2.4 BET-SA of samples of UiO-66 made via the synthesis with pre-conditioned ZrCl₄ in DMF and modulator.

	BET-SA (m ² /g)	
	Literature (Standard synthesis)	Experimental (Pre-conditioned ZrCl ₄ in DMF and modulator)
UiO-66-AA	1150 ¹⁰¹	1520
UiO-66-HCl	1580 ⁹⁹	1170
UiO-66-BA	1252 ⁷⁹	1680

2.2.2 ²H-NMR Linker data

For all of the syntheses explored, the NMR data did not show direct evidence of any new BDC²⁻-containing compounds being formed. This suggests that any formed speciation had short T_2 values, consistent with large molecular size (i.e., coordination

complexes/polymers, MOF oligomers, or solid formation), and could not be observed by the spectrometer under the conditions used. It is unlikely that a considerable concentration of speciation with short T_2 values was present at the start of the data acquisition given the kinetically inert nature of Zr^{IV} and the induction period observed in the syntheses of UiO-66-AA and UiO-66-HCl (Figure 2.5, Figure 2.6).

2.2.2.1 2H -NMR Linker data for UiO-66-AA

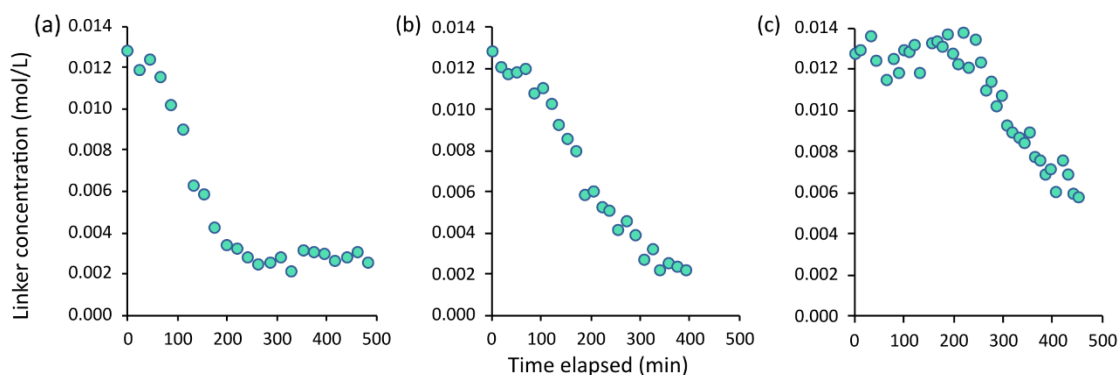


Figure 2.5 Concentration of linker over time for various UiO-66-AA syntheses. (a) Standard synthesis, (b) Synthesis with pre-conditioned DMF and AA, (c) Synthesis with pre-conditioned $ZrCl_4$ in DMF and AA.

In the standard synthesis of UiO-66-AA (Figure 2.5 (a)), the concentration of the linker did not considerably change from its initial value for a period of ca. 60 min before it began to decrease. This induction period indicates that the conditions were not immediately sufficient for the linker to begin coordinating to other materials. There is likely some type of process occurring in the first 60 min that prepares the reaction mixture for linker consumption. Once the induction period has elapsed, consumption of linker begins. The concentration of linker continues to decrease until ca. 210 min, at which point the concentration plateaus. These data can be fitted to a first-order rate model and rate

constants can be determined (see Appendix B), which will aid in the comparison of reaction conditions. The rate constant for the experiment in Figure 2.5 (a) is $-8.4(4) \times 10^{-2} \text{ s}^{-1}$ (Table 2.5).

Table 2.5 Summary of kinetic data for H₂BDC consumption in UiO-66-AA.

	Standard synthesis	Pre-conditioned	
		DMF and AA	ZrCl ₄ in DMF & AA
Rate Constant (s ⁻¹)	$-8.4(4) \times 10^{-2}$	$-5.9(3) \times 10^{-2}$	$-3.5(3) \times 10^{-2}$
Induction period (min)	60	100	240

When the synthesis is performed with pre-conditioned solvent and modulator (Figure 2.5 (b)), the induction period appears to last longer – ca. 100 min – and the reaction rate constant decreases by 30% to $-5.9(3) \times 10^{-2} \text{ s}^{-1}$. This indicates that the solvent is contributing to MOF formation in such a way that the act of reacting the solvent with AA before MOF synthesis slows down the kinetics of MOF formation. It could be that pre-conditioning the solvent with AA allows deprotonation of acetic acid molecules in the reaction mixture. When only solvent and AA are present, this means that these molecules of modulator are prepared to engage in competitive binding as soon as the node forms in solution. When ZrCl₄ is pre-conditioned in solvent and AA, it could be that the presence of acetates and the presence of the acetate-coordinated cluster in solution also lead to slower MOF formation through competition with the linker.

Furthermore, when the solvent is pre-conditioned with ZrCl₄ present as well as the modulator (Figure 2.5 (c)), the reaction rate constant decreases by 58% compared to the standard synthesis – almost double the change seen in the sample of pre-conditioned

solvent and modulator. As well, the induction period before linker consumption begins increases to ca. 240 min, a fourfold increase from the induction period observed in the standard synthesis.

Given the stark contrast between the two pre-conditioning experiments, it is abundantly clear that the addition of ZrCl_4 during the pre-conditioning process has an effect on the subsequent self-assembly of the material. It had been thought that pre-conditioning the ZrCl_4 with solvent and modulator would promote the early assembly of the $[\text{Zr}_6\text{O}_4(\text{OH})_4]^{12+}$ cluster, which would assumedly speed up the subsequent synthesis of the MOF were it already present. This assumption seems to be disputed by these data sets; the process of pre-conditioning led to the sample consuming linker considerably slower than the standard synthesis procedure. If the cluster were forming first, it would follow that the existence of the pre-formed node in solution would lead to more rapid linker consumption given that the node is present at $t = 0$ s. Instead, there is a longer induction period and a slower rate constant. This suggests that either these data dispute the findings by others, or that node formation is not rate-determining and there is a more complex process occurring; the latter is more likely (see below).

2.2.2.2 ^2H -NMR Linker data for UiO-66-HCl

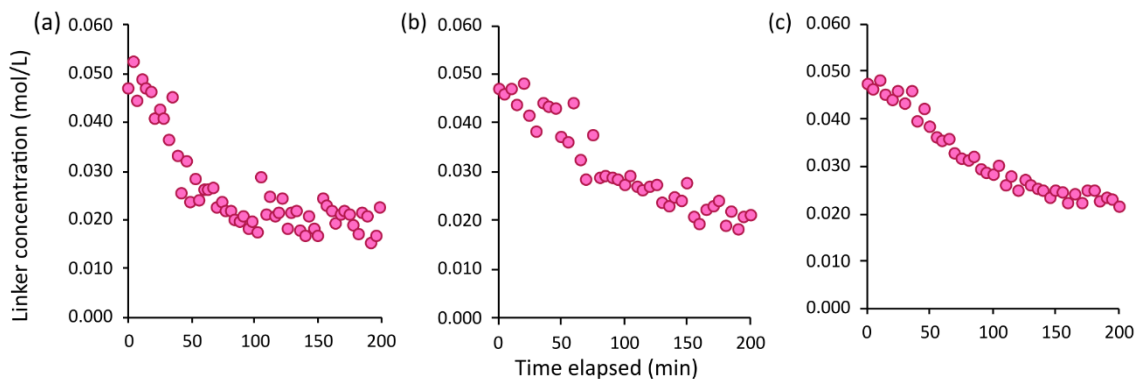


Figure 2.6 Concentration of linker over time for various UiO-66-HCl syntheses. (a) Standard synthesis, (b) Synthesis with pre-conditioned DMF and HCl, (c) Synthesis with pre-conditioned ZrCl₄ in DMF and HCl.

Of note from the UiO-66-HCl linker data (Figure 2.6) is the timescale compared to the data for UiO-66-AA (Figure 2.5); in the standard synthesis case of UiO-66-HCl, linker consumption begins after only 30 min and reaches a minimum at 100 min (Figure 2.6 (a)).

Table 2.6 Summary of kinetic data for H₂BDC consumption in UiO-66-HCl.

	Standard synthesis	Pre-conditioned	
		DMF and HCl	ZrCl ₄ in DMF & HCl
Rate constant (s ⁻¹)	$-10.6(10) \times 10^{-2}$	$-4.3(3) \times 10^{-2}$	$-5.2(3) \times 10^{-2}$
Induction period (min)	30	40	40

The first-order rate constant of the UiO-66-HCl standard synthesis produced the largest magnitude observed in this work ($-10.6(10) \times 10^{-2} \text{ s}^{-1}$; Table 2.6). Given that carboxylates are thought to slow the reaction down due to competitive binding, it follows that by pre-conditioning the UiO-66-HCl synthesis, thereby producing more formate, the rate of linker consumption slows down.

Pre-conditioning the DMF and HCl increased the length of the induction period (Figure 2.6 (b)) and had the largest effect on the reaction rate constant; a decrease of 59% relative to the standard synthesis rate constant was observed. This change makes it apparent that solvent is playing a significant role in the synthesis of UiO-66-HCl.

However, when compared to pre-conditioning DMF and HCl alone, pre-conditioning the ZrCl₄ in DMF and HCl (Figure 2.6 (c)) exhibited no noteworthy change in induction period or rate constant. This lack of change is especially apparent when compared against the change seen in the equivalent case for UiO-66-AA. That is, the two pre-conditioning experiments for UiO-66-AA were markedly different, but the two pre-conditioning experiments for UiO-66-HCl are much more similar than different.

It had been assumed that, in the cases seen so far, the [Zr₆O₄(OH)₄]¹²⁺ cluster was being formed during the pre-conditioning phase with ZrCl₄ in DMF and modulator. For UiO-66-AA, there was a significant difference in the rates and induction periods between the synthesis with pre-conditioned DMF and modulator versus the synthesis with pre-conditioned ZrCl₄ in DMF and modulator. However, the UiO-66-HCl data do not appear to distinguish the two syntheses to the same extent. Either the UiO-66-HCl synthesis proceeds at a similar rate whether or not the [Zr₆O₄(OH)₄]¹²⁺ cluster is formed beforehand, or the cluster is not being formed in this case. If the rate-determining step is not cluster formation, it may even be the case that these data elucidate nothing about cluster formation. Only the slowest process in the reaction mixture can be seen – every process that is quicker will be limited by the slowest one.

When exactly the cluster is being formed during the synthesis of UiO-66-HCl is somewhat contentious in the literature. Xu et al. have reported the rapid formation of the $[\text{Zr}_6\text{O}_4(\text{OH})_4]^{12+}$ cluster when a strong acid is present in solution, as is the case with UiO-66-HCl,⁹² but Semivrazhskaya et al. found no data to suggest the pre-formation of the $[\text{Zr}_6\text{O}_4(\text{OH})_4]^{12+}$ cluster in the synthesis of UiO-66-HCl⁸² – instead, it was believed that zirconium-terephthalate adducts were formed, and as they were hydrolyzed, rapid nucleation occurred.

2.2.2.3 ²H-NMR Linker data for UiO-66-BA

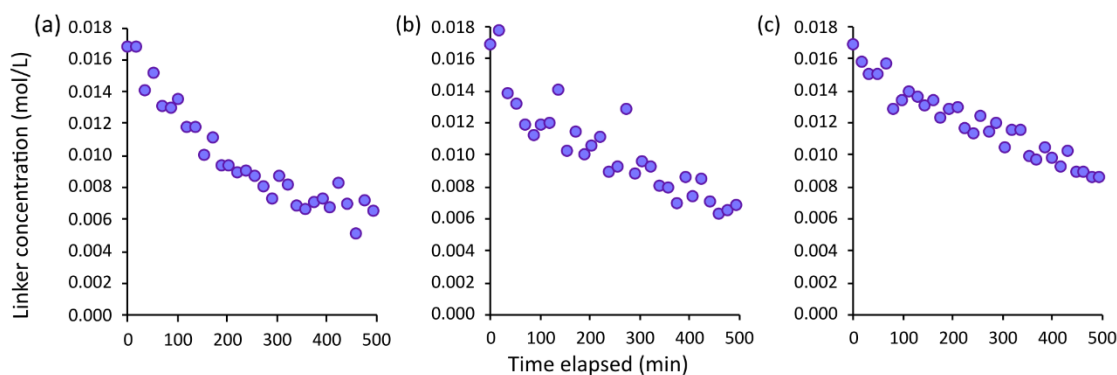


Figure 2.7 Concentration of linker over time for various UiO-66-BA syntheses. (a) Standard synthesis, (b) Synthesis with pre-conditioned DMF and BA, (c) Synthesis with pre-conditioned ZrCl_4 in DMF and BA.

When benzoic acid was used as the modulator, no induction period was observed under any reaction conditions (Figure 2.7). This suggests that the induction period in the UiO-66-AA synthesis is related to acetic acid, coordinated acetate acting as a chelating or $\mu_2\text{-}\eta^1:\eta^1$ bridging linker, the concentration of water associated with the glacial acetic acid, or the notably larger excess of acetic acid in comparison to benzoic acid. Similarly, it suggests that the induction period in the UiO-66-HCl synthesis is related to hydrochloric

acid, DMF hydrolysis (which, if present, would be more rapid under the effects of HCl than BA), the concentration of water in the HCl synthesis, or the strength of HCl as an acid.

Table 2.7 Summary of kinetic data for H₂BDC consumption in UiO-66-BA.

	Standard synthesis	Pre-conditioned	
		DMF and BA	ZrCl ₄ in DMF & BA
Rate constant (s ⁻¹)	$-2.31(12) \times 10^{-2}$	$-1.53(7) \times 10^{-2}$	$-1.14(4) \times 10^{-2}$
Induction period (min)	-	-	-

The rate constant associated with linker consumption for the standard synthesis of UiO-66-BA is 73% smaller than the rate constant for UiO-66-AA's standard synthesis; this is surprising given benzoic acid is in lower concentration and benzoate is a weaker Lewis base than acetate (Table 2.1). This suggests that MOF formation may be limited by dissociation kinetics. As with UiO-66-AA, pre-conditioning the DMF or pre-conditioning the ZrCl₄ in DMF, both with benzoic acid, resulted in a lowering of the rate constant by roughly the same amount as observed for UiO-66-AA.

2.2.3 Time-dependent visual inspection

The synthesis of UiO-66 is known to produce solid sample visible in solution within 12 h (though the reaction is usually allowed to occur overnight for ideal yields); this presented the possibility of following the visual appearance of the reaction over time to cross-check against the ²H-NMR linker data.

For all three modulators, the linker concentration data suggested that the synthesis of UiO-66 was completed “faster” in the case of the standard synthesis as opposed to the case

with the pre-conditioned ZrCl_4 in DMF and modulator. It seemed to follow that MOF would appear in solution sooner in standard synthesis cases.

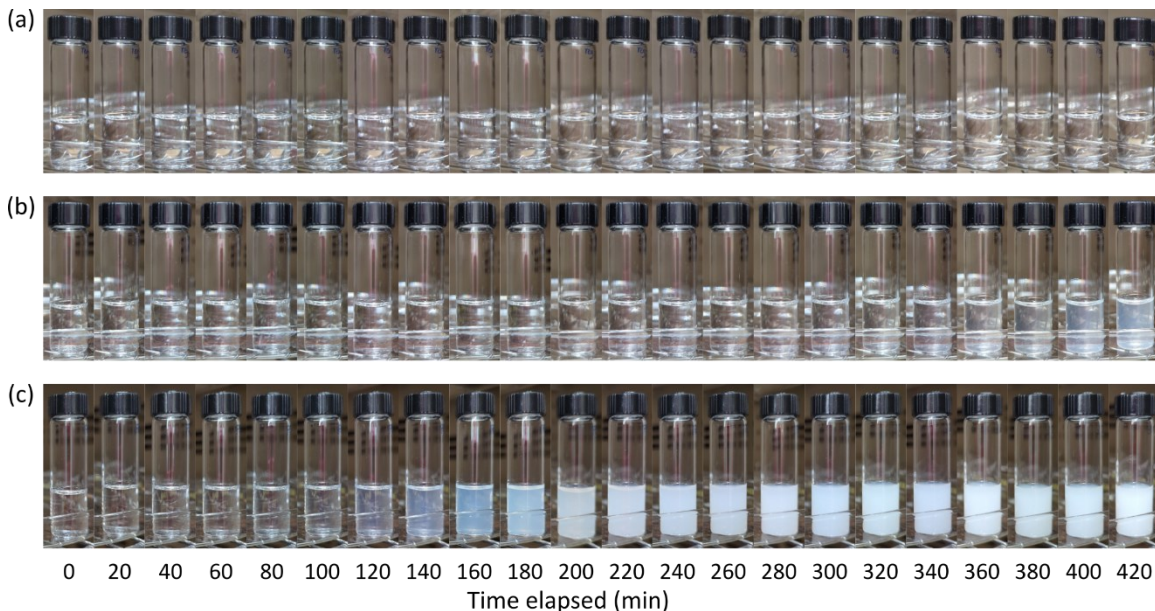


Figure 2.8 Photo images taken at intervals during the synthesis of UiO-66-AA under various conditions. (a) Standard synthesis, (b) Synthesis with pre-conditioned DMF and AA, (c) Synthesis with pre-conditioned ZrCl_4 in DMF and AA.

In fact, the inverse trend became apparent when visual observation experiments were performed with UiO-66-AA (Figure 2.8). After 7 h, the standard synthesis sample of UiO-66-AA had not changed in appearance at all, and the sample with pre-conditioned DMF and solvent had started to become turbid. Interestingly, the sample with pre-conditioned ZrCl_4 , DMF, and solvent produced visible MOF after only 120 min – this was surprising given that the equivalent sample in the ^2H -NMR experiments had a 240-min-long induction period (Figure 2.5 (c)). There is an obvious incongruity here – there is no way MOF can appear in solution before linker has even been consumed. This suggests that the timescale upon which the NMR experiments operate is not necessarily 1:1 with the

timescale in these photo images and, as such, the photo images should only be judged in relation to one another, and not in relation to the overall reaction timeline as determined by NMR.

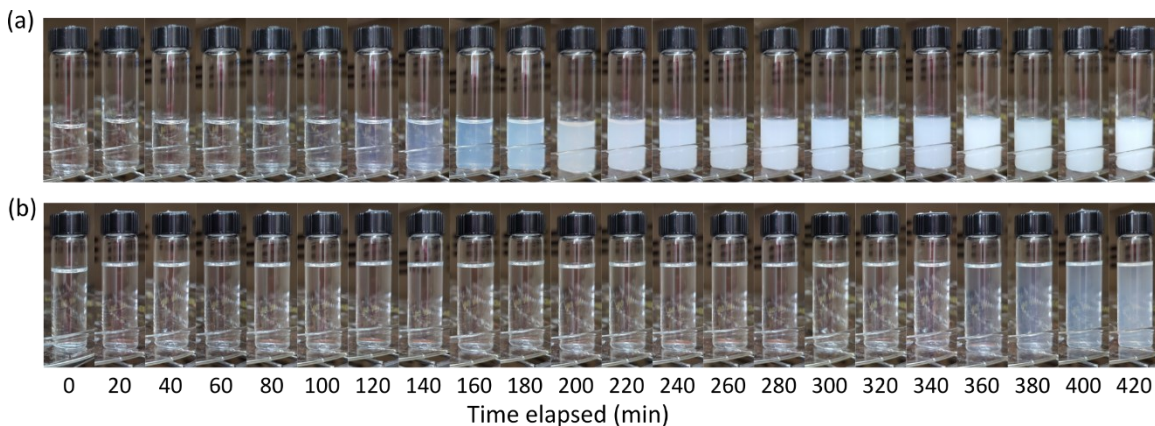


Figure 2.9 Photo images taken at intervals during the synthesis of UiO-66-AA with pre-conditioned $ZrCl_4$ in DMF and AA under various headspace volumes. (a) 5.38 mL of headspace, (b) 2.38 mL of headspace.

The reason for this incongruity between timelines is not immediately clear. However, an initial attempt at collecting time-lapse oven images for UiO-66-AA offered some insight; in that experiment, a larger volume of reaction mixture had been used in the same size of vial, thus producing a diminished volume of headspace. In that experiment, the sample with pre-conditioned $ZrCl_4$ in DMF and AA showed evidence of MOF formation first, but it took 6 h for the MOF to finally appear, as opposed to the 2 h when there was more headspace (Figure 2.9). The only difference in the preparation of samples for these two experiments was the amount of solution dispensed into the 2 dram vial, so reason would suggest that the amount of headspace above the reaction mixture plays a role in the rate of the reaction. It could be the case that the more headspace that is available, the more gaseous products can fit in the sample vial, such as volatile/gaseous products from DMF/formic

acid decomposition. Thus, when the headspace is large, the decomposition of DMF is driven to the right as per Le Chatelier's principle. When the volume of headspace is small, the reaction is less driven towards the right.

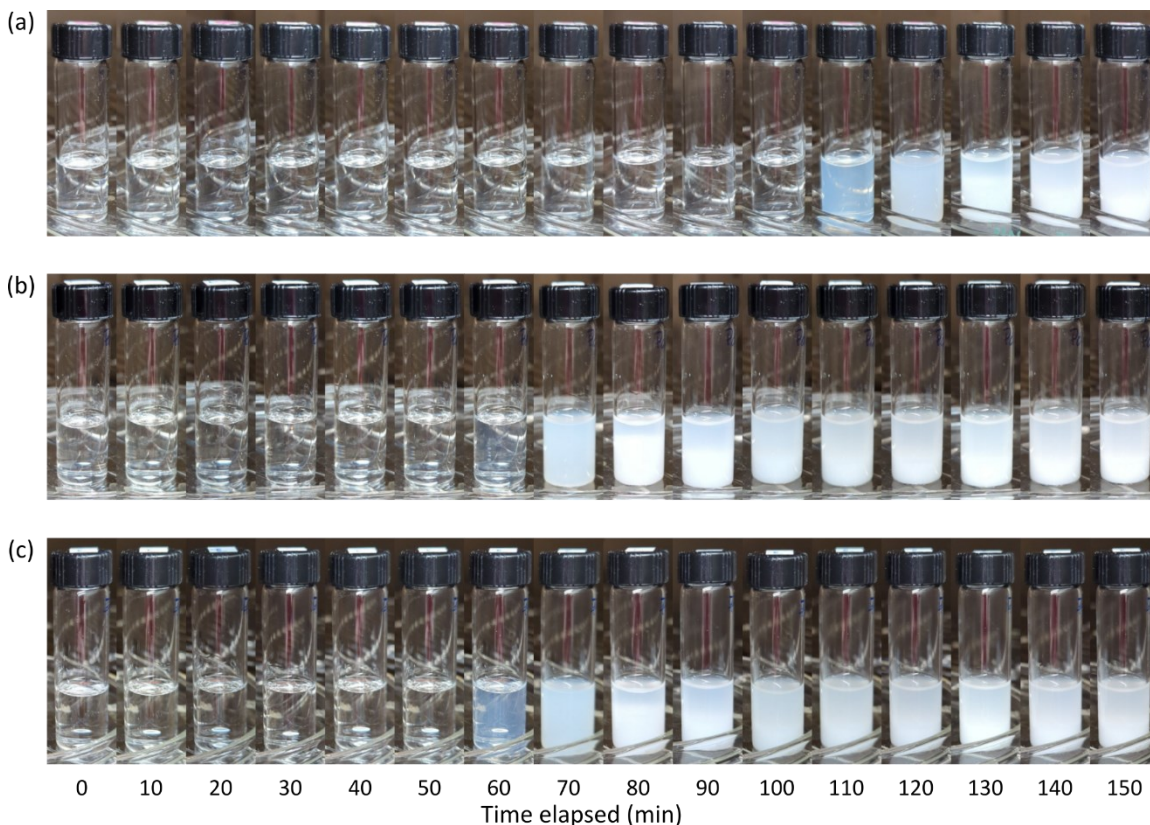


Figure 2.10 Photo images taken at intervals during the synthesis of UiO-66-HCl under various conditions. (a) Standard synthesis, (b) Synthesis with pre-conditioned DMF and HCl, (c) Synthesis with pre-conditioned ZrCl₄ in DMF and HCl.

Notably, UiO-66-HCl appeared in solution at approximately the same time whether the DMF and HCl were pre-conditioned alone or in the presence of ZrCl₄ (Figure 2.10). This is consistent with the similar rate constants observed for the two pre-conditioned syntheses of UiO-66-HCl (Table 2.6). Given that these two syntheses shared similar rate constants and appeared to show MOF forming in the reaction mixture at the same time, there appears

to be a relationship between rate constants and the time at which MOF appears in solution, but it is not a proportional relationship; rather, it appears to be inversely proportional (as with UiO-66-AA). The lower the rate constant, the sooner MOF seems to appear in solution.

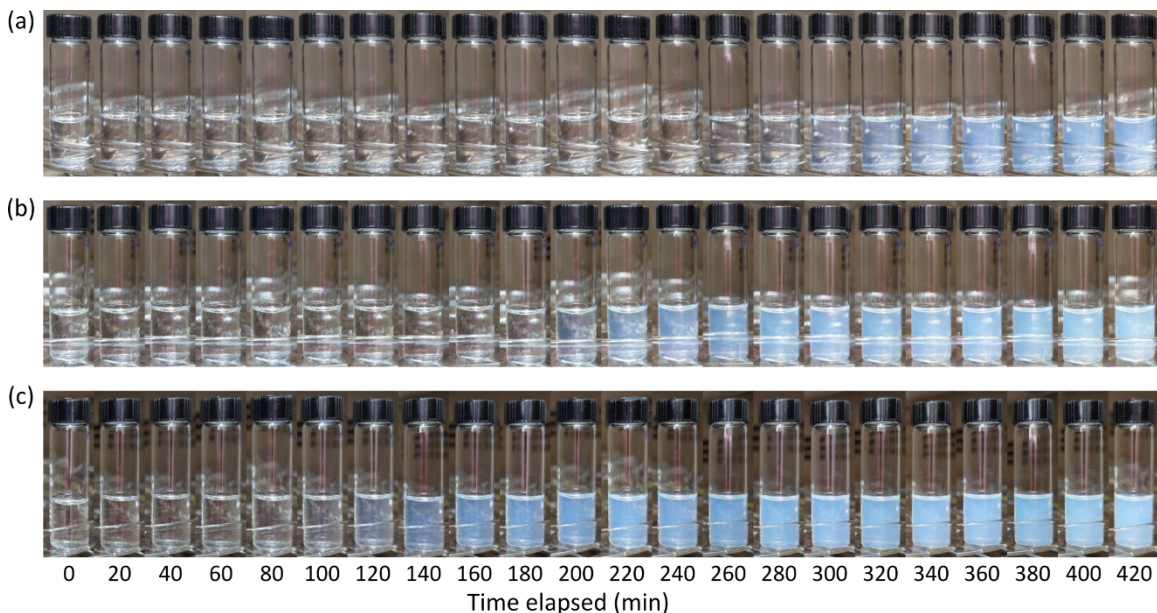


Figure 2.11 Photo images taken at intervals during the synthesis of UiO-66-BA under various conditions. (a) Standard synthesis, (b) Synthesis with pre-conditioned DMF and BA, (c) Synthesis with pre-conditioned ZrCl₄ in DMF and BA.

UiO-66-BA showed the same trend in its data that was seen with UiO-66-AA, but within a time frame that allowed all stages to be seen. In fact, there was a close relationship between the time that MOF appeared in solution and the calculated rate constants. The sample that was pre-conditioned with DMF and BA had a 33% smaller rate constant than the standard synthesis, and the MOF appeared in solution 33% sooner. For the sample with pre-conditioned ZrCl₄ in DMF and BA, the rate constant was 60% smaller than the standard synthesis, and the MOF appeared in solution 51% sooner. This further supports the

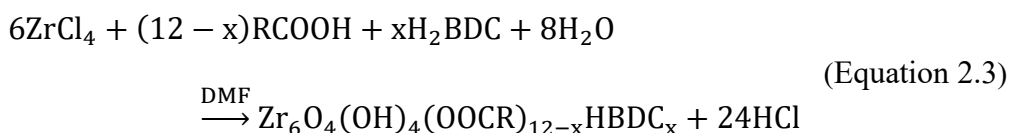
observation that there is indeed a relationship between the rate constants and the time at which MOF appears in solution. It may have been easier to observe this effect for UiO-66-BA than for UiO-66-AA and UiO-66-HCl because the UiO-66-BA synthesis does not have an induction period under any conditions, meaning there was no “overlap” between the induction process and the process of MOF formation in any samples.

Under the effects of the three different modulators, the standard syntheses, despite having larger rate constants, produced visible MOF later than the syntheses that used pre-conditioned reagents.

At this point, the distinction must be made between the time at which a MOF particle has “formed”, and the time at which a MOF particle has become large enough to be visible to the human eye. According to the rate constants, linker was being consumed faster in the standard synthesis cases; it is tempting to describe this behaviour as “MOF is being formed faster”, but the visual data seem to suggest that MOF is forming slower in these cases. Particles become visible to the human eye around a size of 100 μm , so a more accurate way to describe the behaviour is that “MOF is reaching a critical size sooner”. It may be the case that there are oligomers in solution that are not visible to the human eye in the standard syntheses long before MOF visibly appears in solution, but these oligomers are struggling to merge and/or grow into large MOF particles that can scatter visible light and settle in solution. This suggests that nucleation is rapid, but the subsequent growth around the nucleation site is slow or stunted.

2.2.4 D₂O data

Above, focus was placed on how linker is consumed during MOF synthesis, but there are other processes at play that merit investigation. Given that the formation of the node requires the disproportionation of water, and that one of the products of MOF formation is acid (as seen in Equation 2.3, which depicts the formation of UiO-66 from ZrCl₄, linker, and modulator.), the mechanism of MOF formation can be further explored by examining the behaviour of water in the reaction mixture. This was accomplished by adding a small (~15 μL; 0.83 mmol) amount of D₂O to the reaction; this wasn't expected to significantly alter any of the three UiO-66 syntheses. Unlike the linker measurements, which only offered insight into the concentration of linker, the measurements of water can offer insight into two different phenomena in the reaction mixture.



The first of these involves monitoring the chemical shift of the D₂O peak, which provides information about the acidity of the reaction mixture. As a reaction mixture becomes more acidic, the D₂O peak will move to a higher chemical shift (i.e., downfield or deshielded), and if the reaction mixture becomes more basic, the D₂O peak will move to a lower chemical shift (i.e., upfield or more shielded). If DMF hydrolysis is indeed occurring in solution, there should be some evidence of it visible in the changes to the reaction mixture's acidity, which can be followed by the peak shift of D₂O. Insight into the chemical

environment of the reaction mixture is especially useful, as the deprotonation of the linker/modulator is directly impacted by the concentration of protons already in solution.

The second process that can be followed by D₂O produces information regarding the rate of exchange of D₂O (or similarly D⁺ or OD⁻) in solution. This information can be surmised from these ²H-NMR spectra by following the breadth of the D₂O peak; in this case, this was accomplished by monitoring the full width at half maximum (FWHM) of the D₂O peak. On the NMR timescale, a narrow D₂O peak indicates that water is exchanging rapidly, a broad D₂O peak indicates that water is exchanging at an intermediate rate, and the observation of multiple peaks would indicate slow chemical exchange.

2.2.4.1 ²H-NMR D₂O data for UiO-66-AA

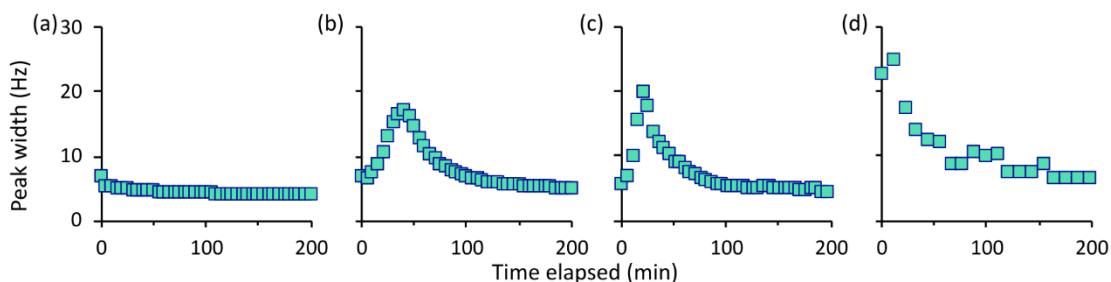


Figure 2.12 Peak width, determined via the full width at half max (FWHM) of D₂O peak over time for UiO-66-AA experiments. (a) DMF and AA alone, (b) ZrCl₄ in DMF and AA, (c) standard UiO-66-AA synthesis, (d) UiO-66-AA synthesis using pre-conditioned ZrCl₄ in DMF and AA.

The process of pre-conditioning DMF and AA is represented in Figure 2.12 (a) – this is the graph that demonstrates what is happening in solution when the solvent is being pre-conditioned in the presence of only modulator. There was nearly no change in the peak width associated with D₂O over 200 min. This illustrates that there is no evidence of

intermediate/slow chemical exchange for D₂O in DMF; this suggests that either hydrolysis of DMF is fast on the NMR timescale or so slow it doesn't visibly occur over the course of the reaction, at least in the absence of the MOF precursors (ZrCl₄ and H₂BDC).

When pre-conditioning ZrCl₄, solvent, and modulator (Figure 2.12 (b)) (i.e., where no MOF can form, but the cluster or pre-cluster could form), a broadening of the D₂O peak was observed before narrowing back to the original FWHM value over 100 min. This breadth started to change almost immediately, with the maximum breadth occurring at approximately 40 min. This implies that a transient speciation is present that has an intermediate chemical exchange with D₂O. As this only occurs when ZrCl₄ is present and is transient, this may be attributed to the formation of the [Zr₆O₄(OH)₄]¹²⁺ cluster. In this case, the water molecules would exchange more slowly as they interact and react with the forming cluster. Once the cluster is formed, the water molecules start to exchange more rapidly again. This suggests that the process of node formation begins almost immediately and is most prominent around 40 min. By 100 min, this process ends. This means that, to distinguish the role that water has on node formation and MOF development, then linker should be added after the pre-conditioning process has elapsed.

When that experiment was performed (i.e., linker was added to a sample that had been pre-conditioned with ZrCl₄, DMF, and AA for 100 min), then the initial peak width was already broad, indicating an initial intermediate chemical exchange with D₂O that sped up over the course of 100-200 min (Figure 2.12 (d)). This suggests that there exists an chemical process over the first 200 min – a similar time to the induction period in Figure 2.5 (a) – that

water/hydroxide/protons are intimately involved in; this process likely requires the linker to be involved and may related to the start of the nucleation process.

In Figure 2.12 (c), the data representing the standard synthesis of UiO-66-AA can be seen. Once again, there is a broadening of the D₂O peak. However, unlike Figure 2.12 (b), this feature is not as smooth and symmetric. It is proposed that both the mechanistic features in Figure 2.12 (b) and (d) are present and overlapping to produce the data in Figure 2.12 (c). This suggests that node formation occurs initially, and the second process takes over as the concentration of the node increases.

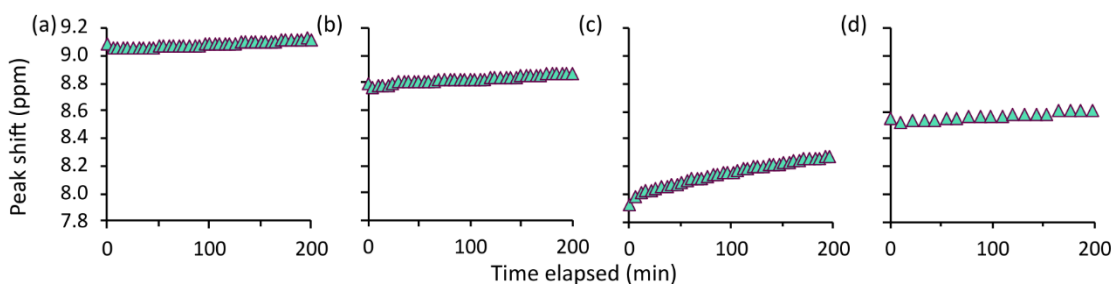


Figure 2.13 Chemical shift of D₂O peak over time for UiO-66-AA experiments at 100 °C.
(a) DMF and AA alone, (b) ZrCl₄ in DMF and AA, (c) Standard UiO-66-AA synthesis,
(d) UiO-66-AA synthesis using pre-conditioned ZrCl₄ in DMF and AA.

Following the chemical shift of D₂O under the same conditions (Figure 2.13), an increase in chemical shift of the D₂O signal (i.e., increasing acidity) over time is observed in all cases. Of the modulators examined, UiO-66-AA produced the most acidic environment. This may explain the surprising observation that under similar conditions UiO-66-AA has a faster rate than UiO-66-BA, despite the 23-fold higher acetic acid concentration than benzoic acid. While there are more acetates to coordinate to the node, there are also more protons/deuterons available to either shift the modulator equilibrium towards acetic acid or

to participate in an acid-assisted dissociative mechanism. This mechanism has been previously observed for kinetically inert cations that need to undergo substitution reactions with strong Lewis bases.¹¹¹ It is possible that the acid-assisted dissociative mechanism is in operation here.

2.2.4.2 D₂O data for UiO-66-HCl

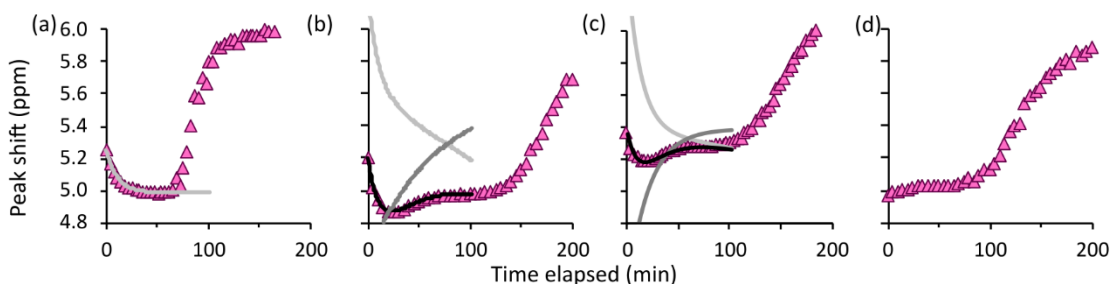


Figure 2.14 Chemical shift of D₂O peak over time for UiO-66-HCl experiments at 80 °C. (a) DMF and HCl alone, (b) ZrCl₄ in DMF and HCl, (c) standard UiO-66-HCl synthesis, (d) UiO-66-HCl synthesis using pre-conditioned ZrCl₄ in DMF and HCl. For fits shown in (a), (b), and (c), see Appendix A.

The change in acidity over time for the HCl experiments appears to illustrate multiple processes (Figure 2.14). For DMF in HCl (Figure 2.14 (a)), an initial exponential decrease in acidity is seen before a plateau is reached. After some critical point, the acidity increases drastically. Given that the HCl used is a strong acid dissolved in water, it is highly likely that the observed changes to acidity in (Figure 2.14 (a)) are due to DMF hydrolysis.

When ZrCl₄ was pre-conditioned with DMF and HCl (Figure 2.14 (b)) or when UiO-66-HCl was synthesized under standard conditions (Figure 2.14 (c)), then there was a minimum in the peak position at ca. 20 min. The dip in these cases is attributed to competing processes. These processes are DMF hydrolysis (exponential decay) and node

formation (exponential growth). These initial features are not observed in (Figure 2.14 (d)) because the DMF has already been hydrolysed during the 50 min pre-conditioning process. In fact, the data in (Figure 2.14 (d)) look like the data from (Figure 2.14 (b)) with the first 50 min of time removed.

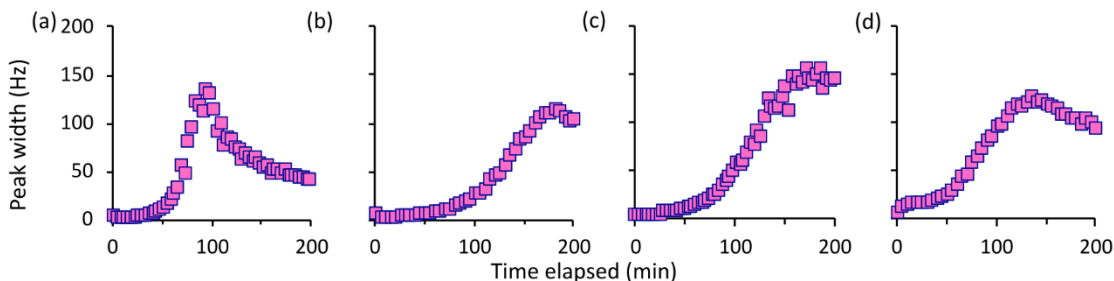


Figure 2.15 FWHM of D₂O peak over time for UiO-66-HCl experiments at 80 °C. (a) DMF and HCl alone, (b) ZrCl₄ in DMF and HCl, (c) Standard UiO-66-HCl synthesis, (d) UiO-66-HCl synthesis using pre-conditioned ZrCl₄ in DMF and HCl.

For UiO-66-HCl's peak width vs. time data (Figure 2.15), no overall trend was observed. In all cases, the D₂O peak began very narrow, broadened over time, and then narrowed again. This is not surprising as the high concentration of HCl would allow for fast H⁺/D⁺ exchange during node formation leading to steady state behaviour. This would remove much of the mechanistic information associated with chemical exchange.

2.2.4.3 D₂O data for UiO-66-BA

In the absence of node/linker precursors, benzoic acid has little effect on DMF (Figure 2.16 (a)). When ZrCl₄ is pre-conditioned with DMF and benzoic acid (Figure 2.16 (b)), however, the D₂O peak broadens over time to reach a maximum at ca. 300 min. This broadening is clearly occurring due to the presence of ZrCl₄, but it is unclear exactly what process this is attributable to. If it was due to DMF hydrolysis, one would expect to see it

in Figure 2.16 (a), as well. Either the broadening seen in Figure 2.16 (b) is not due to DMF hydrolysis, or benzoic acid alone is not enough to drive the hydrolysis of DMF and $ZrCl_4$ is required for the process to occur. Although at this stage it could be suspected that the broadening is related to node formation, the results below will demonstrate that this is unlikely.

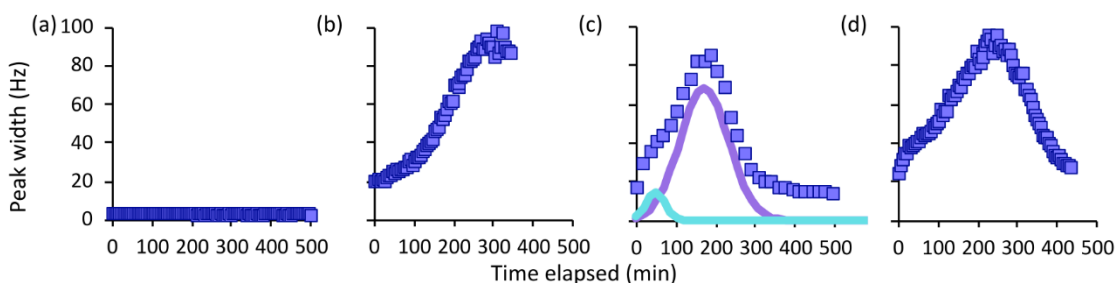


Figure 2.16 FWHM of D_2O peak over time for UiO-66-BA experiments at 100 °C. (a) DMF and BA alone, (b) $ZrCl_4$ in DMF and BA, (c) Standard UiO-66-BA synthesis, (d) UiO-66-BA synthesis using pre-conditioned $ZrCl_4$ in DMF and BA. For fits shown in (c), see Appendix A.

In the case of the standard synthesis (Figure 2.16 (c)), the peak width shows a broad feature at 50 min with a second broad feature at 180 min. As it is not present in Figure 2.16 (b), the former peak appears to be due to the presence of linker and may reflect slow/competitive exchange on the terminal side of the linker. The latter broad feature appears similar to what is observed between DMF and HCl (Figure 2.15), but it does not appear in the case of only DMF and BA, whereas a broad feature does appear in the case of only DMF and HCl.

When the synthesis of UiO-66-BA is performed with pre-conditioned $ZrCl_4$, DMF, and BA, two broad features are again seen (Figure 2.16 (d)). If the process of pre-conditioning $ZrCl_4$, DMF and BA is assumed to form the node, the broad feature seen in Figure

2.16 (b) – (d) cannot be from node formation. If it were, then it shouldn't have appeared in Figure 2.16 (d), since the node would have already formed during the pre-conditioning stage (seen in Figure 2.16 (b)).

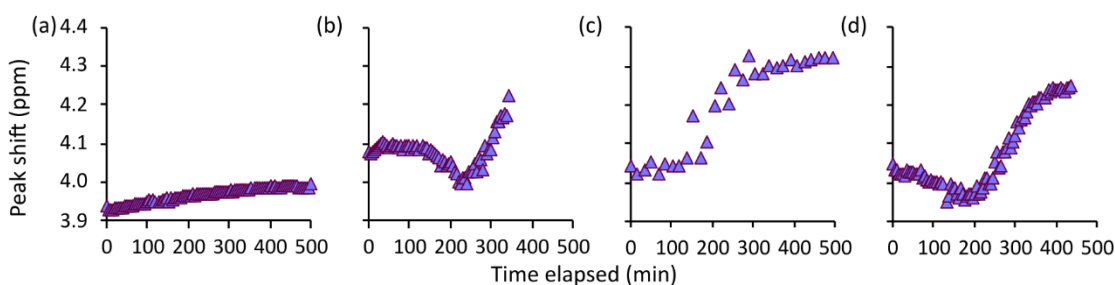


Figure 2.17 Chemical shift of D_2O peak over time for UiO-66-BA experiments at 100 °C. (a) DMF and BA alone, (b) $ZrCl_4$ in DMF and BA, (c) Standard UiO-66-BA synthesis, (d) UiO-66-BA synthesis using pre-conditioned $ZrCl_4$ in DMF and BA.

Much like the FWHM data, when node/linker precursors are absent, benzoic acid appears to have little effect on DMF (Figure 2.17 (a)). However, in the presence of $ZrCl_4$, the acidity data (Figure 2.17 (b)) share features with UiO-66-HCl (Figure 2.14 (b)), such as a period of basification and a period of acidification. If DMF hydrolysis is occurring in Figure 2.17 (b), then it is almost certainly occurring more slowly due to a lower acidity and lower overall water concentration, meaning that the minimum would be observed at a later time. Additionally, node formation may also be slowed down due to the lower water concentration.

Given that in Figure 2.16 (a) and Figure 2.17 (a) there are no changes to acidity or D_2O peak width, the data suggest that either DMF and BA alone are not sufficient to initiate DMF hydrolysis and that hydrolysis is possible only once $ZrCl_4$ has been added, or that the change in peak shift/width is not associated with the process of hydrolysis at all. If the

former is true, it may be because the node itself is Lewis acidic and could potentially be playing the role of the acid catalyst in the process of DMF hydrolysis. If the latter is true, then the changes to peak shift/width would have to be attributed to other processes in the reaction, though there is not a clear answer as to what these processes may be.

2.2.5 Defectivity

As discussed in Chapter 1, MOFs can contain defect sites – that is, sites where a node or linker “should” be, but aren’t. In cases of missing linker, these defect sites located on the node will be capped with alternative compounds to charge balance the node and satisfy the coordination chemistry of the metal. In UiO-66, any carboxylate can act as a capping agent and cap a defect. To assess the defectivity of UiO-66, different analytical techniques can be availed of. As nitrogen gas adsorption isotherms, measured at 77 K, were taken for various samples, the PSDs of these isotherms can be extracted using existing DFT models for nitrogen gas adsorption at 77 K (Chapter 1). When defects are present in UiO-66, a distinctive peak attributed to enlarged pores appears at ~ 18 Å. In addition to the calculation of PSDs, thermogravimetric analysis (TGA) can be employed to determine the number of linkers present in the sample relative to the number of Zr nodes. Both PSDs and TGA were used to assess the defectivity of samples of UiO-66 made by standard synthesis and by pre-conditioning the $ZrCl_4$, DMF, and modulator.

2.2.5.1 UiO-66-AA

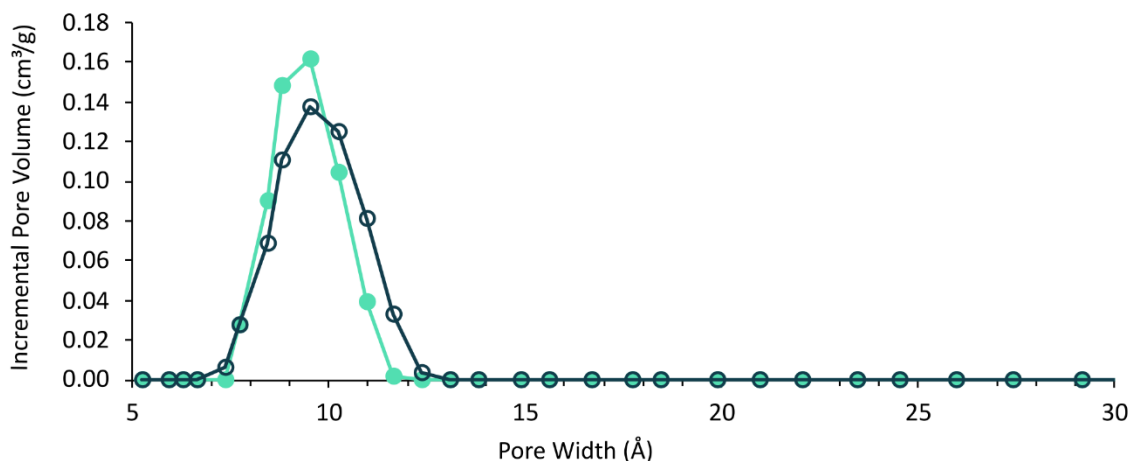


Figure 2.18 Pore size distribution for UiO-66-AA calculated using the Tarazona model. Solid circles represent data from the standard synthesis of UiO-66-AA. Empty circles represent data from synthesis of UiO-66-AA using pre-conditioned $ZrCl_4$ in DMF and AA.

In the case of UiO-66-AA, both the standard synthesis and the synthesis with pre-conditioned $ZrCl_4$, DMF, and AA produced a PSD with a single feature centered around 10 Å (Figure 2.18). This singular feature demonstrates that only one pore around 10 Å was evaluated by the DFT calculations. This pore is the octahedral pore mentioned in Section 2.1.3 – the tetrahedral pore is too small to be seen by the analytical instrumentation used (Micromeritics Tristar). If defects were present in the material, there would be evidence of pores larger than 10 Å due to the defects causing an artificial ‘enlargement’ of the pores. That there are no defects present suggests that acetate is not functioning as a capping agent in these samples of material.

TGA was performed on samples of UiO-66-AA synthesized through the standard synthesis and through the synthesis with pre-conditioned $ZrCl_4$ in DMF and AA (Figure 2.19). The number of defects per node was calculated by the method of Lázaro¹¹² in which the final

mass of the sample after heating is assumed to be pure ZrO_2 and the amount of missing linker is back-calculated from this point; this assumes no missing nodes as well. The number of defects per node in the standard synthesis of UiO-66-AA was determined to be 0.49/6. The number of defects per node in the synthesis with pre-conditioned ZrCl_4 , in DMF and AA was 0.50/6. Furthermore, there is no difference in the number of missing linkers, indicating that these two materials are more similar than different; this is reflected in the PSD data as well.

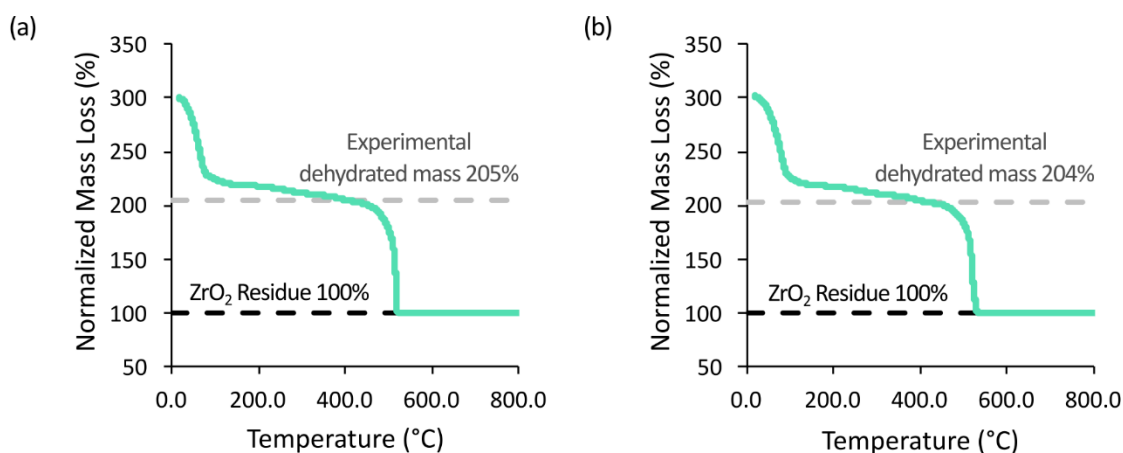


Figure 2.19 TGA of samples of UiO-66-AA. Plateaus used for calculations are denoted with gray dashed lines. (a) Standard synthesis, (b) Synthesis with pre-conditioned ZrCl_4 in DMF and AA.

It is worth noting that neither TGA nor DFT-determined PSDs are perfect methods of assessing defectivity, so it is not necessarily indicative of incongruence that the TGA suggests the presence of defects while the PSD does not. The important takeaway from these data is that the process of pre-conditioning the ZrCl_4 in DMF and AA does not significantly affect the number of linkers in the final MOF sample.

2.2.5.2 UiO-66-HCl

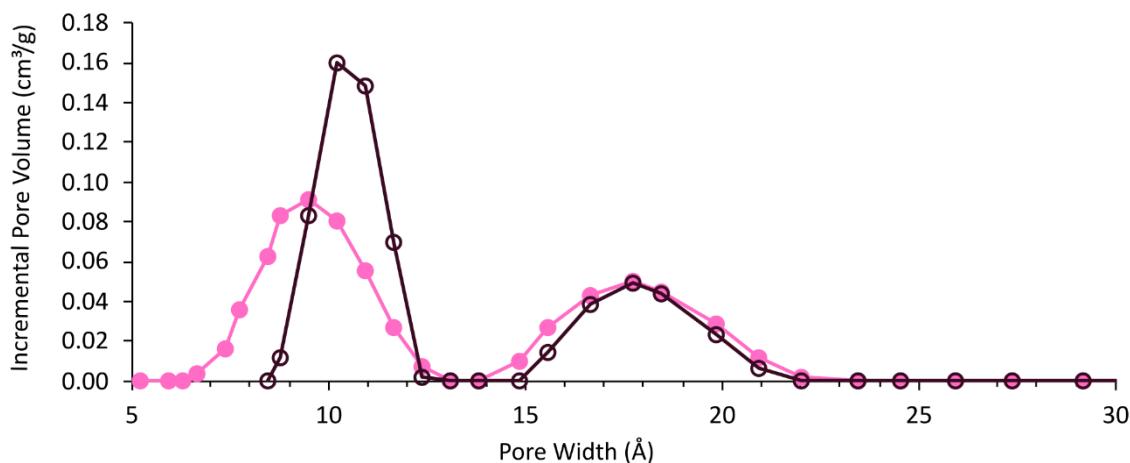


Figure 2.20 Pore size distribution for UiO-66-HCl calculated using the Tarazona model. Solid circles represent data from the standard synthesis of UiO-66-HCl. Empty circles represent data from synthesis of UiO-66-HCl using pre-conditioned $ZrCl_4$ in DMF and HCl.

In the PSDs of UiO-66-HCl (Figure 2.20), a minor decrease in the number of defect-based pores at ca. 17.5 Å relative to the ca. 10 Å octahedral pores was seen. The distribution of the pores around 10 Å also appeared to change – the distribution became tighter when the $ZrCl_4$ was pre-conditioned in DMF and HCl. The area under the curve for each PSD up to 14 Å was calculated, and they were found to be 0.302 for the standard synthesis sample, and 0.338 for the sample with pre-conditioned $ZrCl_4$ in DMF and HCl, which suggests that there are less pores around the size of 10 Å in the standard synthesis sample – likely because there are proportionally more defect pores present. It is unclear why the distribution of the pore narrowed, however.

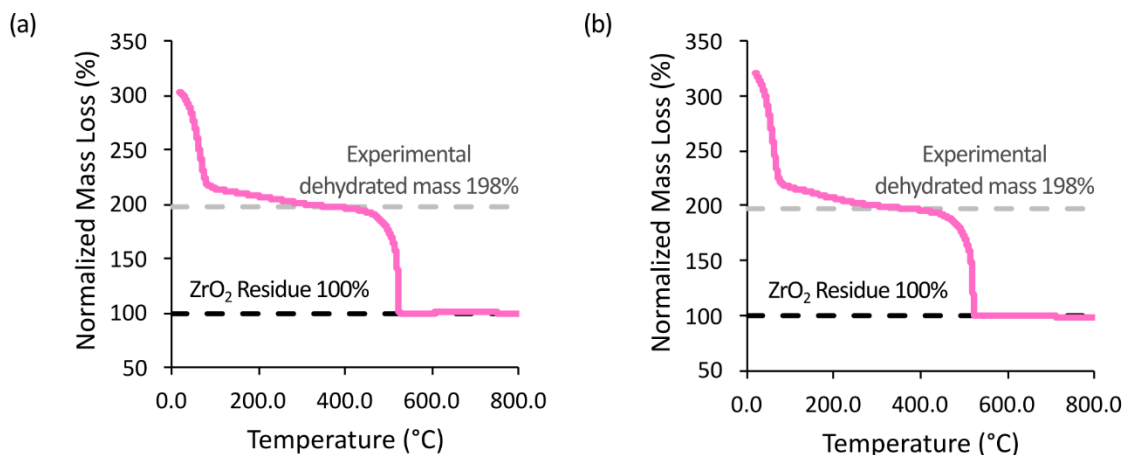


Figure 2.21 TGA of samples of UiO-66-HCl. Plateaus used for calculations are denoted with gray dashed lines. (a) Standard synthesis, (b) Synthesis with pre-conditioned $ZrCl_4$ in DMF and HCl.

When TGA was performed on both samples of UiO-66-HCl (Figure 2.21), the number of defects per node for the standard synthesis was determined to be $1.11/6$, and the number of defects per node for the pre-conditioned sample was determined to be $1.09/6$. This supports the data from the PSD which suggest that the number of defects decreased slightly. Interestingly, we are seeing only $1/6$ missing linkers in these samples, which diverges from the typical $2/6$ seen for UiO-66-HCl. This may be because missing cluster defects are not accounted for in these calculations, or it may be indicative that there is still a lot to learn about these different synthetic procedures.

2.2.5.3 UiO-66-BA

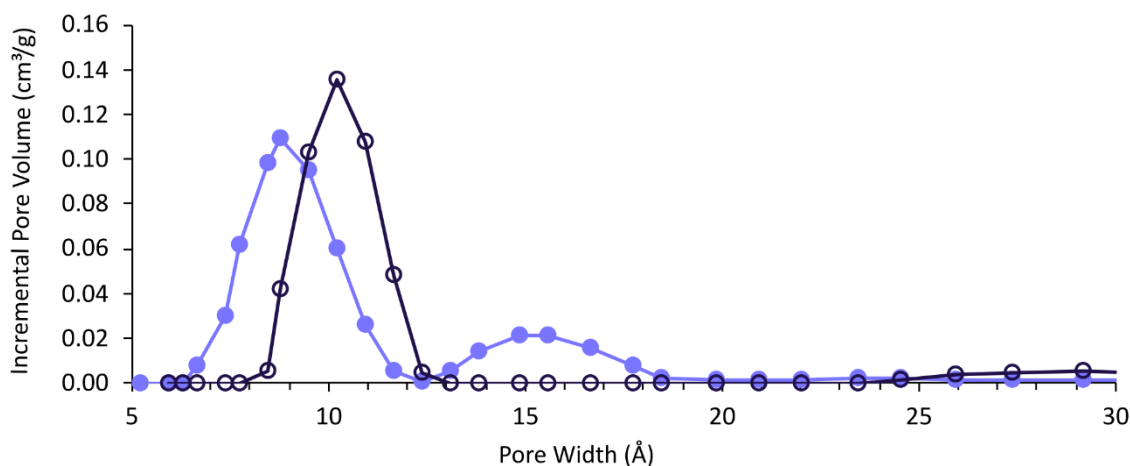


Figure 2.22 Pore size distribution for UiO-66-BA calculated using the Tarazona model. Solid circles represent data from the standard synthesis of UiO-66-BA. Empty circles represent data from synthesis of UiO-66-BA using pre-conditioned $ZrCl_4$ in DMF and BA.

Fascinatingly, UiO-66-BA was found to contain defect-based pores (ca. 15 Å) when produced via standard synthesis, but no defect-based pores when synthesized with pre-conditioned $ZrCl_4$ in DMF and BA (Figure 2.22). Some feature of the pre-conditioning process causes BA or formate to no longer act as a capping agent.

Additionally, the sample with pre-conditioned $ZrCl_4$ in DMF and BA appears to show the presence of mesopores above 25 Å, but these are not true pores – they are indicative of the sample having a high external surface area, causing the software to attempt to justify the resulting change in shape of the isotherm via mesoporosity (see Chapter 3).

The thermograms for the UiO-66-BA samples (Figure 2.23) show a more significant difference than the equivalent thermograms for UiO-66-AA and UiO-66-HCl. The number of defects per node for the standard synthesis was determined to be 1.05/6, which was similar to what was seen with UiO-66-HCl, and the number of defects per node for the pre-

conditioned sample was determined to be 0.45/6, which was similar to what was seen with UiO-66-AA.

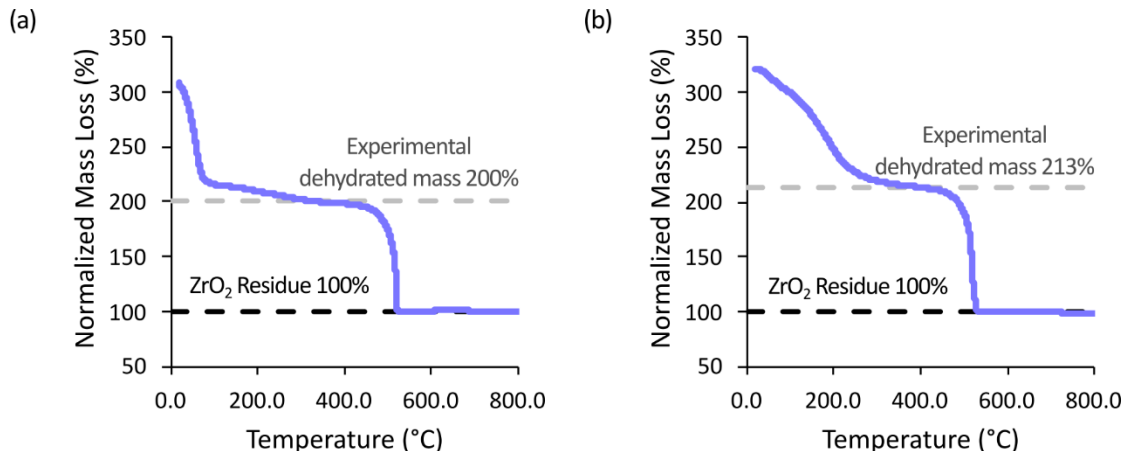


Figure 2.23 TGA of samples of UiO-66-BA. Plateaus used for calculations are denoted with gray dashed lines. (a) Standard synthesis, (b) Synthesis with pre-conditioned ZrCl₄ in DMF and BA.

Again, these data do not perfectly align with the PSDs, but their relative values align with the trend seen in the PSD. That is, the TGA data appear to reinforce the notion that pre-conditioning the ZrCl₄ in DMF and BA before the synthesis significantly reduces the number of defects in the final sample of MOF. Given what has been gleaned from the ²H-NMR data, this difference is likely attributable to the changes to the kinetics of linker consumption.

It is worth putting some of the BA data into context. For the ²H-NMR analysis of linker concentration, we saw the standard synthesis consume linker more quickly than the synthesis with pre-conditioned ZrCl₄ in DMF and BA. The visual inspection, however, indicated that MOF particles reached a critical size the most quickly in the pre-conditioned synthesis. Adding the TGA/PSD data regarding defectivity, we now see a bigger picture of MOF formation. That is, under standard synthesis conditions, linker is consumed rapidly

in order to form a defective MOF that grows in size slowly. When the $ZrCl_4$ is pre-conditioned in DMF and BA, however, the linker is consumed more slowly in order to form a pristine MOF that is able to grow in size more quickly than the standard synthesis. This distinction and context are important for proposing a mechanism of formation, as will be seen in Section 2.3.

2.2.6 SEM

To assess whether the experimental differences between syntheses corresponded with any differences in morphology, SEM images were taken of UiO-66 under the influence of all three modulators made via standard synthesis, and made via pre-conditioned $ZrCl_4$, solvent, and modulator.

2.2.6.1 SEM of UiO-66-AA

The SEM images of UiO-66-AA suggest that the particle sizes in the sample made with pre-conditioned $ZrCl_4$ in DMF and AA were smaller on average than those from the standard synthesis. This is an interesting result, given that the pre-conditioned sample was the first to produce visible MOF in the visual observation experiments (Figure 2.8), which had suggested that it was the first sample to reach a size of 100 μm (i.e., large enough to be seen by the human eye). While it reaches a critical size first, it does not appear to grow as large as the standard synthesis sample. This is consistent with the findings of Taddei et al., who had found pre-conditioning to reduce crystallite size.¹⁰⁵

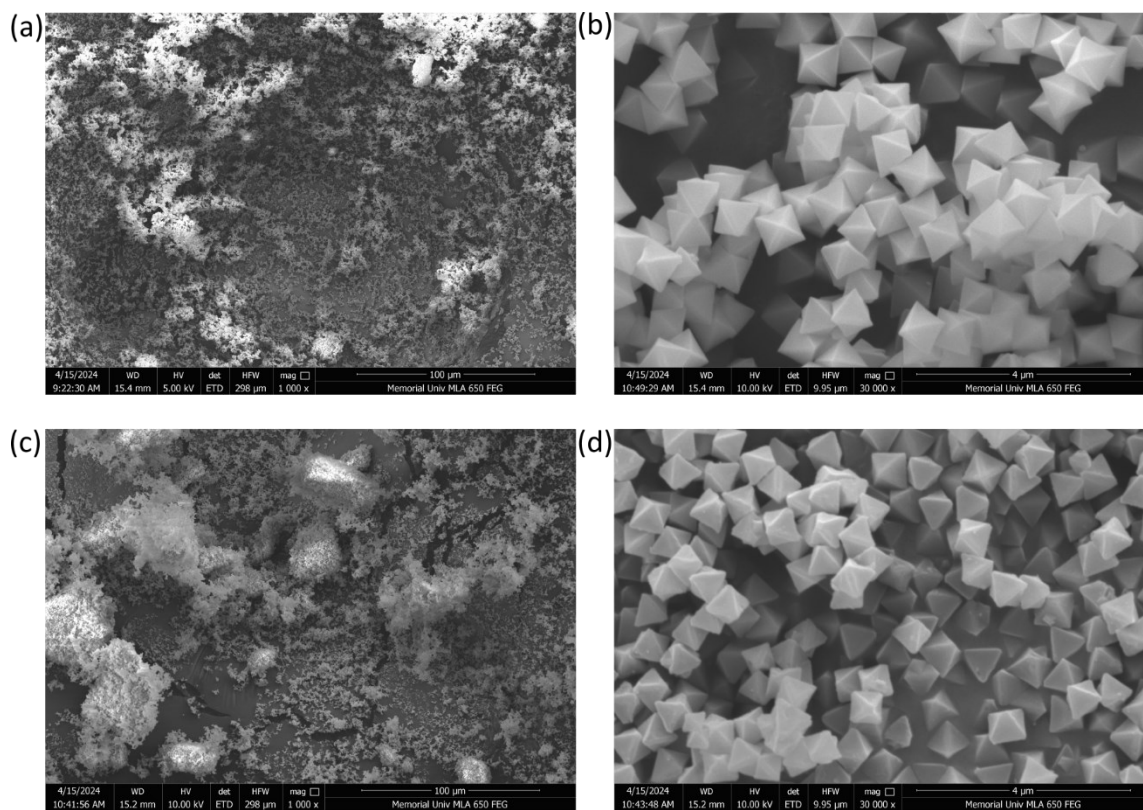


Figure 2.24 Various SEM images of UiO-66-AA: (a) UiO-66-AA made via standard synthesis at 1,000× magnification, (b) UiO-66-AA made via standard synthesis at 30,000× magnification, (c) UiO-66-AA made with pre-conditioned ZrCl₄ in DMF and AA at 1,000× magnification, (d) UiO-66-AA made with pre-conditioned ZrCl₄ in DMF and AA at 30,000× magnification.

2.2.6.2 SEM of UiO-66-HCl

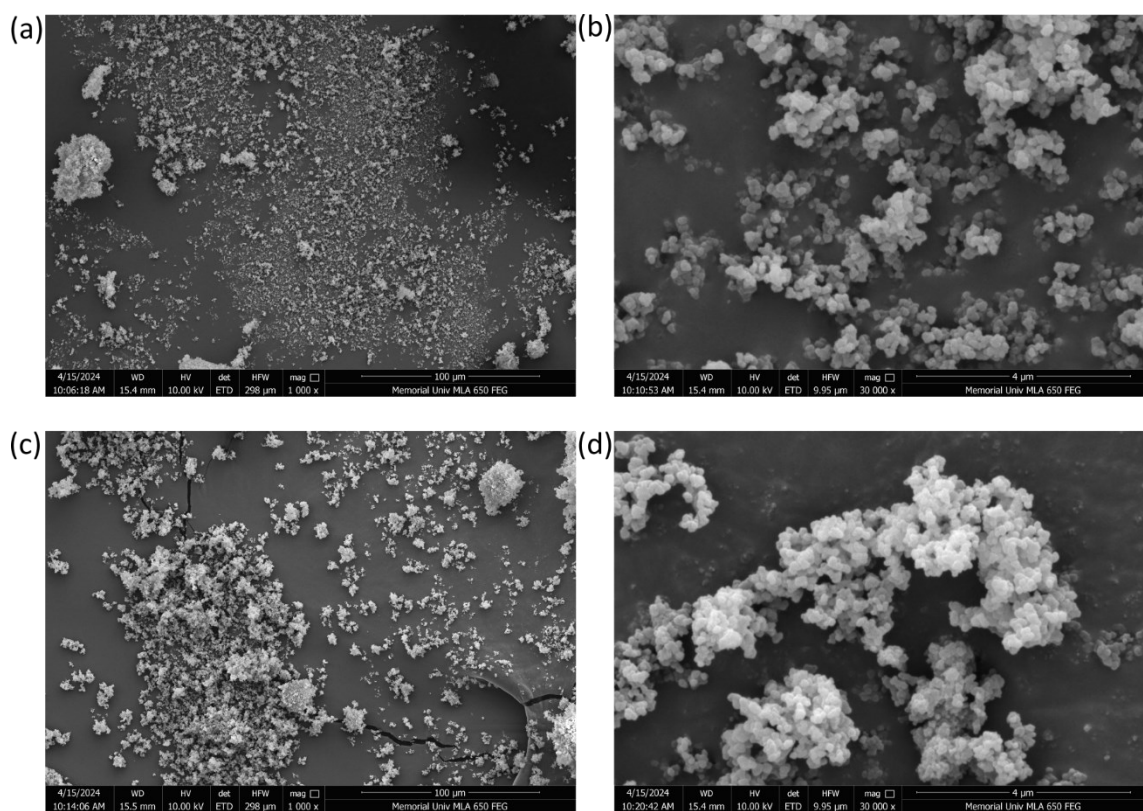


Figure 2.25 Various SEM images of UiO-66-HCl: (a) UiO-66-HCl made via standard synthesis at 1,000 \times magnification, (b) UiO-66-HCl made via standard synthesis at 30,000 \times magnification, (c) UiO-66-HCl made with pre-conditioned $ZrCl_4$ in DMF and HCl at 1,000 \times magnification, (d) UiO-66-HCl made with pre-conditioned $ZrCl_4$ in DMF and HCl at 30,000 \times magnification.

The procured SEM images of UiO-66-HCl seemed to indicate a greater deal of aggregation in the sample made with pre-conditioned $ZrCl_4$ in DMF and HCl compared to the sample made via standard synthesis. The visual nature of the particles made it difficult to assess visually via SEM whether particle size was indeed affected.

2.2.6.3 SEM of UiO-66-BA

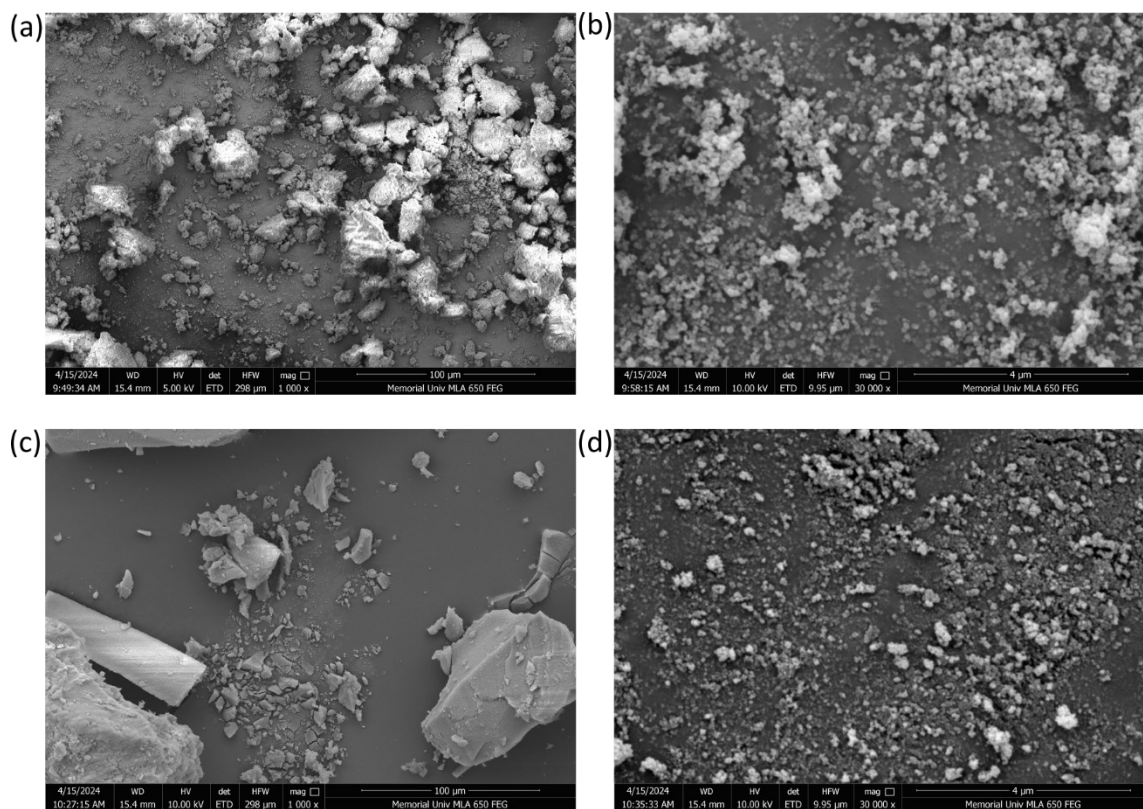


Figure 2.26 Various SEM images of UiO-66-BA: (a) UiO-66-BA made via standard synthesis at 1,000 \times magnification, (b) UiO-66-BA made via standard synthesis at 30,000 \times magnification, (c) UiO-66-BA made with pre-conditioned ZrCl₄ in DMF and BA at 1,000 \times magnification, (d) UiO-66-BA made with pre-conditioned ZrCl₄ in DMF and BA at 30,000 \times magnification.

The physical samples of UiO-66-BA that were produced for observation were markedly more difficult to isolate than their counterparts. Samples of UiO-66-BA produced in bulk had to have their mother liquor mixed with methanol to promote the settling of solid particles in solution by centrifugation. Samples of UiO-66-BA produced via standard synthesis presented as a fine powder with an opalescent sheen. Samples of UiO-66-BA produced using pre-conditioned ZrCl₄, solvent, and modulator presented as a comparatively coarse mix of particles. The pre-conditioned sample appeared as though it

could be comprised of large single crystals, so a sample was taken for XRD. It was discovered to be a packed powder, which was further demonstrated when the large particles began to break apart in the paraffin oil as they degassed.

Both samples of UiO-66-BA produced very fine particles when viewed by SEM (Figure 2.26), but the particles from the pre-conditioned sample appeared to be smaller. This is consistent with the appearance of “mesopores” seen on the pore size distribution, given the high external surface area (Figure 2.22).

2.2.7 Reaction timelines

Reconciling several discrete data sets becomes more complex the more data sets one has. Instead of attempting to superimpose all of the produced graphs, one can instead overlay the reaction’s periods of interest to create a timeline of the reaction. This presents one with a general idea of the major features of the reaction and allows one to see where features line up with one another – it is essentially a neater version of overlaying multiple graphs.

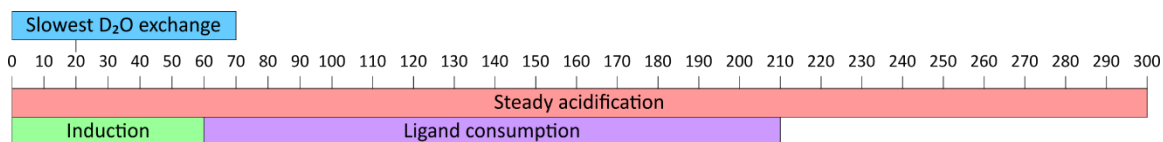


Figure 2.27 A timeline summarizing the collected data regarding the standard synthesis of UiO-66-AA.

In the timeline for UiO-66-AA (Figure 2.27), one feature of note is the fact that the point of slowest D₂O exchange occurs during the early-to-middle of the induction period. If this period of slowest exchange is taken to be the formation of the $[\text{Zr}_4\text{O}_6(\text{OH})_6]^{12+}$ cluster, then what this suggests is that the induction period is not immediately ended by the formation

of the node. As more node is produced, the next step of the synthesis can start to occur – if this next step is slow, it may take time for it to begin.

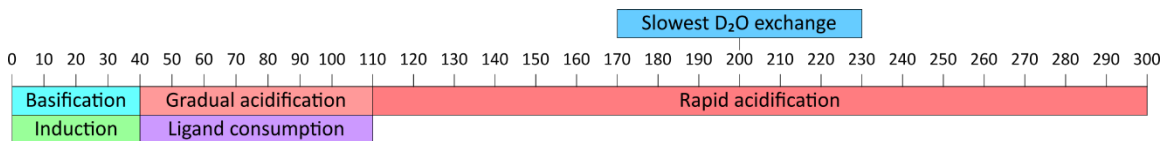


Figure 2.28 A timeline summarizing the collected data regarding the standard synthesis of UiO-66-HCl.

In the first ca. 50 min of the UiO-66-HCl synthesis, the solution basifies, and no linker is consumed. At ca. 50 min, the solution hits a minimum acidity, after which the acidity begins to increase. At the same time, the concentration of linker begins to decrease. At ca. 110 min, the linker concentration reaches a minimum, and the solution rapidly acidifies. During this period of rapid acidification, the rate of D₂O exchange hits a minimum.

The period of decreasing [D⁺] aligns with the induction period. It is possible that one could be caused by the other, or that they are both caused by another factor. Also of interest is the fact that the period of acidification remains gradual as long as linker is being consumed, but that acidity rapidly increases once the consumption of linker has ended.

The point in time in which the slowest D₂O exchange occurs seems to be in the middle of the period of rapid acidification. From Figure 2.15 the peak that is representative of this point of slowest exchange occurred under all four sets of conditions. We know from those data that the peak can't be related to node formation or MOF formation, since it happened when even only DMF and HCl were present, so it is most likely from DMF hydrolysis. It is very interesting to note that this point of highest activity occurs after the initial basification.



Figure 2.29 A timeline summarizing the collected data regarding the standard synthesis of UiO-66-BA.

Notable features of the UiO-66-BA timeline (Figure 2.29) include the two slowest D_2O exchanges occurring during the period of gradual acidification, and the fact that linker consumption occurred throughout the entire process.

2.3 Proposed mechanisms for MOF formation

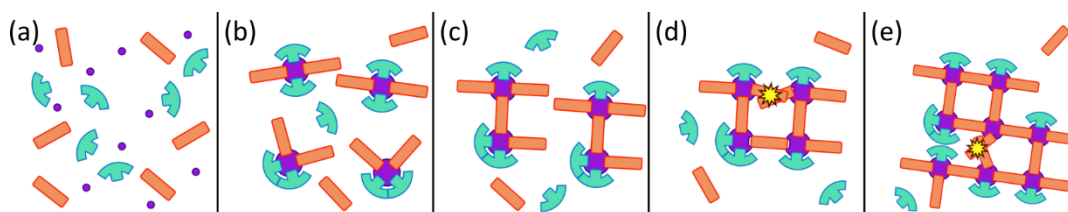


Figure 2.30 Schematic of the proposed mechanisms for the formation of UiO-66 under the standard synthesis conditions. Legend: ligand – orange rectangle; modulator – teal “T”; $Zr/ZrCl_4$ – small purple sphere; $[Zr_6O_4(OH)_4]^{12+}$ node – large purple sphere. (a) Dissolved reaction components, (b) Cluster formation with a mixture of linker/modulator capping groups, (c) Oligomer formation, (d) Ostwald ripening of oligomers forming amorphous materials due to defect regions (yellow stars) occurs rapidly, (e) Additional Ostwald ripening with further defect regions.

The seemingly paradoxical behaviour of MOF appearing faster in the samples with lower rate constants is proposed to be a result of dissociation kinetics being rate-determining in cases where the cluster is preformed. Two pathways for the formation of UiO-66 are thus proposed.

In the standard synthesis, when all the reagents are mixed together (Figure 2.30 (a)), linker and modulator are competing directly for coordination sites as nodes are being formed (Figure 2.30 (b)). Thus, the twelve terminal sites are occupied by a mixture of modulator

and linker. The competitive coordination causes the formation of oligomers with various arrangements of linkers and modulator (Figure 2.30 (c)). When these oligomers attempt to merge, then it is possible for the linkers to arrange themselves such that two linkers attempt to occupy the same space between nodes (Figure 2.30 (d)), creating the necessity for self-healing behaviour. Oligomers with these extra linker defects can continue to grow (Figure 2.30 (e)), but steric inhibition discourages the formation of large, ordered particles until the system can repair these extra linker defects. The defect-repair process is slow and leads to slower MOF particle growth despite a larger linker incorporation rate constant.

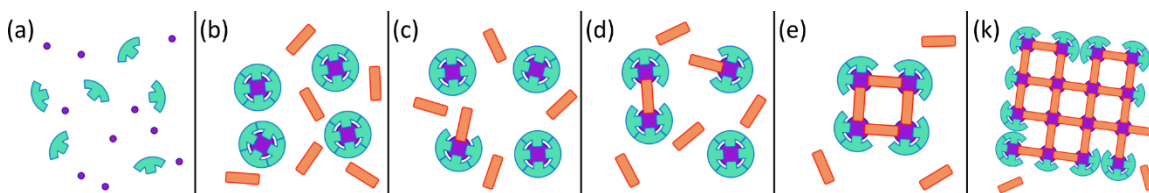


Figure 2.31 Schematic of the proposed mechanisms for the formation of UiO-66 when the $ZrCl_4$ has been pre-conditioned in DMF and modulator. (a) $ZrCl_4$ and modulator dissolved, (b) $Zr_6O_4(OH)_4(modulator)_6$ clusters form during the pre-conditioning step, and linker is subsequently added, (c) Modulators and linkers undergo slow dissociative substitution kinetics, (d) Small oligomers begin to form, (e) The seed/germ forms, (f) Continued growth leads to relatively faster MOF formation.

In the case of the synthesis with pre-conditioned $ZrCl_4$ in DMF and modulator, it is proposed that the nucleation step, and thus the induction step, is not the formation of the node but rather the formation of a MOF oligomer (germ) that is stabilized by a kinetic network effect (Figure 2.31 (e)); this is akin to the chelate/macrocyclic effect. Initially, the $ZrCl_4$ and modulator are pre-conditioned together in DMF (Figure 2.31 (a)) to form the node, decorated with modulator. Then, linker is added (Figure 2.31 (b)). Given that the nodes' coordination sites are already taken up by modulator, the process of attaching molecules of linker to the node is now limited by dissociation substitution kinetics (Figure

2.31 (c)). Oligomers begin to form (Figure 2.31 (d)) through reversible bonding, and at some point, an irreversible oligomer forms (Figure 2.31 (e)). This oligomer, thus termed a “germ”, cannot easily substitute out any of its linkers, as it is stabilized by the kinetic network effect. That is, for any molecule of linker to leave the oligomer, it would need to break its bonds on one end and then the other in rapid succession. After breaking bonds at one end, due to the rigidity of the germ, the linker is not able to pivot away from its original position; thus, its only option is to reform the bond that just broke. These stable germs allow for the MOF to build outwards and more rapidly reach a particle size that is visible to the human eye (Figure 2.31 (f)).

When solvent is pre-conditioned in modulator on its own (i.e., without $ZrCl_4$ present), then the pathway from Figure 2.30 still occurs, but is likely slowed down by the presence of formic acid and dimethylamine. The former acts as an additional modulator while the latter’s pKa strongly favours forming the ammonium cation in solution and thus increases the conjugate base of the carboxylic acids that are present. This serves to slow down the rate of linker incorporation by reducing the acidity.

With the rate-limiting step in the pre-conditioned synthesis shown in Figure 2.31 being modulator dissociation, the need for a defect-repair step doesn’t occur, or occurs to a notably lesser degree, the correct topology forms via slow modulator dissociation and linker substitution.

The proposed mechanism is enforced by the behaviour seen in the defectivity of UiO-66-BA, wherein the standard synthesis produced defects (due to rapid growth of oligomers, as seen in Figure 2.30), but the pre-conditioned synthesis produced a pristine

material (due to controlled growth that is limited by dissociation kinetics, as seen in Figure 2.31).

2.4 Conclusions

When so little is known about the mechanism of MOF assembly, every iota of new knowledge is valuable in honing the success of the process for existing and future MOFs. The work outlined in this chapter has provided crucial insight into what occurs in the reaction mixture during the self-assembly of UiO-66 under the influence of three different modulators. We were able to see the difference in how a coordinating modulator like AA or BA impacted linker consumption compared to a non-coordinating modulator like HCl. The presence of induction periods in the consumption of linker, the relative changes to acidity over the course of the synthesis, and the relative activity of D₂O were all investigated through this work and were contextualized in the greater picture of MOF synthesis. The effect of pre-conditioning various reagents was observed and contrasted across these modulators, which further stressed the nuance in the ways that these modulators influence MOF assembly.

In terms of the first foray into the use of ²H-NMR for monitoring MOF formation, this work was successful in demonstrating that ²H-NMR permits a methodical examination of MOF synthesis. Specifically, where the roles of various components are poorly understood beyond their general importance, in situ ²H-NMR allows for a more rigorous elucidation of each reagent's role.

The methodology illustrated herein can be readily applied to any MOF containing BDC²⁻. This includes MIL-101, MOF-5, MIL-47, MIL-53, or one of the many other crystal structures that contain BDC²⁻. Furthermore, other MOF families can be explored by purchasing and/or modifying existing deuterated linkers (e.g., imidazoles for ZIFs). For larger linkers that cannot be purchased in a deuterated form, synthetic strategies to partially deuterate the molecule (e.g., an aryl carboxylic acid) could be used to acquire the partial ²H-containing form of the linker/pro-linker. If none of these strategies are viable, then other reagents (e.g., modulator, water, solvent) could still be used to probe the mechanism directly or indirectly, through small (10-30 μL) additions of the deuterated versions of these components to the reaction mixture.

2.5 Experimental

2.5.1 Materials and methods

N,N-Dimethylformamide (DMF) and glacial acetic acid were obtained from ACP Chemicals. ACS Grade hydrochloric acid was obtained from VWR Chemicals. ZrCl₄, benzoic acid, terephthalic acid were obtained from Sigma Aldrich. Terephthalic-2,3,5,6-*d*₄ (H₂BDC-*d*₄) acid was obtained from CDN Isotopes. Deuterium oxide (D₂O) was obtained from Stohler Isotope Chemicals. Sodium 3-trimethylsilylpropionate-2,2,3,3-*d*₄ (TMSP-*d*₄) was obtained from MSD Isotopes. All chemicals were used as received, with no further purification.

2.5.2 Synthesis of UiO-66-AA in bulk

UiO-66-AA was synthesized based on the literature prep by Audu and co-workers.¹⁰¹ To a 50 mL Duran® vial, 148 mg ZrCl₄ (0.635 mmol) was added, followed by 10 mL acetic acid (0.175 mol), 104 mg H₂BDC (0.626 mmol), and 40 mL DMF. The mixture was sonicated until it was clear and colourless before being placed in the oven overnight at 100 °C. The standard synthesis occurs at 120 °C, but 100 °C was chosen to replicate conditions in the NMR spectrometer.

2.5.2.1 Synthesis of UiO-66-AA for NMR analysis

To a 25 mL Duran® vial, 37 mg ZrCl₄ (0.16 mmol) was added, followed by 2.25 mL acetic acid (0.0390 mol), 26 mg H₂BDC (0.16 mmol), and 10 mL DMF. The mixture was sonicated until it was clear and colourless. A 1 mL aliquot was drawn from the mixture and a small amount of TMSP-*d*₄ was added to it and sonicated until dissolved. The 1 mL aliquot was transferred to a J. Young NMR tube for NMR analysis at 100 °C.

2.5.3 Synthesis of UiO-66-HCl in bulk

UiO-66-HCl was synthesized according to the prep by Katz and co-workers.⁹⁹ To a 25 mL Duran® vial, 125 mg ZrCl₄ (0.536 mmol) was added, followed by 1 mL 12 M HCl, 4 mL DMF, and 125 mg H₂BDC (0.752 mmol). Then 11 mL DMF was added, and the mixture was sonicated until clear and colourless before it was placed in the oven overnight at 80 °C.

2.5.3.1 Synthesis of UiO-66-HCl for NMR analysis

To a 2-dram vial, 31 mg ZrCl_4 (0.13 mmol) was added, followed by 0.25 mL 12 M HCl, 1 mL DMF, and 31 mg H_2BDC (0.19 mmol). Then 2.75 mL DMF was added, and the mixture was sonicated until clear and colourless. A 1 mL aliquot was drawn from the mixture and a small amount of $\text{TMSP-}d_4$ was added to it and sonicated until dissolved. The 1 mL aliquot was transferred to a J. Young NMR tube for NMR analysis at 80 °C.

2.5.4 Synthesis of UiO-66-BA in bulk

UiO-66-BA was synthesized based on the literature prep outlined by Atzori and co-workers.⁷⁹ To a 25 mL Duran® vial, 80 mg ZrCl_4 (0.34 mmol) was added, followed by 335 mg of benzoic acid (2.74 mmol) and 57 mg H_2BDC (0.34 mmol). 20 mL of DMF was then added. The mixture was sonicated until it was clear and colourless before being placed in the oven overnight at 100 °C. The standard synthesis occurs at 120 °C, but 100 °C was chosen to replicate conditions in the NMR spectrometer. The final product was unable to be isolated by centrifugation alone, so the mother liquor was mixed 1:1 with methanol during isolation to encourage flocculation.

2.5.4.1 Synthesis of UiO-66-BA for NMR analysis

To a 2-dram vial, 20 mg ZrCl_4 (0.086 mmol) was added, followed by 83 mg of benzoic acid (0.68 mmol) and 14 mg H_2BDC (0.084 mmol). 5 mL of DMF was then added, and the mixture was sonicated until the solution was clear and colourless. A 1 mL aliquot was drawn from the mixture and a small amount of $\text{TMSP-}d_4$ was added to it and sonicated until

dissolved. The 1 mL aliquot was transferred to a J. Young NMR tube for NMR analysis at 100 °C.

2.5.5 Pre-conditioning solvent and modulator

For several experiments, the solvent was “pre-conditioned” before being used in MOF synthesis. This is to say that the solution and the respective modulator were placed in the oven at synthesis temperature for a length of time before being removed, allowed to cool, and subsequently used in the reaction.

The lengths of time chosen for the pre-conditioning process for each solvent were based on our preliminary results and did not end up necessarily representing the ideal period over which pre-conditioning would occur.

For pre-conditioning UiO-66-AA experiments, DMF and acetic acid were heated for 3 h at 100 °C. For pre-conditioning UiO-66-BA experiments, DMF and benzoic acid were heated for 4 h at 100 °C. For pre-conditioning UiO-66-HCl experiments, DMF and HCl were heated for 1 h at 80 °C.

2.5.6 Pre-conditioning ZrCl₄ in solvent and modulator

Similar to the above process, for several other experiments, the solvent was “pre-conditioned” in the presence of ZrCl₄, which was believed to promote the formation of the Zr₆O₄(OH)₄¹²⁺ cluster in solution. This was accomplished by heating solvent, modulator, and ZrCl₄ in the oven for a length of time before removing the sample, allowing it to cool, and subsequently using it in the reaction.

The lengths of time chosen for this process are the same as for the solvent pre-conditioning process. That is, for pre-conditioning UiO-66-AA experiments, DMF and acetic acid were heated for 3 h at 100 °C. For pre-conditioning UiO-66-BA experiments, DMF and benzoic acid were heated for 4 h at 100 °C. For pre-conditioning UiO-66-HCl experiments, DMF and HCl were heated for 1 h at 80 °C.

2.5.7 High resolution ^2H -NMR

All NMR data were collected on Bruker Avance II spectrometer using the lock channel of a triple-tuned TXI probe operating at 600 MHz (92.15 MHz for ^2H). The time-resolved experiments were collected using a zg2H pulse sequence, with 64 scans and 4096 time-domain points, 1.1 s acquisition time, D1=0.1 s relaxation time and a multizg_2d au_program.

NMR data were processed in MestReNova ver. 14.2.1. The spectra obtained were referenced to the deuterium TMSP- d_4 peak at 2.44 ppm.

Ligand concentrations over time were determined by using MestReNova's Reaction Monitoring plug-in to create concentration graphs. The concentration of the TMSP- d_4 was assumed to stay constant over the course of the reaction and the chemical shift and integration of the linker and D_2O were determined relative to TMSP- d_4 . The plots obtained from MestReNova were subsequently converted to concentration by using the initial concentration of H_2BDC used in the synthesis. Further details on the process of acquiring ligand concentrations can be found in Appendix C.

2.5.8 Quantities of ^2H reagents used

For NMR experiments meant to observe H_2BDC , 100% of the reagent used in the synthesis was in its ^2H form. That is, to monitor H_2BDC in any synthesis, all the H_2BDC added as a reagent was of the form $\text{H}_2\text{BDC}-d_4$.

To monitor H_2O , 12 μL of D_2O was added to the 1 mL aliquot of reaction mixture drawn for NMR analysis.

2.5.9 MOF activation

For bulk MOF synthesis, after the sample was removed from the oven and cooled, the reaction mixture was transferred to a 50 mL centrifuge tube. The MOF was isolated by centrifugation and the mother liquor was decanted. Then 15 mL DMF was added, and the centrifuge tube was shaken. The sample was centrifuged and the DMF was decanted. This DMF wash was repeated two more times. Then 15 mL methanol was added, and the centrifuge tube was shaken. The sample was centrifuged, and the methanol was decanted. This methanol wash was repeated two more times. Then, the tube was placed in the oven overnight at 80 $^\circ\text{C}$ to dry.

The next day, the sample was transferred to a pre-weighed Micromeritics Tristar tube.

All samples were activated on a Micromeritics Smart VacPrep by evacuating the sample at a rate of 5 mmHg/s for 60 min. Then, the sample was heated at a rate of 5.0 $^\circ\text{C}/\text{min}$ until it reached 150 $^\circ\text{C}$, where it was held for 180 min.

2.5.10 Nitrogen gas adsorption isotherms

Nitrogen gas adsorption isotherms (77 K) were taken on a Micromeritics TriStar II instrument. Surface areas were calculated by BET theory using the Micromeritics Microactive software suite, ensuring that the four-point criteria were met for all samples. Pore size distributions were determined using DFT with the Tarazona model within the Micromeritics Microactive software suite.

2.5.11 Powder X-ray diffraction

Powder X-ray diffraction data were collected using a Rigaku MiniFlex 600 with a Cu-target sealed-tube X-ray source and a D/teX Ultra 2 detector. The source was operated at 40 kV/15 mA. Samples were collected from 5-50° in 2 θ using a step size of 0.02 at a rate of 10°/min.

2.5.12 Scanning electron microscopy

Scanning electron microscopic images were collected on a FEI MLA 650FEG at 10.00 kV. Samples were gold coated using a SPI-Module Sputter Coater prior to analysis.

2.5.13 Thermogravimetric analysis

Thermogravimetric analysis data were collected using a TA Instruments Discovery TGA 55. Samples were heated at a rate of 10 °C/min up to 900 °C under air.

Chapter 3

Refining and Exploring the Synthesis of a Phthalocyanine MOF

3.1 Introduction

The ability to install a variety of organic molecules into a MOF by introducing attachment points at symmetrical locations is part of what has inspired the wide range of applications available to MOFs. Since these families of ligands, based off of different rigid cores, can introduce unique properties to the MOFs in which they are installed, there are many such families being researched, and new ones always being developed. New ligand families will almost certainly have different ideal conditions for their syntheses than existing families, and thus experimentation is necessary to probe the limits of the synthesis space and identify the necessary conditions required to incorporate these new ligands into the MOF structure.

One of the main challenges with developing these new syntheses is the lack of a clear indicator of when the synthesis has been successfully optimized. Typically, the crystal structure of the MOF can be used to estimate an upper limit to the surface area, which can then be used to guide the research, but this requires the existence of a crystal structure of the material. This is not always easy, and can take up to a decade to procure, as in the case of UiO-66.

This chapter illustrates many of the challenges associated with the development of MOFs featuring new linkers through attempts to optimize the synthesis of a MOF featuring a novel phthalocyanine linker.

3.1.1 Porphyrins

Porphyrins are a naturally occurring class of macrocyclic compounds featuring four pyrrole rings bonded to one another via methine bridges (=CH-) (Figure 3.1). Porphyrins and their derivatives are found all over nature – from heme in blood to chlorophyll in plants – due to the utility provided by their photosensitivity as well as their ability to coordinate a metal atom in their centers. Different metal atoms beget different properties for the resulting porphyrin, contributing to the wide range of applications seen for these macrocycles.

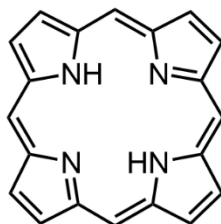


Figure 3.1 Metal-free porphine, the simplest porphyrin. All other porphyrins share this macrocycle.

It is no wonder that porphyrins have made their way into MOFs as organic linkers. As was discussed in the intro (Section 1.2.2), porphyrins have all the necessary features to become linkers. Their macrocycle functions as a rigid core, and the methine carbons are ideal locations for attachment points such as carboxylic acids, pyridines, and phenylamines. The attachment of such groups can easily convert porphyrins into ditopic (two-connected) and tetratopic (four-connected) linkers (Figure 3.2). Their ubiquity, utility, and ease of

synthesis have allowed a great many porphyrins to become macrocyclic linkers in MOFs, such as PCN-222, PCN-224, and NU-902.

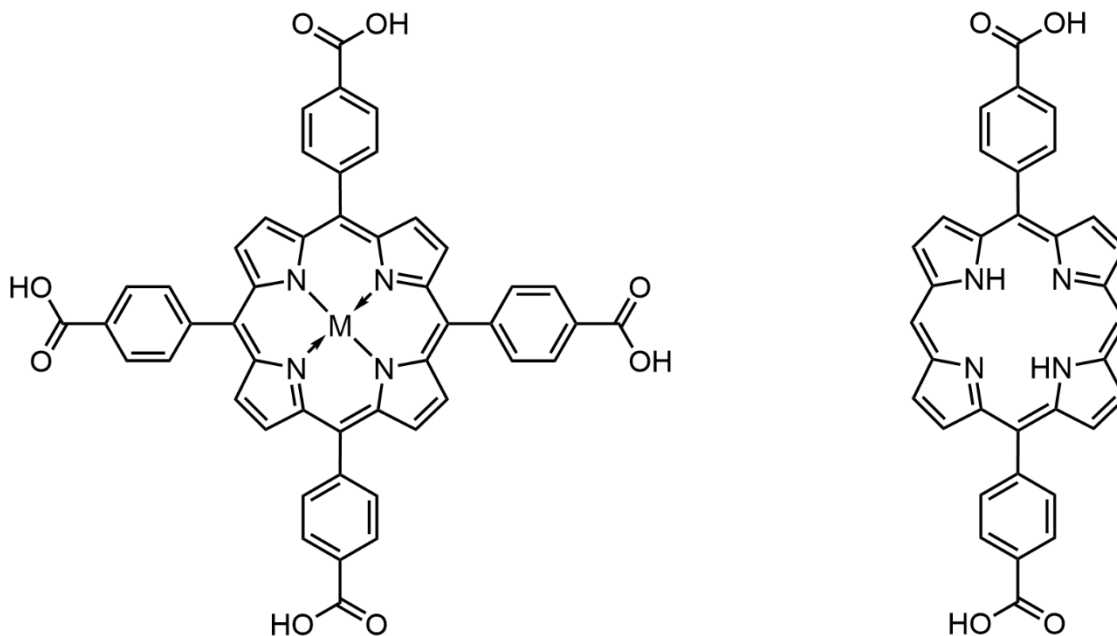


Figure 3.2 Two porphyrinic pro-linkers used in MOFs. Left: H₄TCPP(M). Right: H₂DBP(H₂)

3.1.2 Phthalocyanines

Phthalocyanines (Pcs) are a class of compounds that bear a structural resemblance to porphyrins but, unlike porphyrins, which occur naturally, phthalocyanines are entirely synthetic chemicals.

The most striking feature of phthalocyanines is arguably their vivid colour, which led to their initial employment as a pigment and dye. Copper phthalocyanine (CuPc), which when used as a pigment is referred to as phthalo blue (Figure 3.3, left), is a popular colorant in paint, due largely to the vivacity of its hue, but also due to other outstanding features of phthalocyanines. UV and visible light stability, superb thermal stability, and resistance to

a range of pH values make phthalocyanines a popular choice for conditions that may face intense weathering – car paint and tattoo ink are famous examples. Installing chlorine atoms on all the β carbons of copper phthalocyanine (Figure 3.3, right) leads to a bathochromic shift in the absorption spectrum, giving the material a green hue. Appropriately, the resulting pigment is called phthalo green.

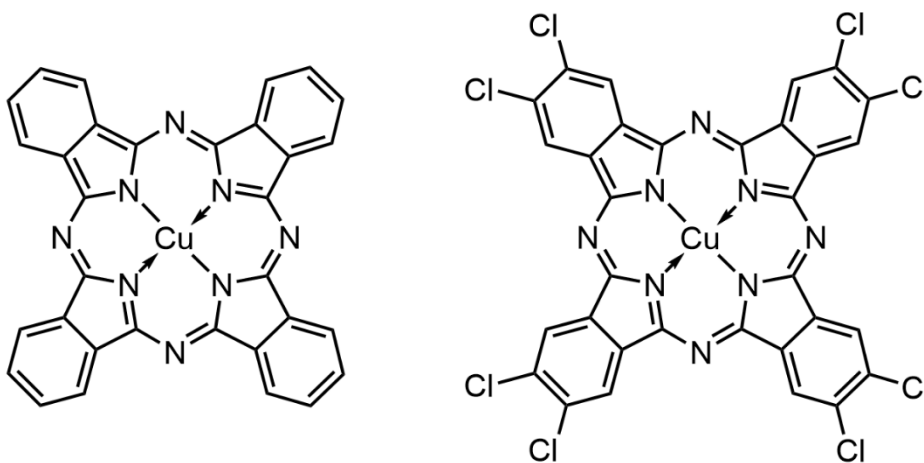


Figure 3.3 The chemical structures of the phthalocyanines used to give pigment to the oil paint colours known as phthalo blue (left) and phthalo green (right).

Since their inception, many applications for phthalocyanines have been found that make use of the molecule's exemplary features. The primary driving force of a great deal of this research stems from the high extinction coefficients of phthalocyanines; this makes them highly desirable for light-responsive fields, such as photocatalysis,¹¹³ photovoltaics,¹¹⁴ and photodynamic therapy.¹¹⁵ For comparison, the extinction coefficient of copper phthalocyanine¹¹⁶ ($10^5 \text{ M}^{-1} \text{ cm}^{-1}$) is approximately an order of magnitude larger than $\text{Ru}(\text{bipy})_3^{2+}$, a well explored photophysical complex,¹¹⁷ and N719, a common photosensitizer in dye-sensitized solar cells.¹¹⁸ Much like porphyrins, phthalocyanines can coordinate a metal ion in their center, and a thoughtful choice of metal can enhance certain

effects and tailor the compound for more specific actions. For example, when Fe is coordinated inside a Pc, it acts as a redox-active center, allowing FePcs to mimic heme-like reactivity.¹¹⁹

The exemplary stability of phthalocyanines is owed in part to their system of 18 π electrons, which help to provide them their characteristic pigment; unfortunately, these same electrons, along with the planar geometry of the molecule, often contribute to π - π stacking in phthalocyanines. This stacking causes particle aggregation, which can hinder the applicability of the material, and contributes to poor overall solubility. Aggregation makes it hard to process the material, and it can diminish or eliminate the expected properties. If a phthalocyanine is being used for catalysis, it will only be able to perform catalysis using the outer shell of the aggregate, at best. At worst, the presence of aggregated phthalocyanines could render the catalyst inactive. Many of these and other pitfalls typical of phthalocyanines could be avoided if they could be kept from aggregating. Consequently, there are many factors to take into consideration when seeking to employ phthalocyanines in different applications (e.g., MOFs).

3.1.3 Phthalocyanine MOFs

Phthalocyanines would find higher effectivity and perhaps even broader applicability if their usage was not hindered by π - π stacking-induced aggregation. In the interest of ameliorating these challenges, many researchers have attempted to immobilize phthalocyanines by forcing them into orientations that eliminate, or at least greatly reduce, aggregation. This has historically been done by incorporating Pcs into other structures,

such as including them in composite films,¹²⁰ or decorating them on the outside of a MOF.^{121,122}

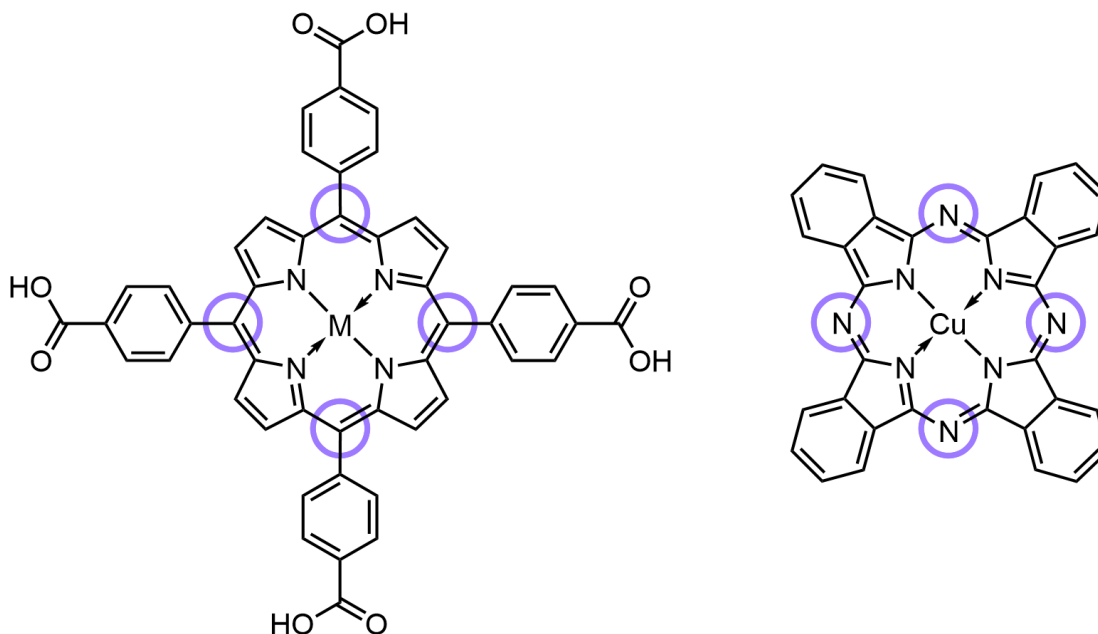


Figure 3.4 Tetrakis (4-carboxyphenyl) porphyrin, a common porphyrinic linker (left), and a typical phthalocyanine (right). Note the phthalocyanine's N atoms preventing the attachment of additional moieties at those locations (indigo circles).

Phthalocyanines can also be immobilized by their incorporation into the actual crystal structure of a MOF; the inclusion of a phthalocyanine in a MOF as the sturdy core of an organic linker offers many benefits to the resulting material. In the case of photocatalysis, for example, a MOF with a phthalocyanine incorporated into its structure would have an enormous advantage over a membrane. Phthalocyanines in a membrane may settle in aggregated pockets and may not be regularly ordered, thus retaining some of the original pitfalls of phthalocyanine use. The crystalline nature of MOFs, however, necessitates that any phthalocyanines incorporated into the structure are regularly ordered and thus more easily accessible. Every pore inside of the MOF would become a site for catalysis

(assuming the reaction compounds can penetrate the pores), enhancing the utility of the material by expanding the surface area.

In Chapter 1, the essential features of a linker were stressed: A linker must have a rigid core and a symmetrical arrangement of attachment points. Despite the structural similarities between porphyrins and phthalocyanines, there is little literature featuring phthalocyanine-containing linkers in MOFs, while there has been copious amounts of research into porphyrinic MOFs.³⁸ The cause of this discrepancy lies in the attachment points. Porphyrins provide two or four ideal sites where attachment points can be installed (Figure 3.4, left); this is why porphyrins are readily converted into potential linkers (pro-linkers). Phthalocyanines, by comparison, do not have an easy location where attachment groups can be installed; the equivalent location on the phthalocyanine has a nitrogen atom, which has no substitution positions left, barring it from usage (Figure 3.4, right). The only practical locations for new moieties are on the eight beta peripheral positions of the outermost benzene rings. However, unlike porphyrins where two of the four methine groups can be substituted to make a linear (i.e, ditopic) linker, there is no easy synthetic pathway that results in only two or four of the eight beta peripheral positions being utilized to form a symmetric pro-linker. As illustrated below, phthalocyanines can be formed from the cyclization of four 1,2-dicyanobenzene (phthalonitrile) subunits. If the phthalonitrile contains one additional functional group (e.g., a benzoic acid subunit), then several isomers are possible. Some of these isomers may be good pro-linkers for MOFs. However, separation of these isomers may be challenging due to the low solubility and aggregation of phthalocyanines.

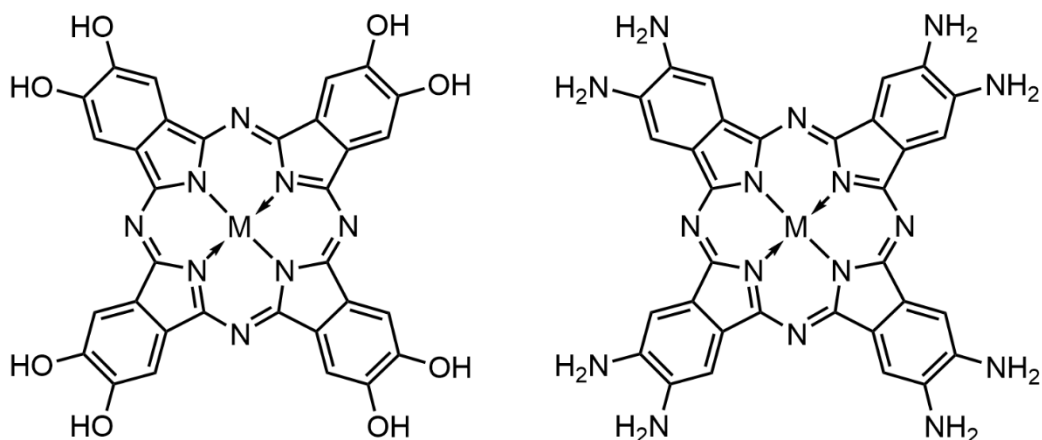


Figure 3.5 The two existing phthalocyanine-based linkers that have appeared in MOFs in the literature. M = Ni,^{123–126} Cu,^{126–128} Co.^{129–131}

The published works involving PcMOFs have navigated this issue in two main ways. In several cases, all eight of the beta positions are substituted to provide the linker with four catechol moieties^{124,125,128–131} (Figure 3.5, left). In all other cases, the phthalocyanine linker is synthesized so that amine groups occupy those eight beta positions to create o-phenylenediamine groups^{123,126,127} (Figure 3.5, right). Thus far, all 2D PcMOFs have featured a single atom as their node, such as Ni, Fe, Co, and Cu; the similar linker moieties and single-atom nodes cause all of these MOFs to exist as flat sheets. The only 3D PcMOF to date features a Fe trimer as its metal node.¹³¹

These strategies for the incorporation of a phthalocyanine into a MOF are innovative, but the linkers they produce are not as highly customizable as porphyrins or other common MOF linkers. If one needed a larger pore in their MOF, then they must ask themselves, “How can this phthalocyanine linker be lengthened?” One could extend the outermost groups into naphthalenes, but that would still lead to the same possible arrangement of attachment groups, which would produce the same flat topology. As discussed in Section 1.2.2, an

ideal linker would allow for readily accessible synthetic strategies to create longer linkers (e.g., BDC vs. BPDC) or create different distributions of attachment points (e.g., BDC vs. BTC) in order to increase pore size, as per the isorecticular principle.

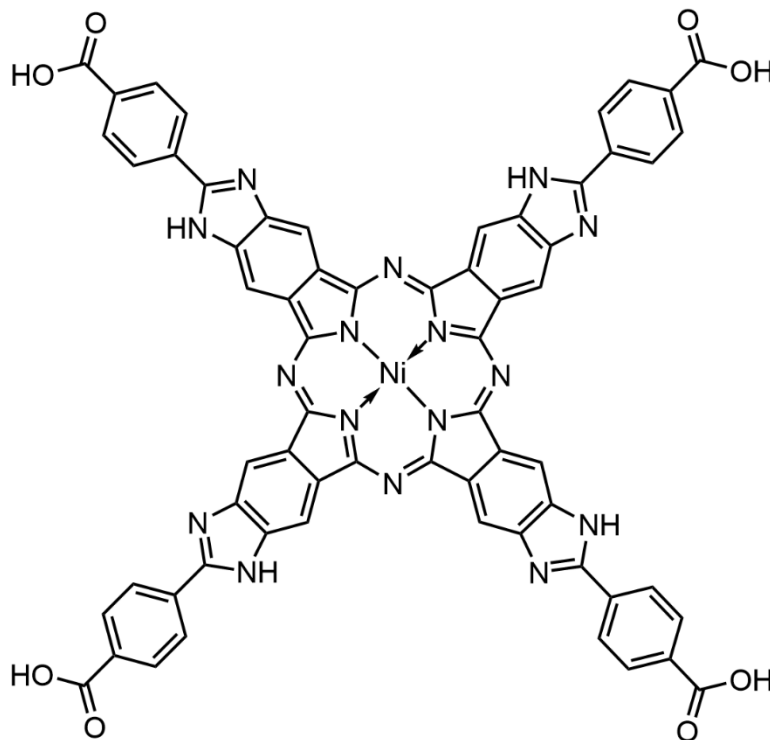


Figure 3.6 The phthalocyanine linker synthesized by Dr. Mohsen Shayan during his PhD.
M = Co, Ni.

One of the Katz group's previous students, Dr. Mohsen Shayan, began the PcMOF research that this work builds upon.¹³² Dr. Shayan had the approach of turning the outer benzene rings of the phthalocyanines into benzimidazoles (Figure 3.6), which neatly provided the phthalocyanine with four symmetrical locations that attachment groups could be installed onto. In Dr. Shayan's study, an additional phenylene group was added between the imidazole and a carboxylic acid attachment group. It is worth noting that the synthesis of this pro-linker allows for all the ideal features of a MOF linker described in Chapter 1. As

illustrated below in Section 3.2.1 (Figure 3.8), as long as a substituted benzaldehyde can be acquired, wherein the substitutions contain the attachment groups, a phthalocyanine can be made that has the potential to act as a good linker for MOF synthesis.

3.1.4 Motivation of this work

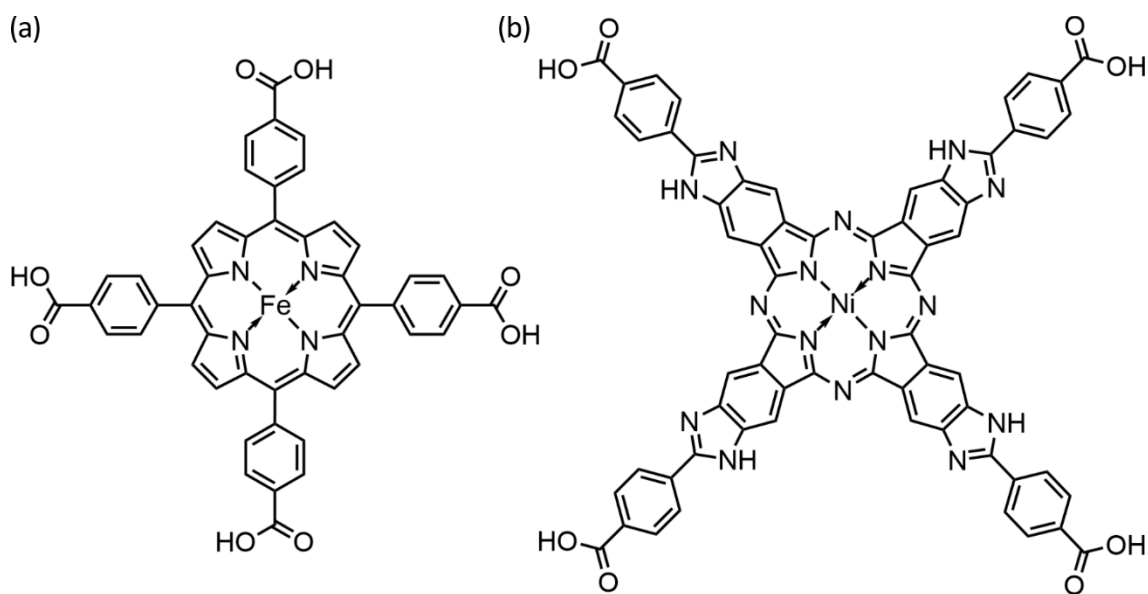


Figure 3.7 (a) The porphyrinic linker used in PCN-222, (b) The phthalocyanine linker synthesized by Dr. Shayan.

During his research, Dr. Shayan was able to synthesize this linker, henceforth called BzPcLinker, with Ni and Co in the core of the phthalocyanine. He also successfully incorporated the Ni version of the BzPcLinker (Ni-BzPcLinker) into a MOF by using the synthesis of the MOF known as PCN-222²⁹ as a template, given the similar shape/size of PCN-222's linker to the BzPcLinker (Figure 3.7). As he was focused on trying to identify parameters that would allow the linker to be incorporated into a MOF of any porosity, Dr. Shayan explored the wide reaction space in search of a set of parameters that would

produce a material that was slightly porous. Then, he experimented with those conditions further. This approach was successful, and Dr. Shayan was able to identify a synthetic space that created a porous material, henceforth called BzPcMOF, with a maximum achieved BET-SA of 1220 m²/g. This was not a surface area that could be reached on a consistent basis, yet, and there were parameters that remained unexplored due to the unavoidable constraints of a finite program and finite research time in an infinite synthetic parameter space.

One indicator of an effective MOF synthesis is its replicability (i.e., its ability to produce surfaces areas in agreement with one another between repeated syntheses). When I picked up this project, the standard synthesis of BzPcMOF was still newly discovered, and lacked the desired level of replicability when experimenting with the incorporation of a new ligand family into MOFs.

Since the upper limit of BzPcMOF's surface area was unknown, the principal goal of this chapter was thus to refine the synthesis enough so that surface areas > 600 m²/g could be consistently achieved. I also sought to produce a sample of this MOF that would allow for the determination of its crystal structure, either by PXRD or single-crystal X-ray diffraction. Understanding the structure of the MOF would provide a great deal of insight into how the synthesis can be improved (e.g., it could help inform stoichiometric ratios, etc.).

3.2 Results and Discussion

3.2.1 Linker synthesis

In order to synthesize the MOF and experiment with its surface area, the linker needed to first be synthesized. Dr. Shayan's previous research on BzPcMOF suggested that synthesized samples of the MOF contained unknown material in their pores; the most probable source of this material was judged to be unreacted reagents or by-products trapped in the pores in samples of the synthesized BzPcMOF. As such, it was prudent to reexamine the linker synthesis as familiarity with it was being built to see whether there were any opportunities to refine the synthesis and obtain a purer product.

The synthesis of the BzPcLinker as outlined by Dr. Shayan can be seen in Figure 3.8. The process involves the synthesis of a bisulfite adduct from a substituted benzaldehyde, followed by the conversion of that adduct into a benzimidazole through the reaction of it with 4,5-diaminophthalonitrile. Finally, the tetramerization of the benzimidazole forms the phthalocyanine, which can be readily deprotected to generate the pro-linker.

In the interest of attempting to reduce amount of unwanted material (i.e., unreacted reagents, side products, impurities) in samples of synthesized BzPcLinker, two key changes to Dr. Shayan's original BzPcLinker prep were made following experimentation with the synthesis.

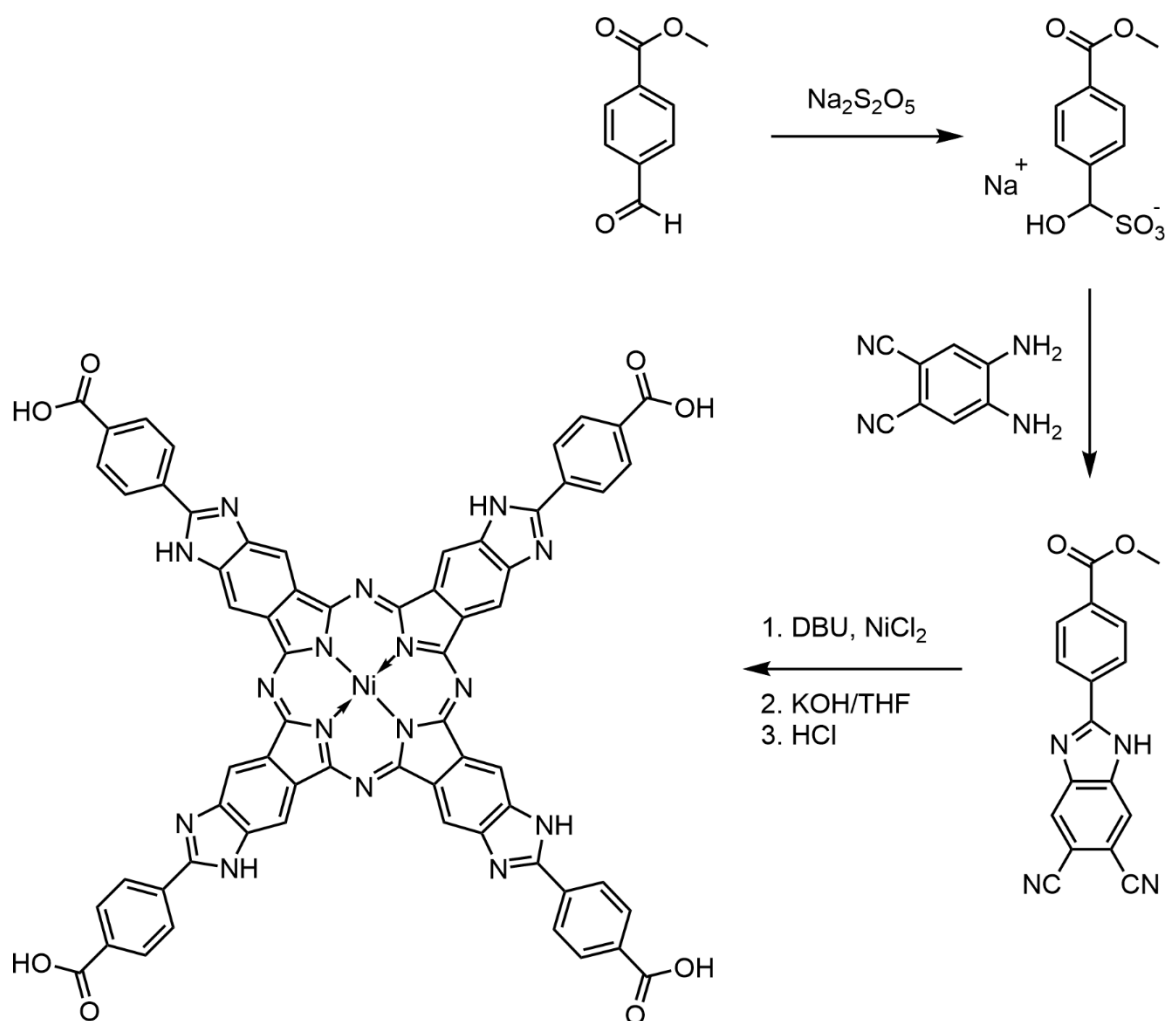


Figure 3.8 Synthesis roadmap of the Ni-BzPcLinker. Full experimental can be found in Section 3.4.

First, the quantity of NiCl_2 used was reduced from the original 179 mg to 110 mg to more closely reflect the 4:1 stoichiometric ratio of BZI tetramers to Ni atoms. In the original procedure with an excess of Ni, it was noticed during the washing steps that a large amount of dark material was present floating on top of the solution, and which would not settle by centrifuge. When the synthesis was modified, the solution contained much less of this difficult-to-remove byproduct, without notable changes to the final yield, suggesting the removal of impurities. Second, the quantity of 1,8-diazabicyclo(5.4.0)undec-7-ene (DBU)

used was reduced from 1.225 mL to 1.000 mL after several experiments with varying levels of DBU. During any synthesis of the BzPcLinker, the final washes for synthesized samples produce a clear dark brown solution; it took longer to remove this dark brown colour from samples of BzPcLinker when it was synthesized with more DBU. Given that the increased presence of this dark material is associated with higher quantities of base used in the synthesis, and this dark material is significantly more soluble than the BzPcLinker, it is suspected that this dark material is the product formed when the BZI polymerizes instead of tetramerizes. When the amount of DBU was reduced, the BzPcLinker produced clearer LDI mass spectra, and the yield improved slightly from 13% to 18%.

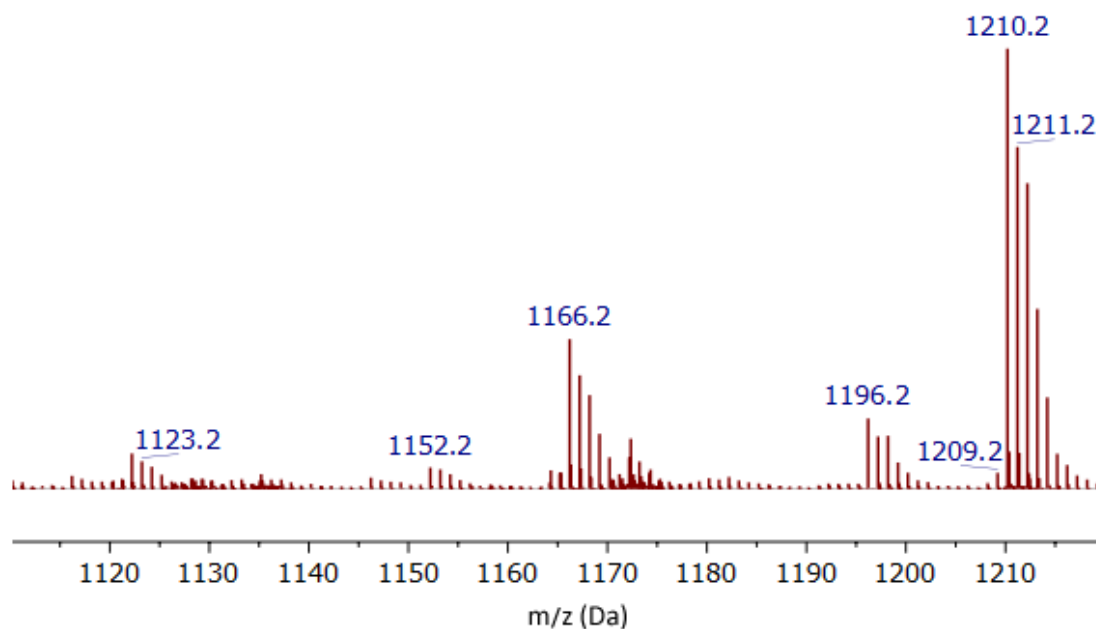


Figure 3.9 LDI mass spectrum of Ni-BzPcMOF. The molecular ion signal appears at $m/z = 1210.2$.

Due to the BzPcLinker's low solubility, its tendency to aggregate, and the potential for the Ni(II) in its centre to be paramagnetic, broadening of any $^1\text{H-NMR}$ peaks was expected. As such, $^1\text{H-NMR}$ was not attempted for the characterization of the linker. In lieu of other analytical methods, laser desorption/ionization mass spectrometry (LDI-MS) was used to confirm the synthesis of the linker (Figure 3.9).

3.2.2 Original Ni-BzPcMOF synthesis

When this project was picked up, the standard synthesis of the Ni-BzPcMOF was as follows: To a 50 mL Duran vial, 70.0 mg ZrCl_4 (0.300 mmol) and 1.800 g benzoic acid (14.74 mmol) were added, along with 24.0 mL of DMF. The cap was screwed on, and the mixture was sonicated for 10 min to give a colourless solution. The vessel was placed in the oven at 80 °C for 1 h before being removed from the oven and allowed to cool to room temperature; this is reminiscent of the pre-conditioning work demonstrated in Chapter 2. Then, 35.2 mg of Ni-BzPcLinker (0.0291 mmol) was added to the solution, along with 4 drops of 12 M HCl (ca. 80 μL), and the mixture was sonicated for 60 min to give a clear dark-green solution. Finally, the reaction mixture was placed in the oven at 120 °C for 72 h. When the sample was retrieved, the MOF appeared as a fluffy dark-green solid floating in a clear yellow solution.

After the sample had cooled down, the reaction mixture was transferred to a 50 mL centrifuge tube and subsequently centrifuged at 5500-7500 rpm for 5-15 min after which all of the MOF had settled at the bottom. Then, 15 mL of fresh DMF was added, the sample was shaken, and it was centrifuged again. This process was repeated twice more. After the

DMF was decanted the last time, 15 mL of fresh DMF was again added, and the MOF was left in DMF overnight to ensure all remaining pore-bound impurities had time to leach out of the pores.

The next day, the sample was centrifuged, the DMF decanted, and 15 mL acetone was added. The washing process that had been used for DMF washes was repeated with the acetone. After the last wash, the sample was left in acetone overnight to ensure that all remaining DMF molecules in the pores had ample time to be exchanged for acetone in the pores. Finally, the next morning, the sample was centrifuged again, the acetone was decanted, and the vial containing the wet sample of MOF was placed in the oven at 80 °C overnight to dry. The next day, the sample was collected and transferred to a pre-weighed gas adsorption analysis tube, at which point it was activated with Micromeritics Smart VacPrep by first heating it at 5 °C/min up to a temperature of 90 °C and holding it there for 30 min. Then, the sample tube was heated at 5 °C/min up to a temperature of 120 °C, which was maintained for 10 h. Finally, the sample tube was cooled to room temperature and backfilled with N₂ gas. At this point, the sample was considered ready for any gas adsorption experiments.

3.2.3 Modified BzPcMOF synthesis

As reagents age over time, the surface areas of MOFs synthesized with them may change, ideally for the better but most often for the worst, and the effects of the experimental parameters that are being altered for the research will become obfuscated by the effects of the reagents degrading. Even if one always retrieves fresh reagents for their reactions, there

are other factors that can influence a reaction,¹³³ some of these factors being unknown to the researcher until well after they acquire their control data. This is especially true for the synthesis of new MOFs.

To avoid misinterpreting our results, every time a variable was altered in the experimental MOF synthesis, the standard procedure as outlined by Dr. Shayan was implemented for one sample, and the experimental surface areas were compared in relation to that standard. To this end, results are reported in % change from control instead of as discrete surface areas. This allowed comparisons to be made while ensuring that issues from the age of reagents, quality of solvent, etc. were not interfering with the interpretation of results.

3.2.3.1 Ensuring replicability

Early attempts in this work at making identical samples of BzPcMOF did not meet replicability requirements (Table 3.1); the difference between two surface areas of “identical” samples was far too large to be from stochastic effects alone.

Table 3.1 BET-SA of samples of BzPcMOF made under the same conditions using the “4 drops” method of HCl addition.

	BET-SA (m ² /g)
BzPcMOF-3	1060
BzPcMOF-4	450

Upon examination of the standard procedure, the concentration of HCl was proposed to be the source of the discrepancy. The standard synthesis described the amount of HCl required for the synthesis as “80 μ L/4 drops”. Using an autopipette to dispense exactly 80 μ L of acid would be ideal, however transferring strong acids via autopipette will lead to acidic

fumes entering the body of the autopipette and corroding it, and, depending on the type of material used for the disposable autopipette tips, plastics may leach from the tip into the acid, leading to the presence of nano/microplastics in the reaction mixture. In the standard synthesis, to avoid these risks, 4 drops of HCl were added with a Pasteur pipette.

However, “4 drops” is not a replicable quantity, since such drops could all be different sizes from one another; it could not be guaranteed that the amount of HCl being added was consistent between samples. Since it could be the case that the MOF was highly sensitive to the concentration of HCl, a different approach to adding acid was developed.

The new procedure for addition of HCl was thus: To add 80 μL of HCl to each of the 3 samples being prepared, 1 mL of HCl was added to 5 mL of DMF, and 480 μL of the resulting solution was transferred via autopipette into each sample. This new approach shares some of the possible pitfalls mentioned previously (i.e., potential leaching of plastic into solution), but they are ameliorated by the acid no longer being highly concentrated.

Table 3.2 BET-SA of samples of BzPcMOF made under the same conditions using the new method of HCl addition.

	BET-SA (m^2/g)
BzPcMOF-D	654
BzPcMOF-E	626

Once the method of administering HCl was changed, the resulting surface areas were in excellent agreement (Table 3.2). The synthetic procedure was permanently altered to account for this new method of HCl addition.

3.2.3.2 Effects of changes to reagents

Table 3.3 Percent changes to surface area of samples of BzPcMOF under the effects of various changes to the reagents used in the synthesis.

Experiment set	Condition	Change to surface area of resulting MOF
(I)	Increased [HCl] ^[a]	+60%
	Decreased [HCl] ^[b]	+75%
(II)	2x ZrCl ₄	+21%
	3x ZrCl ₄	-4%
	4x ZrCl ₄	-11%
(III)	DMAc as solvent	+4%

^[a] Increased 27%. ^[b] Decreased 27%.

(I) The results of the replicability tests indicated that the MOF was highly sensitive to the amount of HCl used in the synthesis. When samples of BzPcMOF were synthesized with a higher [HCl] and lower [HCl] than the control, it was found that there was a significant increase in the surface area of both of the samples (Table 3.3). It was clear that the procedure should be changed to reflect this new information, but it was unclear whether to permanently increase or decrease [HCl]. Of the two options, the decision was made to use a higher [HCl] in all future syntheses. As discussed in Chapter 1, the increased concentration of acidic modulators in MOF synthesis is associated with the slower formation of MOF in solution,¹³⁴ which in turn is associated with a higher degree of crystallinity. As well, it was observed that, during the cleaning stage of BzPcMOF synthesis, the sample with higher [HCl] had far cleaner washes than the sample with lower [HCl] (i.e., clear and nearly colourless vs. dark green). The colour/clarity of the wash did

not appear to be reflective of the final surface areas, but in the interest of promoting clean and careful MOF formation, the higher acid concentration was chosen, and the standard procedure was changed to use 110 μL HCl (i.e., 660 μL of a 1:5 HCl:DMF solution) instead of 80 μL HCl (480 μL of a 1:5 HCl:DMF solution) for all future experiments. It is indeed strange that samples made with more and less acid produced better surface areas than the standard synthesis sample, and it suggests a more complex underlying relationship between the quantity of acid and the rest of the reaction mixture.

(II) In a typical MOF synthesis, an ideal ratio of metal node precursor (in this case, ZrCl_4) to linker would typically be informed by their stoichiometric relationship in the structure of the MOF. However, as the structure of the MOF was unknown at the time of this research, trial and error was the only realistic option for optimizing the quantity of metal precursor used. In the standard synthesis, 10.3 eq of ZrCl_4 (relative to the amount of BzPcLinker) was the amount used. Experiments were performed with 20.6 eq (2 \times), 30.9 eq (3 \times), and 41.2 eq (4 \times) of ZrCl_4 . 20.6 eq (2 \times) of ZrCl_4 appeared to show an increase to the surface area of the material but amounts of ZrCl_4 exceeding 20.6 eq were found to negatively affect the MOF's surface area (Table 3.3). Though the decline in the 30.9 eq and 41.2 eq samples was not remarkably significant, upon viewing them beneath a microscope, both samples had small cube-shaped crystals mixed in with the MOF powder. When single-crystal X-ray diffraction was performed on these square crystals, they appeared to belong to Zr or a ZrM alloy (presumably $M = \text{Ni}$). It is suspected that excess ZrCl_4 in the reaction mixture reacted with other compounds that were present in order to form these square crystalline impurities. When the 30.9 eq and 41.2 eq samples had their

elemental compositions (i.e., % Zr vs % Ni) evaluated with SEM-EDX (see Section 3.2.4.1), they were found to have elemental compositions similar to the 20.6 eq sample, suggesting that any excess ZrCl_4 after 20.6 eq was not incorporated into the MOF. In the interest of minimizing the presence of unreacted material or Zr-based impurities in the final MOF powder, it was decided that 20.6 eq ZrCl_4 would be the new standard for the synthetic procedure.

(III) The BzPcLinker suffers from poor solubility, which may influence its participation in the synthesis of BzPcMOF. Dimethylacetamide (DMAc) has been in the synthesis of other MOFs with tetratopic ligands, such as NU-1000,¹³⁵ and thus it was chosen as an experimental solvent for BzPcMOF. An experiment was performed where DMF was changed out for DMAc at all points in the synthesis, including changing the DMF wash steps to DMAc wash steps.

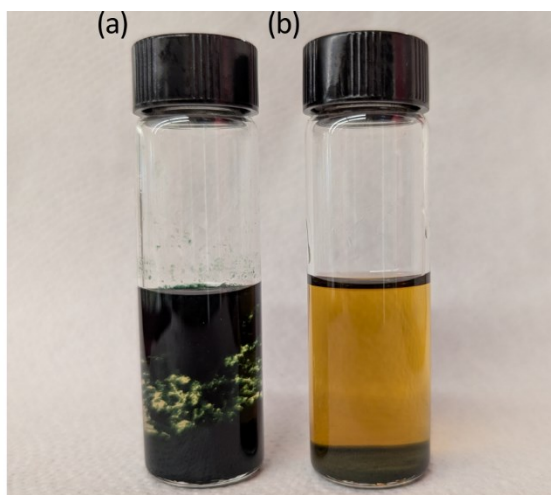


Figure 3.10 Samples of BzPcMOF made in different solvents. (a) Synthesized in DMF, (b) Synthesized in DMAc.

BzPcMOF that has been synthesized in DMF had the appearance of a fluffy green-black solid suspended in solution, while BzPcMOF made with DMAc had the appearance of a grainy black solid settled at the bottom of the reaction vessel (Figure 3.10). Surprisingly, there was effectively no difference in surface area between the sample made in DMF and the sample made in DMAc (Table 3.3). Given the difference in the appearance of the samples made in DMF vs. DMAc (i.e., fluffy and buoyant vs. grainy and sunken), SEM was performed on the samples to assess whether there were small-scale morphological differences contributing to their appearances; these SEMs and further discussion of the difference between the DMF and DMAc samples can be found in Section 3.2.4.2. Since there was no significant difference in the resulting surface areas, it was decided to leave DMF as the principal solvent.

3.2.3.3 Effects of changes to procedure

Table 3.4 Percent changes to surface area of samples of BzPcMOF made with various changes to the synthesis procedure.

Experiment set	Condition	Change to surface area of resulting MOF
(I)	Shortened drying time ^[a]	+30%
(II)	Synthesized at 80 °C	-26%
	Synthesized at 100 °C	-26%
	Synthesized at 140 °C	-27%

^[a] 1 h as opposed to overnight.

(I) In the procedure provided by Dr. Shayan, samples of BzPcMOF were dried in the oven at 80 °C overnight after their final acetone wash. Drying in the oven overnight is conventional for many MOF syntheses, such as that of UiO-66. During experimental

synthesis of BzPcMOF, however, it was noticed that within one h of being placed in the oven, samples appeared to be sufficiently dry such that they could be prepared then for surface area analysis. This led to the question as to whether leaving the sample in the oven for longer than it needed would damage the MOF. 80 °C is a relatively low temperature (given the MOF is synthesized at 120 °C) and phthalocyanines are characteristically stable, so it is not entirely logical that a higher drying temperature would cause a decay in quality. Perhaps, however, drying the MOF while it wasn't under vacuum caused some degree of collapse due to capillary forces in the pores, or being left in the oven overnight with other samples in the oven caused it to take up airborne chemicals. As such, an experiment was performed where a sample of BzPcMOF dried overnight was compared to a sample of BzPcMOF dried for 1 h (Table 3.4). It was found that the 1 h drying procedure produced a better/more porous material. In the interest of shortening the length of the work-up and improving the surface areas, an alteration to the procedure was made to dry the BzPcMOF for 90 min instead over overnight.

(II) Another parameter that had not yet been experimented with was the temperature of the synthesis. The temperature at which a synthesis is conducted often has much to do with the solubility of the reagents and the solubilizing power of the chosen solvent. DMF, known for its exemplary solubilizing power, is employed at many different temperatures across various MOF syntheses, so temperatures above and below the control (120 °C) were assessed for this work.

Changing the temperature in either direction led to a decline in the surface area of the sample (Table 3.4). The surface areas for the experimental samples were not terrible in

isolation, but compared to the surface area for the control, the experimental samples did suffer for the change ($\sim 1000 \text{ m}^2/\text{g}$ for control vs $\sim 800 \text{ m}^2/\text{g}$ for experimental), and as a result, no alterations to the synthesis were made. It is useful, however, to know that the synthesis is indeed still successful at other experimental temperatures. If one were to attempt to synthesize this MOF in a circumstance where they did not have the ability to reach above $100 \text{ }^\circ\text{C}$ (such as in the $^2\text{H-NMR}$ work in Chapter 2), the synthesis would likely still be successful and produce useful results.

3.2.4 MOF characterization

In total, the changes made to the MOF synthesis were as follows: The method of adding HCl was altered, the amount of ZrCl_4 was increased from 10.3 eq (70 mg) to 20.6 eq (140 mg), the amount of HCl added was increased from 80 μL (i.e., 480 μL of a 1:5 HCl:DMF solution) to 110 μL (i.e., 660 μL of a 1:5 HCl:DMF solution), and the oven drying time for the synthesis was decreased from overnight to 90 min. It was also noticed that the surface areas of control samples were higher on average when fresh ZrCl_4 (i.e., removed from the glovebox on the day of synthesis) was used. When these changes are implemented, syntheses of BzPcMOF consistently reach surface areas greater than $1000 \text{ m}^2/\text{g}$, as long as fresh ZrCl_4 is used.

Characterization of the MOF can now proceed with more consistent samples of BzPcMOF. Of principal interest are scanning electron microscopy (SEM) (to assess visual morphology), SEM-EDX (to assess elemental composition), and powder X-ray diffraction (PXRD) (to assess crystallinity).

3.2.4.1 SEM-EDX

One concern regarding this project was that BzPcMOF was not a MOF at all – rather, that it was a hydrogen-bonded organic framework (HOF).¹³⁶ HOFs share some similarities with the class of MOFs, but while MOFs make use of both linkers and nodes, HOFs are made of only linkers. That is, linkers, instead of being bridged by nodes, connect to one another via hydrogen bonds, forming a polymeric complex.

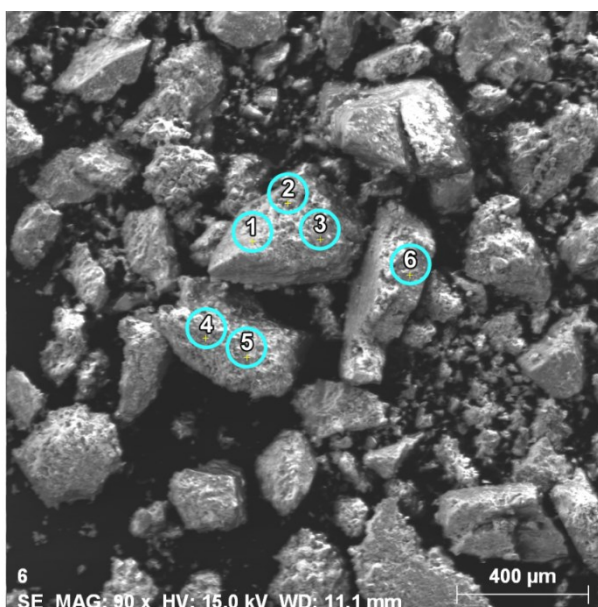


Figure 3.11 The sample of BzPcMOF made with 41.2 eq of $ZrCl_4$, as analyzed with SEM-EDX. The points chosen for multi-point analysis have been circled with blue for visibility.

In the interest of determining whether the BzPcLinker-derived material was a MOF or a HOF, Scanning Electron Microscopy with Energy Dispersive X-ray spectroscopy (SEM-EDX) was employed. SEM-EDX is not capable of probing the structure of the material, but it offers insight into the material's elemental composition. Due to the inherent limitations of EDX, the average percent compositions of any elements lighter than sodium

(e.g., carbon, hydrogen) could not be determined. Performing SEM-EDX allowed the presence of Zr to be evaluated, as well as the ratio of Ni to Zr (if present).

SEM-EDX was performed on four samples of BzPcMOF that were from the experiments varying $[\text{ZrCl}_4]$ (i.e., the “10.3 eq”, “20.6 eq”, “30.9 eq”, and “41.2 eq” samples) – this permitted the observation of how the ratios of the elements in the material were changing in respect to the added ZrCl_4 . In order to minimize the possibility of accidentally targeting one of the Zr-complex crystals that were seen in the 30.6 eq or 41.2 eq samples, multi-point analysis was performed on multiple particles for each sample (Figure 3.11), and the results were averaged.

Table 3.5 Average % compositions of elements in samples of BzPcMOF synthesized with varying amounts of ZrCl_4 .

Amount of ZrCl_4 used	Avg % Cl	Avg % Ni	Avg % Zr
10.3 eq	10.4	13.4	76.2
20.6 eq	9.9	9.8	80.3
30.9 eq	7.1	9.8	83.1
41.2 eq	7.8	9.3	82.3

What was most clear was that Zr was abundantly present in the sample particles (Table 3.5). While it could have been the case that the Zr existed around a HOF material as an impurity after its synthesis, the DMF washes would almost certainly have removed it, so any Zr present could be assumed to be incorporated into the structure of the MOF.

Beyond that, the data elucidate some interesting aspects of the composition of BzPcMOF. As the amount of ZrCl_4 used increases from 10.3 to 20.6 eq and then again to 30.9 eq, the average % composition of Zr increases. At 41.2 eq, the amount of Zr incorporated is

roughly the same as at 30.9 eq, implying that an upper limit of Zr incorporation is reached around 30.9 eq.

This suggests that the original amount of ZrCl_4 used was not ideal, given that adding more ZrCl_4 allowed more Zr to be incorporated into the MOF. It also suggests is that using 20.6 – 30.9 eq of ZrCl_4 is ideal, since adding any more ZrCl_4 past that point no longer has a noticeable effect on the elemental composition of the material or the surface area. This indicates that the excess Zr is not being incorporated. In fact, the appearance of the Zr-complex crystals all but confirms this – excess Zr is indeed being crystallized into some cubic Zr material/alloy.

The sample made with 20.6 eq of ZrCl_4 suggests an approximately 8:1 ratio of Zr atoms to Ni atoms (Table 3.5). If it is assumed that the $\text{Zr}_6\text{O}_4(\text{OH})_4^{12+}$ node is present in the MOF, then the ratio can be seen instead as 1.3:1 ratio of Zr_6 nodes to Ni atoms.

It is worth noting that these ratios are in regard to a single formula unit of this MOF. For example, UiO-66 has 12 linkers coordinated to each node. However, since each of those linkers is connected to another node, the ratio of nodes to linkers in UiO-66 is understood as 1:6. In the case of BzPcMOF, each linker connects four separate nodes, so a 1.3:1 ratio of nodes to linkers would actually suggest that each node has approximately 4 linkers attached to it.

This 1.3:1 ratio can be rationalized if one first assumes that the $\text{Zr}_6\text{O}_4(\text{OH})_4$ cluster is present in a capped state. That is, if one assumes that there is an extra $\text{OH}/\text{H}_2\text{O}$, or equivalently a benzoate/formate, per Zr atom, the cluster will have a charge of 6^+ instead

of 12^+ . Then, if the linker in the MOF has a charge of 8^- (i.e., all the carboxylic acids are deprotonated, as well as each imidazole), then these two components can be balanced if there are 4 $Zr_6O_4(OH)_4$ clusters (total charge of 24^+) for every 3 linkers (total charge of 24^-). This 4:3 ratio of $Zr_6O_4(OH)_4$ to linker (in terms of the formula unit) can thus be reduced to 1.3:1, which would match the ratio observed by SEM-EDX.

What was also notable from the EDX data was the presence of Cl in the MOF. Since the MOF is synthesized with HCl and $ZrCl_4$, they are the likely sources of Cl atoms. These Cl atoms could be capping a Zr node, charge balancing a defect, or coordinating to the Ni atoms in the BzPcLinkers.

3.2.4.2 SEM visual assessment

Given that the sample of BzPcMOF synthesized in DMAc had a significantly different appearance than samples synthesized in DMF, SEM was performed on a sample of BzPcMOF made in DMF and a sample of BzPcMOF made in DMAc.

The SEM images showed a significant difference in the average size of particles of BzPcMOF made in DMF versus those made in DMAc (Figure 3.12). Samples of BzPcMOF made in DMF showed a variety of particle sizes, with larger particles that appeared to be aggregates of smaller particles. The DMAc sample, in contrast, had much smaller particles on average, with very few aggregate particles (Figure 3.13). Sadly, neither of these SEMs exhibit morphologies that are consistent with single isolated crystals of MOF.

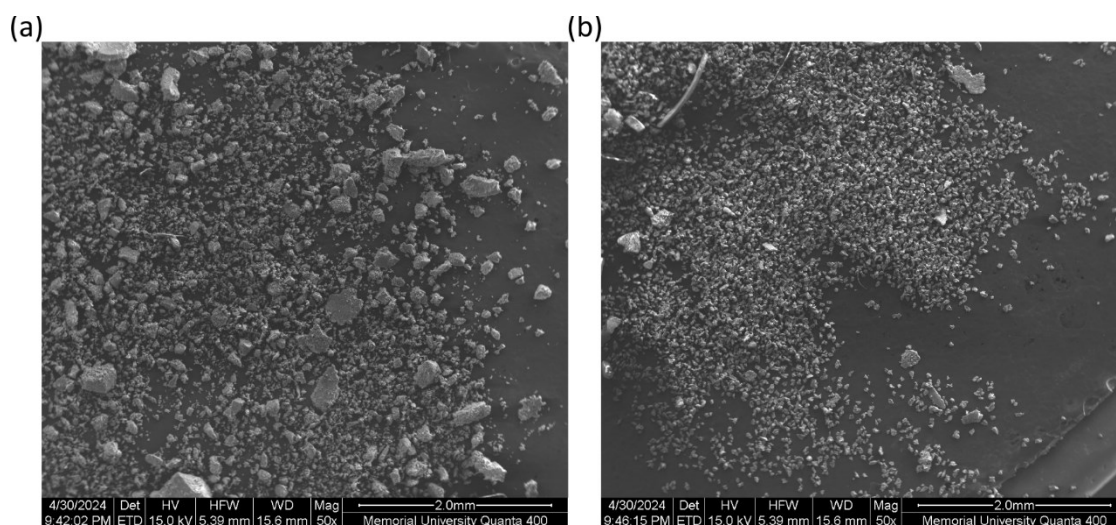


Figure 3.12 SEM images of BzPcMOF synthesized in different solvents viewed at 50 \times magnification. (a) BzPcMOF synthesized in DMF, (b) BzPcMOF synthesized in DMAc.

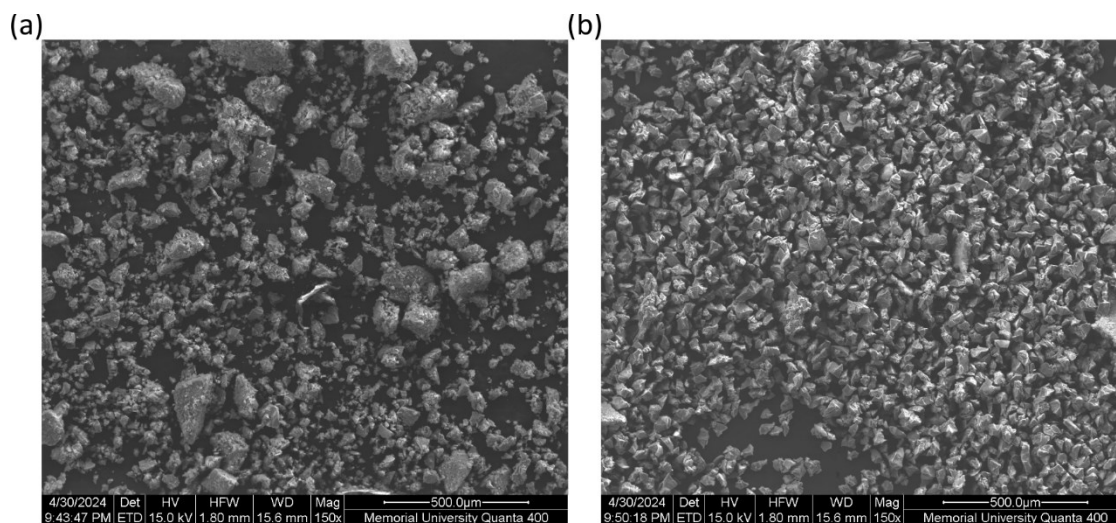


Figure 3.13 SEM images of BzPcMOF synthesized in different solvents viewed at 150 \times magnification. (a) BzPcMOF synthesized in DMF, (b) BzPcMOF synthesized in DMAc.

The synthesis of BzPcMOF, in the case of both DMF and DMAc, included the use of 12 M HCl. Data obtained during the work in Chapter 2 suggested that DMF hydrolysis was occurring in the presence of HCl during the synthesis of UiO-66-HCl at 80 $^{\circ}$ C. Given that the synthesis of BzPcMOF includes HCl and takes place at 120 $^{\circ}$ C, one can assume that

DMF hydrolysis is occurring in situ, producing formic acid and dimethylamine. Similarly, DMAc may hydrolyze during the synthesis in DMAc, producing acetic acid and dimethylamine (Figure 3.14).

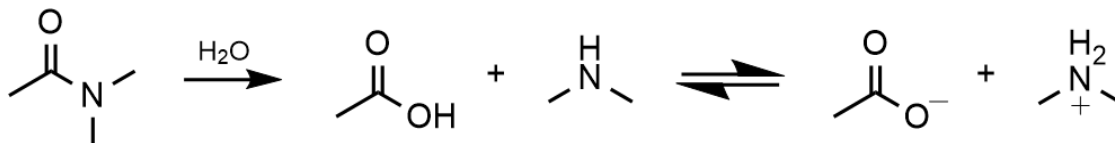


Figure 3.14 Hydrolysis of DMAc into acetic acid and dimethyl amine, which are in equilibrium with acetate and dimethylammonium.

It is likely that resulting differences in the appearance of the MOF are attributable to this difference in modulation, which may reflect a difference in hydrolysis rates of DMF and DMAc under otherwise equivalent conditions. As was also seen in Chapter 2, the choice of modulator in a synthesis can have a significant impact on the resulting MOF (visual morphology, defectivity, etc.). In those experiments, particles of UiO-66-AA appeared as octahedrons, whereas particles of UiO-66-BA and UiO-66-HCl had an irregular/lumpy appearance. It is possible that the presence of acetic acid instead of formic acid in the synthesis of BzPcMOF led to the visual difference seen here.

3.2.4.3 PXRD

XRD was initially measured on a Rigaku Ultima IV X-ray diffractometer located in TERRA in the CREAT network at MUN. The resulting diffractograms contained very few and broad peaks, which is typical of large-pore MOFs. Due to the low number of observed reflections, determining structural information from the diffractogram was not possible. Given the low angle limitation of the instrument (3.61° in 2θ) and the knowledge that that

MOFs with similarly sized porphyrinic linkers can have peaks below this cutoff, samples were sent to McMaster University to obtain data below 3.61° in 2θ . In hindsight and in talking with Rigaku, we learned that our instrumentation could also have reached these low angles. The observed diffractogram from McMaster University is shown in Figure 3.15 with four observed reflections.

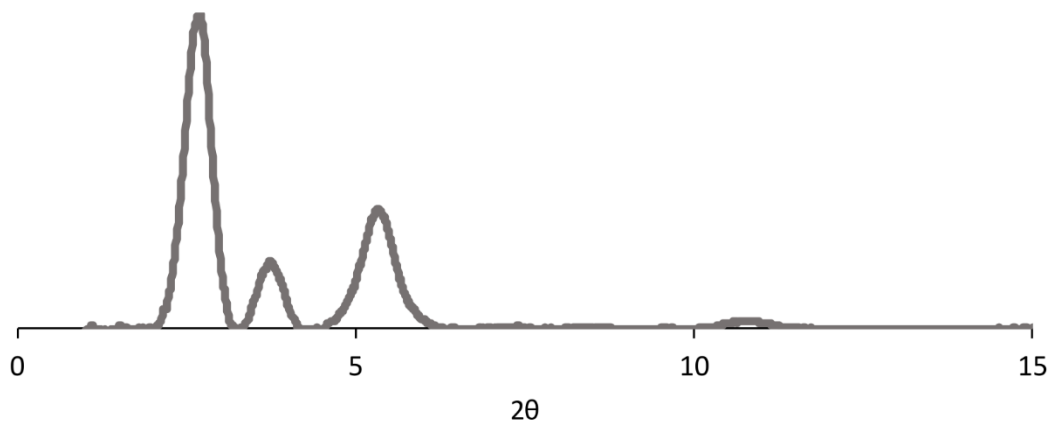


Figure 3.15 Powder X-ray diffractogram of BzPcMOF.

The diffractogram provided a clearer look at four reflections, but did not provide enough information for the crystal structure to be determined. Without a straightforward path to solving the crystal structure, a slightly unorthodox approach was employed.

Crystal structures saved in the crystallographic information file (.cif) format can be used by programs like Mercury to simulate the X-ray diffractogram of that structure. For experimental samples of MOFs that may host guest molecules in their pores, the relative intensities of the simulated diffractogram will vary slightly-to-moderately relative to experimental samples, but there is typically a high degree of agreement between the peak locations of the simulated and experimental diffractograms. While this fingerprinting

technique is often employed to confirm the identity of a MOF (as seen in Chapter 2), it can also be used for exploratory purposes.

The attachment points on the BzPcLinker make it a tetratopic square planar linker, which is similar in structure to existing tetratopic square planar porphyrin linkers (Figure 3.7) found in many MOFs. Thus, a list of MOF topologies that use square planar ligands was obtained via the literature and a search of the Cambridge structural database. Using these known structures, the Topologically Based Crystal Constructor (ToBaCCo)¹³⁷ was used to generate the crystal structures of MOFs that could conceivably host the BzPcLinker. This was done by first preparing two simulated .cifs for the BzPcLinker and the node found in the existing porphyrin MOFs. It is worth noting that while only the $Zr_6O_4(OH)_4$ node was used, each node was slightly distorted from the ideal Zr_6 octahedron geometry. Then, from each of these unique topologies, a topology .cif was generated. Within a topology .cif, the MOF's topology was simplified to a coordinate for the centre of mass of the linker and a coordinate for the centre of mass of the node. As well, a series of "bonds" were included to describe how these centers of mass connect to one another. One at a time, ToBaCCo used each of these unique topology .cifs, alongside the .cifs of the linker and node, and attempted to fit the linkers and nodes to that topology. When successful, ToBaCCo returned a .cif of the provided linkers and nodes arranged in that topology, and this .cif was then used to simulate the X-ray diffractogram of the resulting MOF.

This process was performed with 5 of the unique topologies that could conceivably host the BzPcLinker. Given that ToBaCCo necessitates isolated nodes and not chain-based

nodes, some topologies could not be examined. Once all of the simulated diffractograms were obtained, they were compared against the experimental diffractogram (Figure 3.16).

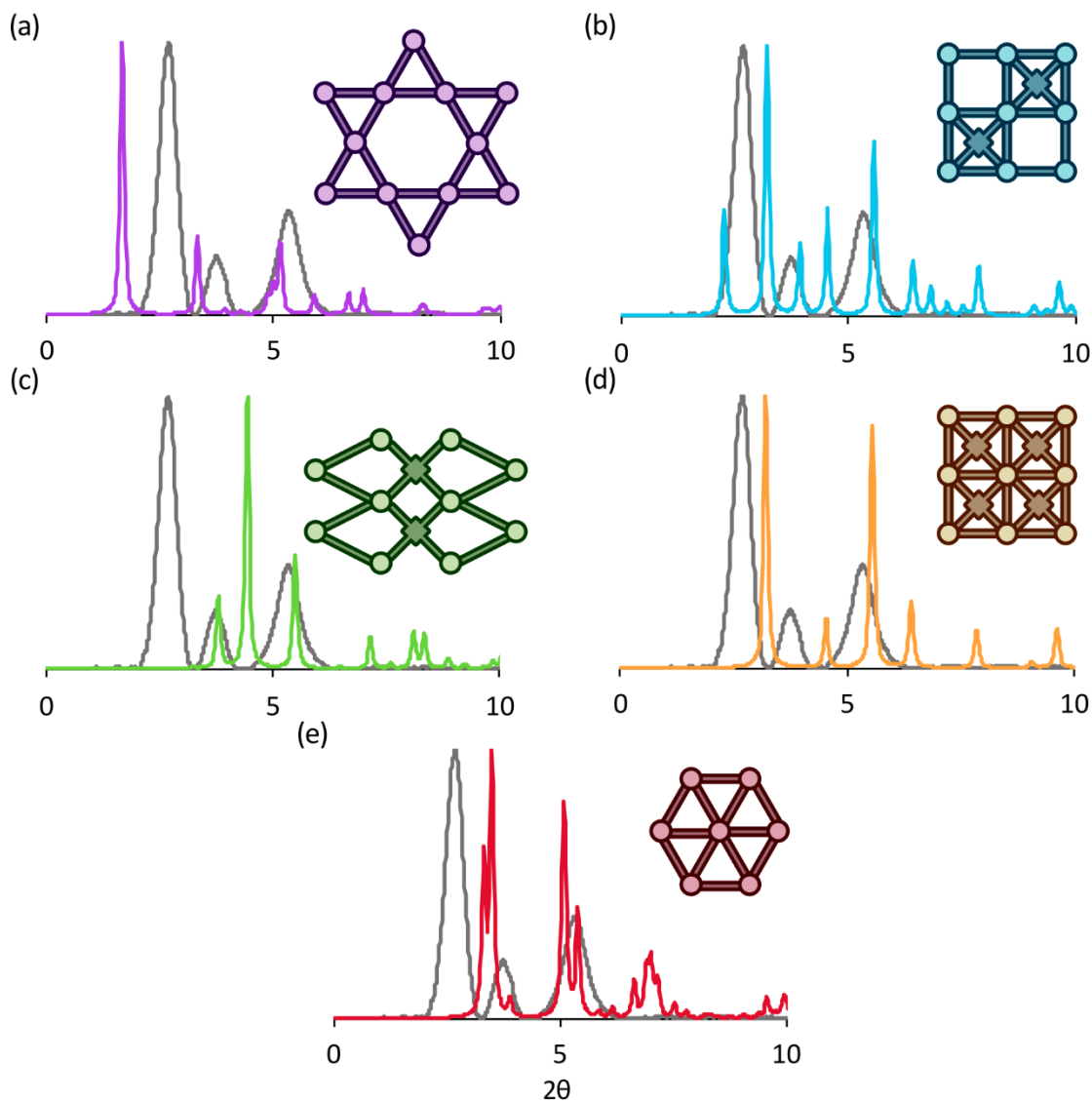


Figure 3.16 Experimental PXRDs of BzPcMOF (grey) compared against simulated diffractograms of MOF topologies containing the BzPcLinker. (a) *csq*, (b) *she*, (c) *sqc*, (d) *ftw*, (e) *shp*.

Of the topologies explored, *csq* (Figure 3.16 (a)) and *ftw* (Figure 3.16 (d)) had the closest agreement with the experimental diffractogram. The *shp* topology, which is related to the

csq topology, is also possible; the *csq* topology can be seen as ordered defects of the *shp* topology. Thus, it is possible that a *csq/shp* “mix” topology is also possible, but no attempts were made at this time to model it.

None of the simulated diffractograms from these topologies aligned perfectly with the experimental, but *csq* and *ftw* both featured the three large early peaks with spacings that were similar to the experimental diffractogram. Though there is not perfect agreement, one of these two could still be the true topology. Since the unit cells for these topologies are only simulations, their exact measurements may be inaccurate, even if they reflect the true topology.

One possible reason for any inaccuracies is due to the fact that the simulation is not able to account for the general movement of a framework in a MOF, so the effect of movement that is transverse to a bond is not considered. In experimental structures, transverse movement across a bond leads to the bond’s average length being shorter than it would be without transverse movement (i.e., in simulations). Thus, the “longer” bonds in simulated structures may lead to larger unit cells, which would cause peaks on simulated diffractograms to appear at a lower angle than what is seen experimentally. If this were the case here, this would favour the *csq* topology (Figure 3.16 (a)), but the obtained surface areas for BzPcMOF are low compared to other *csq* MOFs, such as PCN-222 (e.g., 1200 m²/g for BzPcMOF vs. 2300 m²/g for PCN-222).²⁹ This suggests that either there is material stuck in BzPcMOF’s pores that is lowering the surface area, or the *csq* topology is incorrect.

The SEM-EDX data from Section 3.2.4.1 suggested that each node was connected to approximately 4 linkers. Of the topologies examined, none of them involved 4-connected nodes – they were all either 6-connected (*she*), 8-connected (*csq*, *sqc*), or 12-connected (*ftw*, *shp*).

It is also worth noting that the *ftw* topology was only simulated with the $Zr_6O_4(OH)_4$ node. The *ftw* topology is also seen in MOFs which contain what is called the Zr_8O_6 node. Recent literature suggests that the Zr_8O_6 node is actually composed of four $Zr_6O_4(OH)_4$ nodes in distinct orientations within the unit cell, as in the case of PCN-221.¹³⁸ If this node were present in BzPcMOF under the *ftw* topology, it could make the unit cell appear larger than expected, which would account for the differences in the PXRD. This node would contain 24 Zr atoms, which, together with the SEM-EDX data, would suggest a 1:3 ratio of nodes to linkers. This is consistent with the ratio of nodes to linkers for a structure with a 12-connected node, such as the node seen in *ftw* topologies.

3.2.5 MOF stability

One of the most desired features among MOFs is stability.^{26,27,139} For a MOF to reach the point of being synthesized and utilized in industry, it must at least be worth its cost in reagents. That is, the MOF should be stable enough to perform its designated task multiple times. If a MOF is intended to be used long-term, it requires temporal stability; if a MOF is intended to be used in flue gas separation, it needs to be stable to compounds found in flue gases (e.g., SO_x and NO_x); if a MOF is intended for photocatalytic water splitting, it requires stability in water; if a MOF is intended to be used in a high-temperature

environment, it needs thermal stability. Producing a MOF that is stable under a wide variety of conditions like this is challenging. Assessing the limits of new MOFs helps determine the ideal applications for them.

3.2.5.1 Temporal stability

An important feature for any MOF is its ability to maintain its structural integrity over time. To assess the temporal stability of BzPcMOF, an old sample of BzPcMOF, which had been stored for 6 months on the bench in a 1 dram vial after previous surface area analysis, was re-activated and its surface area was re-collected and compared to its original surface area.

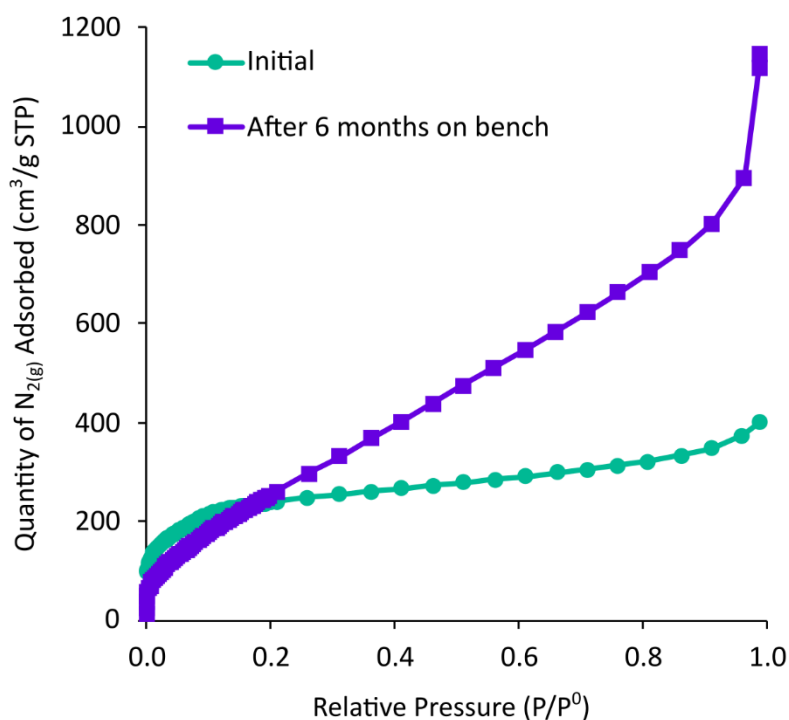


Figure 3.17 Nitrogen gas adsorption isotherms, measured at 77 K of a sample of BzPcMOF before and after it sat on the lab bench in a sealed vial for 6 months.

Until the collection of the aged isotherm, BzPcMOF had only been seen to produce a Type I isotherm. The sample of aged BzPcMOF, however, produced a Type II isotherm (Figure 3.17), which suggests that, during the 6 months it was sitting on the bench, its external surface area increased significantly.

Table 3.6 Surface areas of a sample of BzPcMOF before and after it sat on the lab bench in a sealed vial for 6 months.

	BET-SA (m ² /g)	Change from control
Initial	960	/
After 6 months elapsed	1099	+14%

Interestingly, the surface area of the sample did not suffer for the change (Table 3.6), and in fact increased by 14%. This suggests that whatever is causing the change in the isotherm shape is not compromising the internal surface area of the material. The pore size distributions, as discussed in Chapter 1, are calculated from the isotherms, so an entirely different isotherm shape means there will likely be an entirely different pore size distribution.

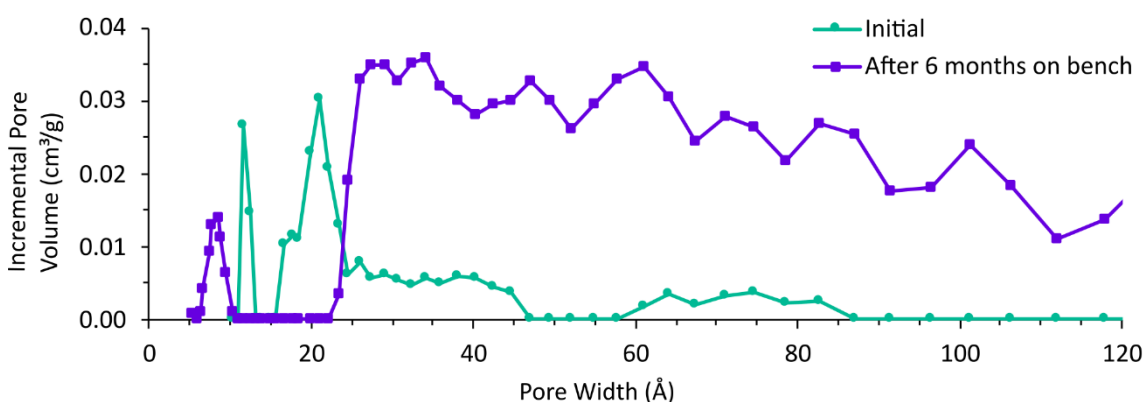


Figure 3.18 PSDs of a sample of BzPcMOF before and after it sat on the lab bench in a sealed vial for 6 months. PSDs were calculated using the Tarazona model.

Indeed, the pore size distribution for the aged sample was markedly different (Figure 3.18) compared to the initial sample. The pores between 10-25 Å were gone, instead replaced with one single pore at ca. 8 Å and then what appeared to be a large array of mesopores exceeding 25 Å. These large pores are not true pores, they are a direct result of the mathematical model attempting to accommodate for the shape of the isotherm. The question remains as to how and why the MOF's external surface area increases over time.

3.2.5.2 Water stability

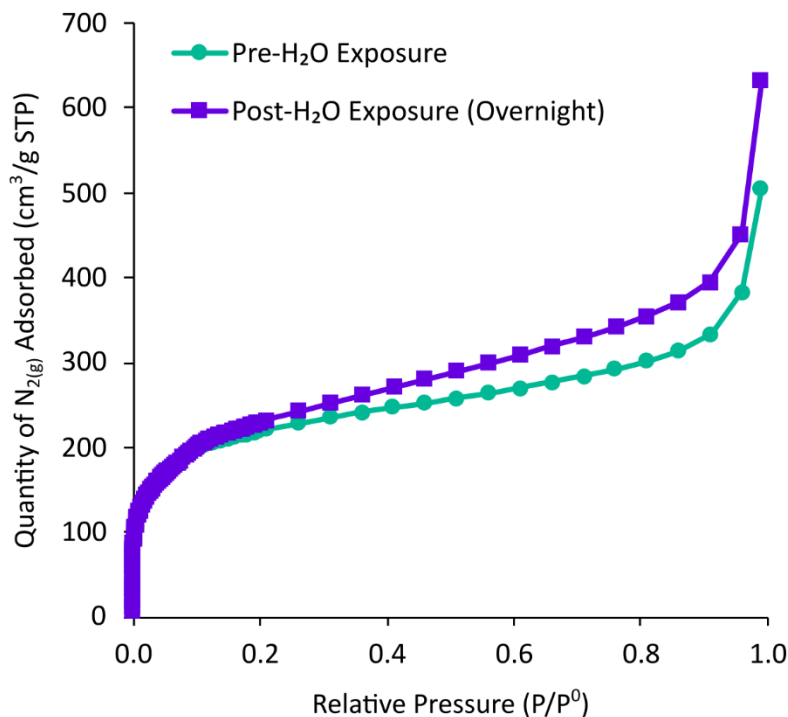


Figure 3.19 Nitrogen gas adsorption isotherms measured at 77 K for samples of freshly made BzPcMOF before and after being submerged in distilled water overnight.

Whether a MOF remains stable in the presence of water is a significant contributor to the potential real-world applications of the material. MOFs lend themselves well to adsorption and separation-based applications, but water is ubiquitous in many such cases. MOFs have

been suggested for applications involving separation of flue gases and natural gases, both of which tend to contain water in their compositions. Moreover, any application involving the MOF being exposed to humid air must also necessitate water stability.

In order to assess the water stability²⁷ of BzPcMOF, a fresh sample of BzPcMOF was placed in a centrifuge tube, and the tube was filled with distilled water. The sample was left to soak overnight, and the next day, the water was exchanged for acetone, the MOF was allowed to dry in the oven, and the material was re-activated.

Table 3.7 Surface areas of a sample of fresh BzPcMOF before and after it was submerged in distilled water overnight.

	BET-SA (m ² /g)	Change from control
Initial	872	/
Post-H ₂ O submersion (Overnight)	908	+4%

There was no significant change to the isotherm after overnight submersion in water (Figure 3.19). There was slight deviation away from the Type I isotherm shape to a more Type II shape, but the surface area of the material did not suffer from the difference (Table 3.7).

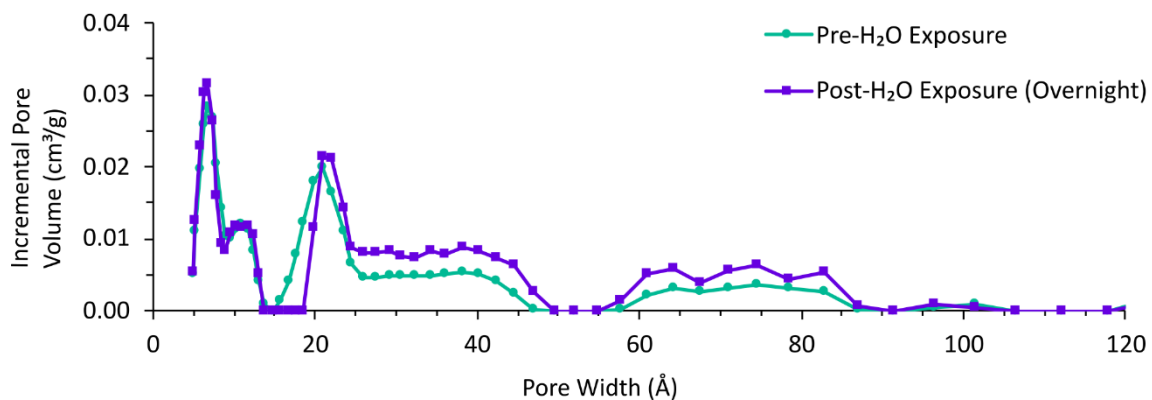


Figure 3.20 PSDs of a sample of BzPcMOF before and after it was exposed to distilled H₂O overnight. PSDs were calculated using the Tarazona Model.

The pore size distributions for the BzPcMOF pre- and post-H₂O exposure share many features (Figure 3.20), suggesting the pores largely retained their integrity. The pores at ~ 8 Å, ~ 12 Å, and ~ 22 Å are present in both samples. The mesoporous region of the PSD (20 – 120 Å) appears to demonstrate an increase in the incremental pore volume of some of the mesopores in the sample post-exposure; the appearance of these mesopores is likely due to external surface area or cavities formed from packed microcrystalline powder and not the pores in the MOF.

It is apparent from these data that overnight submersion in H₂O does not have an immediate negative effect on the MOF. To further assess the limits of its stability in water, a sample of old MOF that had been sitting on the bench for several months was re-activated, had adsorption analysis performed on it, and then was submerged in deionized water for one week.

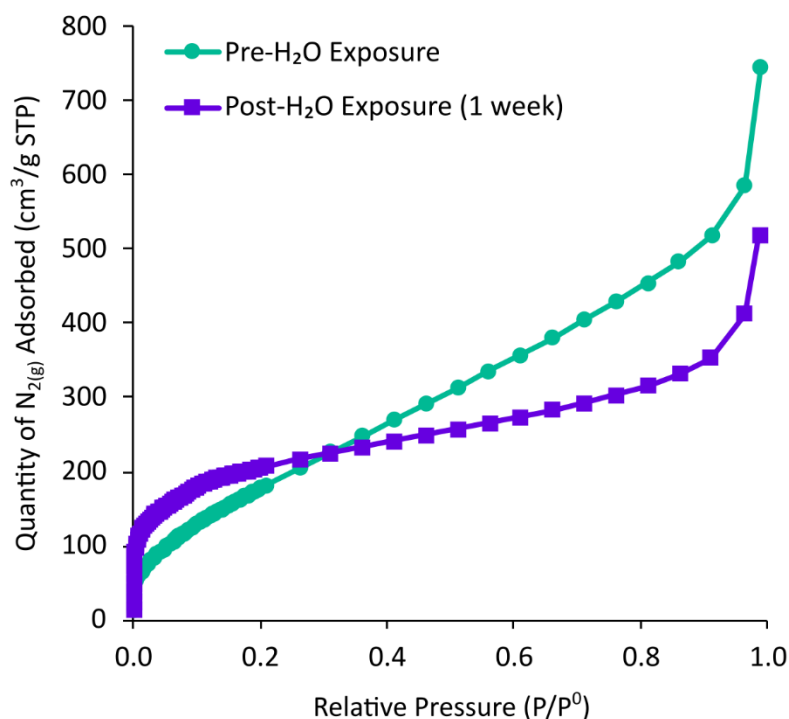


Figure 3.21 Nitrogen gas adsorption isotherms measured at 77 K for a sample of aged BzPcMOF before and after being submerged in distilled water for 1 week.

It is worth noting that the isotherm of the MOF before it was exposed to H₂O (Figure 3.21) is consistent with the appearance of the aged isotherms acquired during the temporal stability tests (Figure 3.17). That is, the MOF that was chosen as the initial for this water stability test was MOF that had already changed to increase its amount of external surface area.

Table 3.8 Surface areas of a sample of old BzPcMOF before and after it was submerged in distilled water for 1 week.

	BET-SA (m ² /g)	Change from control
Initial	770	/
Post-H ₂ O submersion (1 week)	800	+4%

Interestingly, there was a significant change in the shape of the isotherm of the water-exposed MOF compared to its initial shape (Figure 3.21). The Type II isotherm characteristic of aged BzPcMOF changed to an isotherm that was more consistent with a Type I shape. Based on evidence thus far, this suggested that H₂O exposure reduced the external surface area of the material. Again, the experiment did not appear to negatively affect the total surface area of the MOF (Table 3.8).

Like the isotherm, the initial PSD of the MOF (Figure 3.22, green circles) is reflective of the MOF being an aged sample, displaying one pore at 8 Å, and an array of ‘mesopores’. The PSD of the sample after it was exposed to H₂O for one week (Figure 3.22, blue squares) is shockingly consistent with that of fresh BzPcMOF. The pores at 8, 12, and 22 Å are once again present, and the proportion of volume made up of these ‘mesopores’ is decreased.

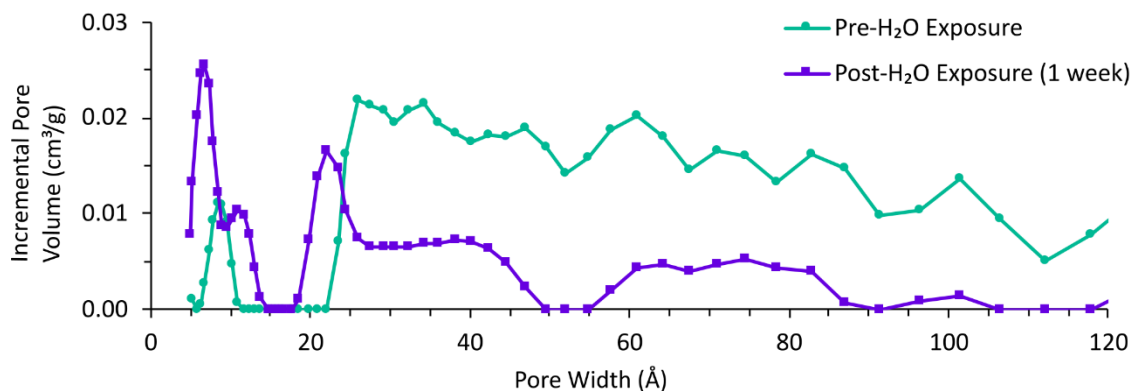


Figure 3.22 PSDs of a sample of aged BzPcMOF before and after it was exposed to distilled H₂O for a week. PSDs were calculated using the Tarazona model.

Earlier, it had been noted that the reason BzPcMOF’s external surface area increased when it was left on the bench. These data suggest that whatever process is causing the external surface area of the MOF to increase over time when it is left out on the bench appears to be effectively reversed by aqueous submersion.

3.2.5.3 SEM of water stability test samples

Given that the isotherms and PSDs of the samples of BzPcMOF from the water tests appeared to demonstrate an increase in the external surface area of the MOF, it is reasonable to suspect some type of morphological change may occur as a result of prolonged submersion in water. To this end, SEM was performed on samples of aged BzPcMOF before and after submersion in water for a week.

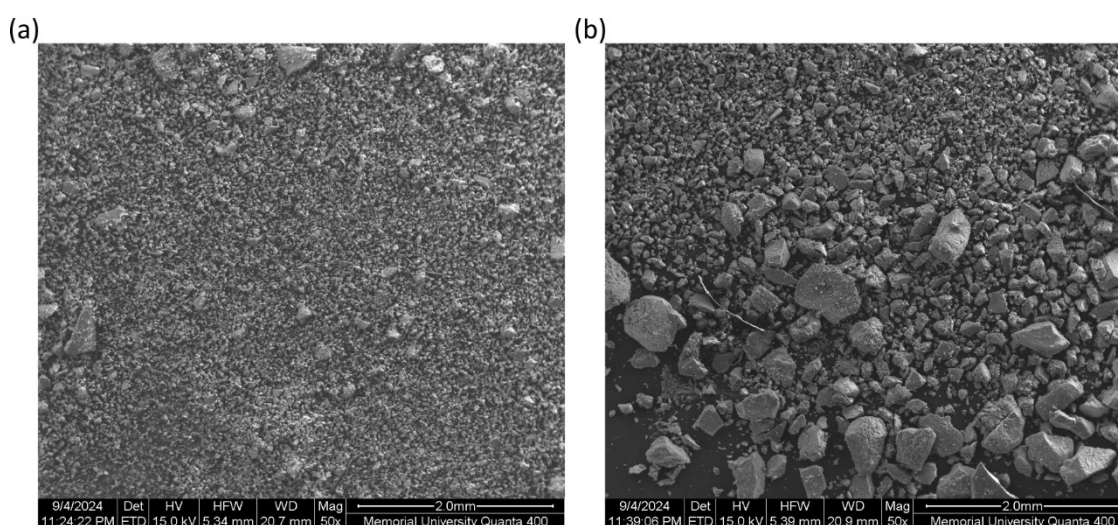


Figure 3.23 SEM images taken at 50 \times magnification of a 6 month old sample of BzPcMOF before and after it was submerged in water for a week. (a) Before submersion, (b) After submersion.

There was a significant difference in the appearance of the sample once it had been submerged in water for a week. Prior to submersion, the sample appeared as very fine particles of somewhat regular size (Figure 3.23 (a)). After submersion, however, the particles appeared to be larger and of more irregular size (Figure 3.23 (b)).

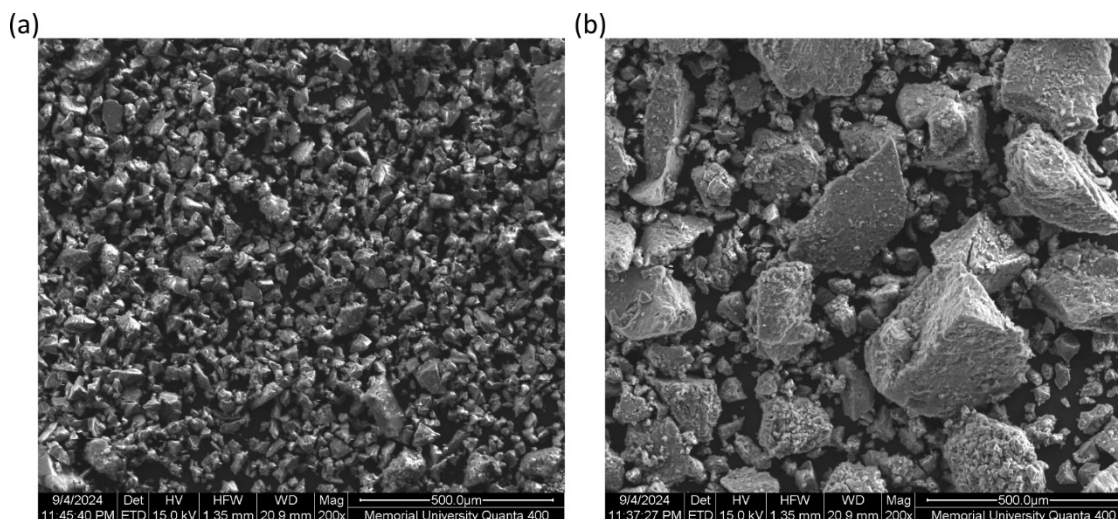


Figure 3.24 SEMs at 200 \times magnification of a 6 month old sample of BzPcMOF before and after it was submerged in water for a week. (a) Before submersion, (b) After submersion.

Upon closer inspection at a higher magnification, the starkness of the difference was made plain. Many of the larger particles that were present in the post-submersion sample (Figure 3.24 (b)) appeared to be aggregates of the smaller particles that made up the pre-submersion sample (Figure 3.24 (a)). That is, it appears that the process of submerging the MOF in water causes the small particles of MOF to aggregate into larger particles.

The trend seen with particle sizes of these samples of BzPcMOF is consistent with the trend observed through the water stability isotherms. The isotherms and PSDs suggested that an aged sample of BzPcMOF, which had a high external surface area, could have its external surface area reduced by soaking it in water. This aligns with the observations here that samples soaked in water have a higher average particle size (and thus a lower external surface area).

In summary, the stability experiments demonstrated intriguing behaviours from the BzPcMOF. Fresh samples of BzPcMOF have low external surface areas and large average

particle sizes (Figure 3.25 (a)). As fresh samples of BzPcMOF are left under ambient conditions over time, the large particles, which are made of many small particles aggregated together, begin to separate into their constituent pieces (Figure 3.25 (b)). This means that, over time, the average particle size in a sample of BzPcMOF will decrease. When a sample is submerged in water, however, the small particles re-aggregate and form large particles that appear similar to fresh samples of BzPcMOF (Figure 3.25 (c)).

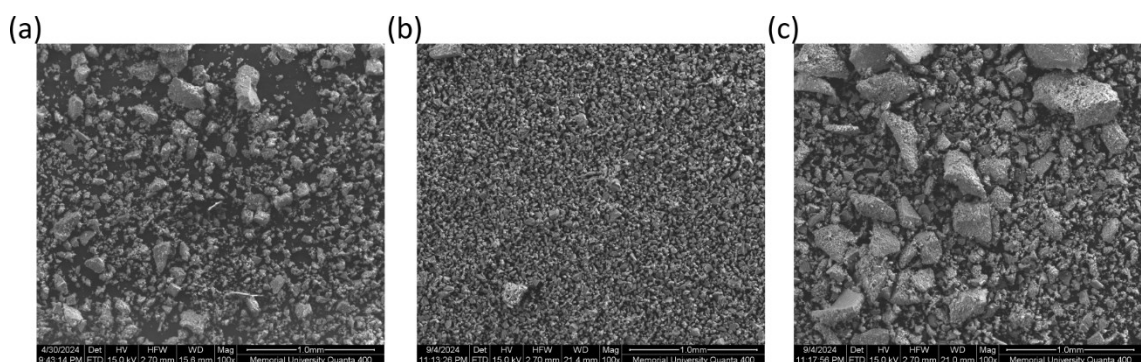


Figure 3.25 SEM images of various samples of BzPcMOF at 100 \times magnification. (a) Fresh BzPcMOF, (b) 6 month old BzPcMOF, (c) 6 month old BzPcMOF after being submerged in water for one week.

This provides BzPcMOF with an interesting niche, in terms of its applicability: Its external surface area can be adjusted through judicious use of time and water. If BzPcMOF ends up filling an industrial role that requires a low external surface area, then any samples of BzPcMOF whose large particles have separated into their constituent pieces over time can be mended through submersion in distilled water. To the inverse effect, if an application requires a large external surface area, then aging a sample of BzPcMOF will only make it more ideal for the task. It remains to be seen how this unique behaviour can be best utilized, but it is certainly promising that BzPcMOF possesses both temporal and water stability, and that any changes caused by one can be reverted by way of the other.

3.3 Conclusions

The principal goal of this project was to refine the BzPcMOF synthesis such that surface areas in excess of 600 m²/g could be regularly achieved. To this end, the project was successful – in fact, surface areas exceeding 1000 m²/g can now be consistently achieved. This level of consistency was reached through probing various facets of the synthesis and assessing how the properties of the resulting material changed. In particular, it was learned that BzPcMOF is highly sensitive to [HCl], and adjusting the synthesis accordingly has allowed for high and consistent surface areas to be met.

The second goal was to acquire the crystal structure of BzPcMOF. Given that the MOF produced few peaks via XRD and could not be grown as a single crystal, the crystal structure was not determined during this work and remains unknown. Several possible crystal structures were ruled out through a trial-and-error process of comparing simulated diffractograms against experimental diffractograms, narrowing down the list of potential topologies.

While the crystal structure of BzPcMOF remains elusive, this work effectively sets the stage for another researcher to inherit the curiosities of BzPcMOF. Now, the subsequent scientist who works on BzPcMOF will have, from the outset, a refined synthesis in hand and an understanding of BzPcMOF's morphology and stability. They will not need to fight to acquire reasonable surface areas. Instead, they will be able to attain them immediately through the changes made to the synthesis in this work. They will know about the unique

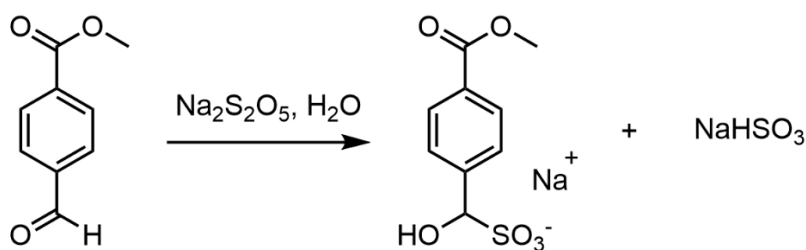
nature of BzPcMOF's temporal/hydro stability, and this will allow them to better investigate potential applications of BzPcMOF (e.g., water splitting).

3.4 Experimental

3.4.1 Materials and methods

Nickel(II) chloride, *N*-methyl-2-pyrrolidone, 1-pentanol, benzoic acid, *N,N*-dimethylacetamide (DMAc) and 1,8-diazabicyclo(5.4.0)undec-7-ene (DBU) were obtained from Sigma Aldrich. Sodium metabisulfite, glacial acetic acid, and *N,N*-dimethylformamide (DMF) were obtained from ACP Chemicals. 4,5-Diaminophthalonitrile was obtained from Aaron Chemicals. Methyl 4-formylbenzoate was obtained from Combi-Blocks. ACS Grade hydrochloric acid was obtained from VWR Chemicals. All chemicals were used as received, with no further purification.

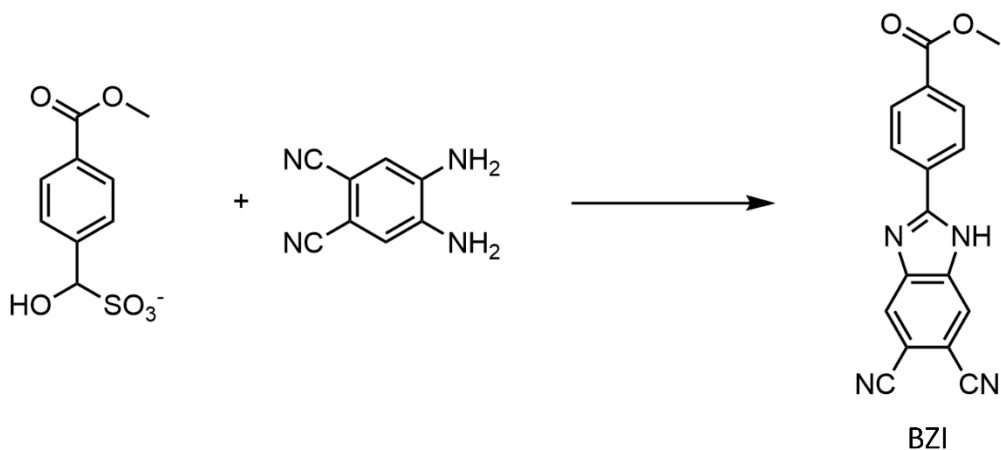
3.4.2 Synthesis of adduct



To a 250 mL round-bottom flask containing a stir bar, 5.34 g (32.5 mmol) of methyl-4-formylbenzoate and 100 mL of 95% ethanol were added. The mixture was allowed to stir until all the solid dissolved. Separately, in a 50 mL beaker, 3.20 g (16.8 mmol) of sodium metabisulfite was dissolved in 20 mL of deionized water.

The sodium metabisulfite solution was added dropwise to the methyl-4-formylbenzoate solution. A white precipitate immediately formed in the colourless solution. Once the solution was completely added, an additional aliquot of 50 mL 95% EtOH was added, and the mixture was left to stir for 30 min. While the stirring occurred, 180 mL of 95% EtOH was chilled in the fridge for the washing step. After 30 min, the mixture was suction filtered and the solid was washed with the chilled EtOH. The final product was a fluffy white solid. No characterization was performed. (Yield: 4.20 g, 94%).

3.4.3 Synthesis of benzimidazole

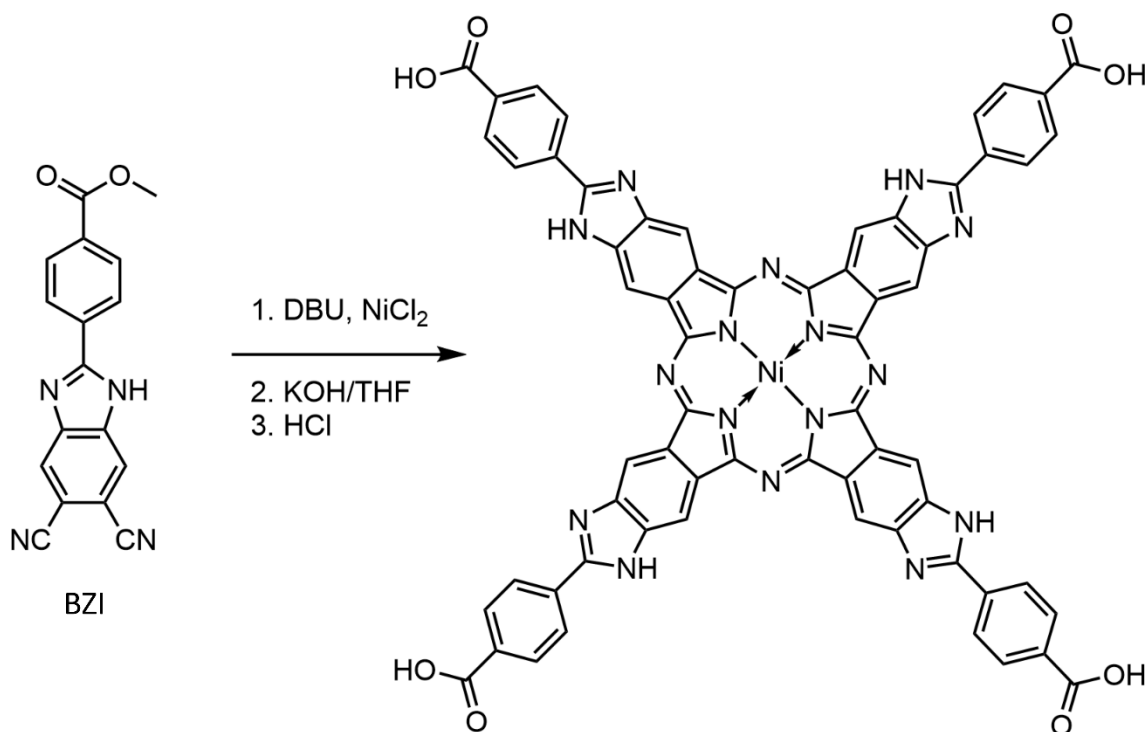


To a microwave vial, 914 mg 4,5-diaminophthalonitrile (5.78 mmol), 1.76 g (6.56 mmol) of the bisulfite adduct, and 12 mL *N*-methyl-2-pyrrolidone were added. A stir bar was then added, and the vial was capped, crimped, and briefly sonicated to give a brown mixture. The vial was clamped in place above a stir plate, and a syringe needle was punctured through the rubber septum of the vial cap to act as a vent while another needle flowing N₂ gas was also punctured through the septum. The vial was purged with N₂ under stirring for 10 min, and then both needles were removed. The vessel was then heated with stirring at

120 °C for 6 h. The reaction mixture became a clear dark brown solution. Then, the heating was stopped and the stirring continued overnight at room temperature. The next day, a yellow precipitate that was difficult to remove from the vial had formed; the solution remained clear and brown. To make retrieval easier, the sample was heated back up to 100 °C until the solution became a dark brown homogeneous solution again. Then, heating and stirring were stopped and the vial was allowed to cool down. The vial was vented with a syringe needle and the cap was removed. The vial's contents were transferred into a 500 mL Erlenmeyer flask. 300 mL of deionized water was added and the product crashed out as a bright yellow precipitate. To rinse the microwave vial, it was filled with deionized water and briefly sonicated.

The mixture was transferred to a 50 mL falcon tube and isolated by successive centrifugations and the supernatant solution was decanted. To wash the product, 200 mL of a 1:1 solution of EtOH:H₂O was prepared. For each washing, 20 mL of the solution was added to the centrifuge tube and the mixture was stirred for 5 min to encourage dissolution of impurities. The washing procedure was repeated 10 times, at which point the decanted solution changed from a strong orange colour to a pale yellow colour. The final solid was placed in the oven at 80 °C overnight to dry before it was collected the next morning as a powdery yellow solid. (Yield: 1.06 g, 61%). ¹H-NMR (300 Mz, DMSO-*d*₆) δ 8.45 (s, 2H), 8.36 (d, 8.6 Hz, 2H), 8.15 (d, 8.6 Hz, 2H), 3.91 (s, 3H). Imidazolyl N-H was not observed.

3.4.4 One-pot conversion of BZI to Ni-BzPcLinker



To a clean dry 20 mL microwave vial, 740 mg BZI (2.45 mmol), 110 mg (0.849 mmol) NiCl₂, and 12 mL 1-pentanol were combined. A stir bar was added, and the vial was capped, crimped, and briefly sonicated to produce a brown mixture. The vial was clamped in place above a stir plate, and a syringe needle was punctured through the rubber septum of the vial cap to act as a vent. A needle flowing N₂ gas was then punctured through the septum. The vial was purged with N₂ under stirring for 10 min, and then both needles were removed. The vial was then transferred to an oil bath and heated to 145 °C, where it was allowed to equilibrate for 10 min as it slowly took on a deep black colour. The vial was carefully vented using a syringe needle, which caused the solution inside to bubble. 1.00 mL (6.70 mmol) of DBU was measured with a syringe and then carefully added to the vial through the septum, which caused white fumes to evolve from the black solution.

The vial was left to react for 72 h, after which the vial was removed from the oil bath and allowed to come to room temperature. Once the vial cooled, accumulated pressure was vented by puncturing the septum of the vial with a needle. The vial was uncrimped and the reaction mixture was transferred to a 100 mL round-bottom flask. 26 mL of 2 M KOH was added to the round-bottom flask, and then 12 mL of THF was used to rinse the vial into the flask, as the product at this stage is soluble in THF.

A condenser was attached to the round-bottom flask and the round-bottom flask was seated in a heating mantle. For 48 h, the mixture was placed under reflux at 85 °C.

The dark mixture along with its stir bar was then transferred to a 250 mL Erlenmeyer flask, and 75 mL of 1 M HCl was added. The new mixture was stirred at room temperature for 24 h to promote the protonation of the linker.

After 24 h, the product was isolated by transferring 25 mL of the reaction mixture to a 50 mL Falcon centrifuge tube, adding 10 mL deionized water, and centrifuging the tube. The product settled on the bottom, while impurities floated in the thin layer of THF on top. The solution was carefully decanted, and the process was repeated with another 25 mL aliquot of reaction mixture, until all of the reaction mixture had been centrifuged.

15 mL of DMF was added to the isolated solid and the tube was sonicated and vigorously shaken, before 15 mL ethyl acetate was added, and the tube was shaken again. The tube was centrifuged, and the resulting dark brown solution was decanted. This DMF+EtOAc wash process was repeated until the resulting solution was a very light brown colour. Finally, the solid was washed an additional 3 times with 15 mL of deionized water, also

via centrifuge. The solid was dried by placing it in the oven at 80 °C overnight (approx. 16 h) and was collected the next day as a dark green solid powder. (Yield = 0.469 g, 33.5%).

3.4.5 Synthesis of BzPcMOF

To a clean dry 50 mL Duran® vial, 140 mg fresh (i.e., retrieved from the glovebox the same day) ZrCl₄, 1.800 g benzoic acid, and 24.0 mL of DMF were added. The mixture was sonicated for 10 min, at which point it became a clear colourless solution. The vial was placed in the oven at 80 °C for 1 h. After 1 h passed, the vial was removed from the oven and allowed to cool to room temperature. Then, 35.2 mg of the Ni-BzPcLinker was added. To add 80 µL of HCl to the sample, 1 mL of HCl was added to 5 mL DMF, and 480 µL of the resulting solution was transferred via autopipette into the sample. Then, the vial was sonicated for 1 h. The vial was then placed in the oven at 120 °C for 72 h. After 72 h, a fluffy green-black solid was floating in the clear yellow-brown solution.

The reaction mixture was transferred to a 50 mL Falcon centrifuge tube and centrifuged. The mother liquor was decanted off and 15 mL of DMF was added. The tube was vigorously shaken and centrifuged again. The DMF was decanted off, and the process was repeated another 2 times. Finally, after 3 washes, 15 mL DMF was added, and the vial was allowed to sit on the bench at room temperature overnight.

The next day, the tube was centrifuged, the DMF was decanted, and 15 mL acetone was added. The tube was vigorously shaken and centrifuged again. The acetone was decanted

off, and the process was repeated another 2 times. Finally, after 3 washes, 15 mL acetone was added, and the vial was allowed to sit on the bench at room temperature overnight.

The following day, the tube was centrifuged, the acetone decanted, and the sample was then placed in the oven at 80 °C for 90 min to dry. The final product was a fine black powder.

3.4.6 MOF activation

The collected sample was transferred to a pre-weighed Micromeritics 3Flex tube. All samples were activated on a Micromeritics Smart VacPrep by evacuating the sample at a rate of 5 mmHg/s for 120 min. Then, the sample was heated at a rate of 5.0 °C/min until it reached 120 °C, where it was held for 600 min.

3.4.7 Gas adsorption

Nitrogen gas adsorption isotherms (77 K) were taken on a Micromeritics TriStar II instrument. Surface areas were calculated by BET theory using the Micromeritics Microactive software suite, ensuring that the four-point criteria⁸⁷ were met for all samples.

3.4.8 LDI-MS

LDI mass spectra were collected on a Bruker ultrafleXtreme MALDI-TOF/TOF mass spectrometer. Samples were prepared by dispersing 10 mg of BzPcLinker in 1 mL of THF and sonicating the mixture. The BzPcLinker was insoluble in THF, so the mixture was

sonicated until the particles appeared finely dispersed. Then, 0.5 μL of the sample was spotted on the plate for analysis.

3.4.9 SEM

Scanning electron microscope images were collected on a FEI Quanta 400 at 10.00 kV. EDX analysis was performed with a Bruker XFlash 4010 EDX detector. The samples were not gold plated prior to analysis.

Chapter 4

Future Work

The work contained in this thesis investigated the synthesis of UiO-66 by ^2H -NMR and explored the reaction space of the synthesis of BzPcMOF. The ^2H -NMR work has succeeded in demonstrating what can be learned from UiO-66, but it does not mark the end of that project. Many questions regarding the reaction persist, and there remain aspects of the synthesis that have not yet been explored. Likewise, while the BzPcMOF work clearly demonstrated our ability to reproducibly synthesize a material, the structure of BzPcMOF remains unknown. I believe that the critical barrier to publishing the BzPcMOF work is the determination of the MOF's crystal structure, and once determined, this crystal structure may give rise to the parameter space necessary for other BzPcMOFs. This chapter explores some of the ideas for further work that build on each of these projects.

4.1 Following MOF synthesis via ^2H -NMR

As the research in this thesis contained the first known foray into the use of ^2H -NMR for reaction monitoring of MOF formation, much of the work performed during my thesis was in the interest of assessing what could be learned from this analytical process, and how. There were concepts that were superficially probed during this research, but which did not receive the thorough experimentation that they deserved – there remains a great deal yet to be learned from the synthesis of UiO-66, and by extension, other MOFs.

4.1.1 Deuterated solvent

Earlier in this work, it was hypothesized that DMF hydrolysis was responsible for the changes to the acidity of the reaction mixture in the HCl and BA syntheses, but the limited data were not able to provide any further insight. Some preliminary experiments were conducted to better assess DMF's role, but time constraints only permitted a narrow window of examination. It was hoped that experiments on DMF would allow more to be learned about the role of the solvent in the synthesis of UiO-66, such as when hydrolysis begins, when hydrolysis ends, whether hydrolysis occurs in every synthesis, and whether hydrolysis occurs to a greater extent in some syntheses than others.

We briefly explored this by employing a small amount of DMF- d_7 to the reaction mixture (15 μ L of DMF- d_7 in a 1 mL aliquot of solution); this allowed the ability to follow the characteristic peaks of DMF, as well as the peaks associated with its hydrolysis products. A few preliminary experiments were performed this way, including experiments with the standard syntheses under the effects of all 3 modulators, but there was not enough time to explore this line of research with the depth it deserved. What was learned from these initial experiments provided equally many questions as answers.

When the concentration of the formyl deuteron of DMF- d_7 during the synthesis of UiO-66 was followed via $^2\text{H-NMR}$, DMF appeared to show markedly different behaviours under the effects of each of the three modulators (Figure 4.1). UiO-66-AA appeared to show no decomposition of DMF (Figure 4.1 (a)), UiO-66-HCl showed significant decomposition of DMF after 50 min had elapsed (Figure 4.1 (b)), and UiO-66-BA appeared to show an initial

brief decomposition of DMF, followed by the concentration levelling off (Figure 4.1 (c)). Though UiO-66-AA showed no evidence of DMF hydrolysis, it is possible that the process was occurring on a small enough scale such that it could not be observed with $^2\text{H-NMR}$.

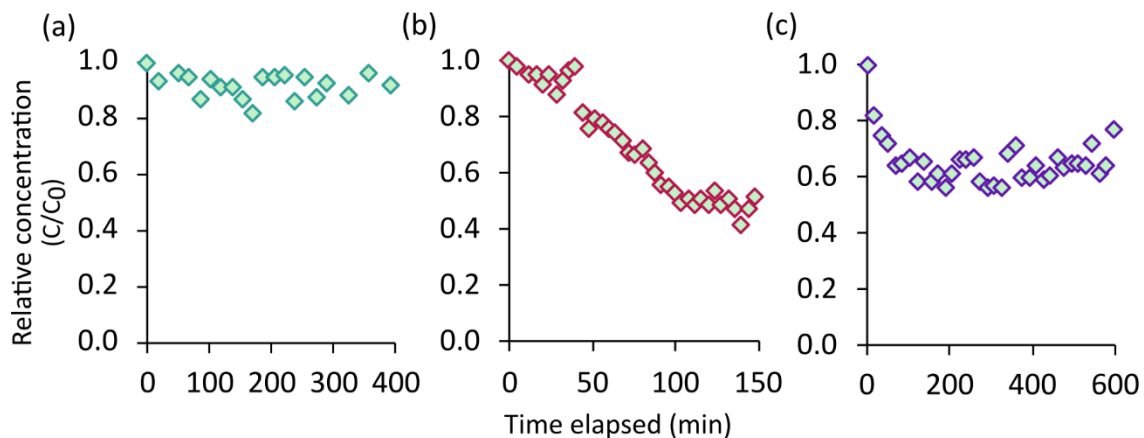


Figure 4.1 Relative DMF concentrations over time in various UiO-66 standard syntheses as determined using DMF's formyl deuterium for: (a) UiO-66-AA, (b) UiO-66-HCl, (c) UiO-66-BA.

The data from these DMF- d_7 experiments could be further assessed by examining the DMF- d_7 methyl peaks (ca. 3.0 ppm; Figure 4.2). We discovered that the peak from dimethylamine was observed as a shoulder on DMF's rightmost methyl peak. When this assessment was performed with the same data used to form Figure 4.1, it was noted that the UiO-66-HCl experiment was the only one to show evidence of DMF decomposition products (Figure 4.2 (b)). This is most curious, as the UiO-66-BA synthesis appeared to show immediate hydrolysis, yet no hydrolysis products are present at any time on the spectra; it is possible that this is because any hydrolysis products being formed are immediately joining the solid/oligomer phase, which is not visible via $^2\text{H-NMR}$, or the gas phase. In order to identify any species present in the gas phase, future work on this project could include headspace analysis via gas chromatography mass spectrometry (GC-MS).

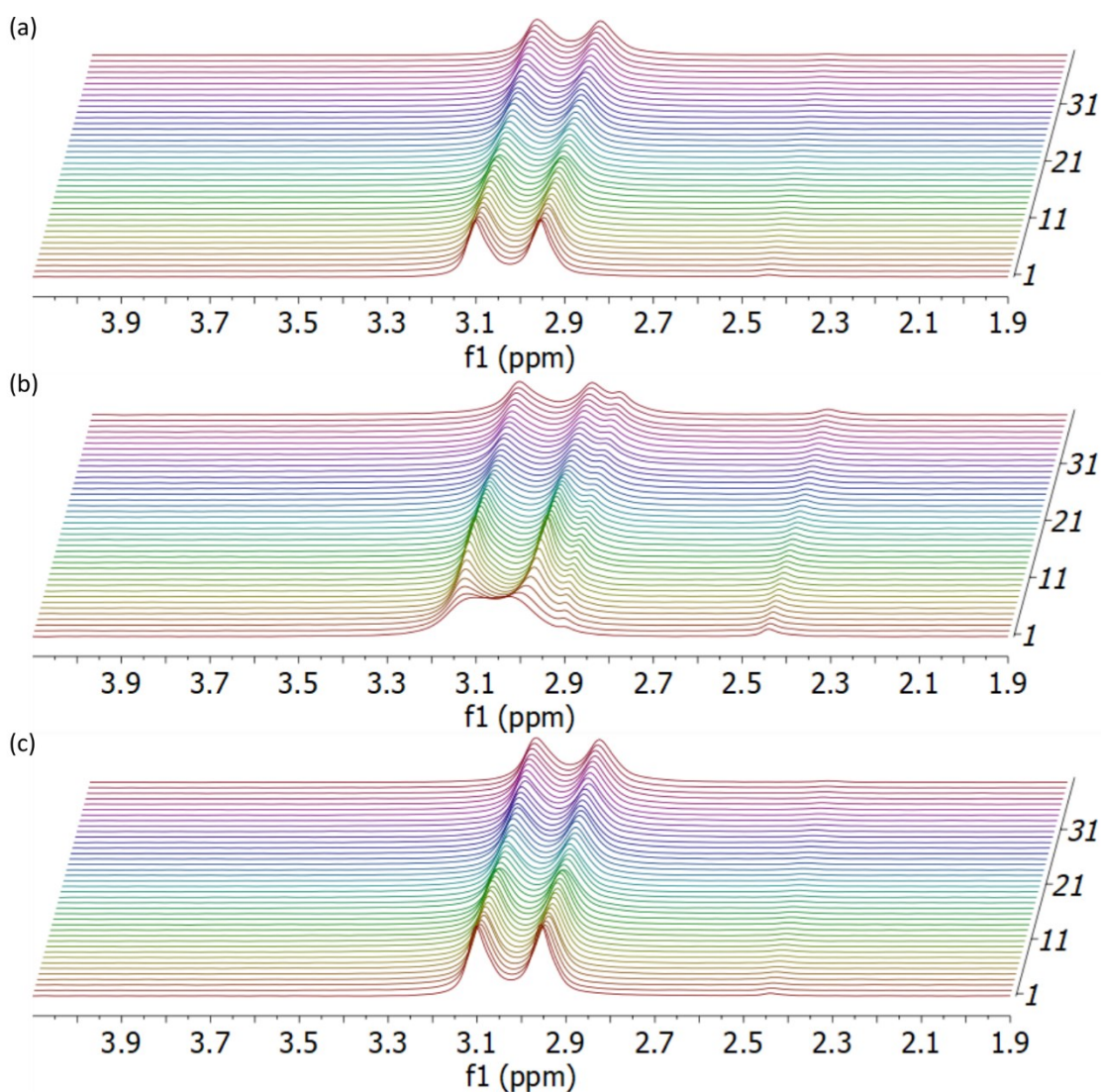


Figure 4.2 Stacked ^2H -NMR spectra of the methyl- d_3 peaks of $\text{DMF-}d_7$ from the standard syntheses of (a) UiO-66-AA, (b) UiO-66-HCl, (c) UiO-66-BA. The peak at 2.44 is from the internal standard (i.e., $\text{TMSP-}d_4$).

The only thing that was determined with any certainty from these initial experiments was that DMF hydrolysis was occurring in the synthesis of UiO-66-HCl. Further experimentation would allow for a much more thorough understanding of the role of DMF. Analysis of DMF during the process of pre-conditioning could be performed for each modulator, as well as during the synthesis of UiO-66 with pre-conditioned ZrCl_4 in DMF

and modulator. This would allow one to better understand the extent of hydrolysis during the pre-conditioning experiments, and the behaviour of the hydrolysis products in the subsequent synthesis. If DMF hydrolysis proceeds until equilibrium during the pre-conditioning phase, then one may be able to say that any changes to the concentration of hydrolysis products in the reaction mixture after pre-conditioning are due to their participation in the self-assembly of UiO-66.

4.1.2 Deuterated modulator

The identity of the modulator used in the synthesis of UiO-66 is evidently of great importance, given the differences seen between the products of the various syntheses, but the mechanisms by which these modulators operate are still largely unknown. The concentration of coordinating modulators (i.e., AA and BA) can be explored via ^2H -NMR by using deuterated modulator. Due to time constraints, the only modulator experiments performed were with the standard syntheses of UiO-66-AA and UiO-66-BA (Figure 4.3).

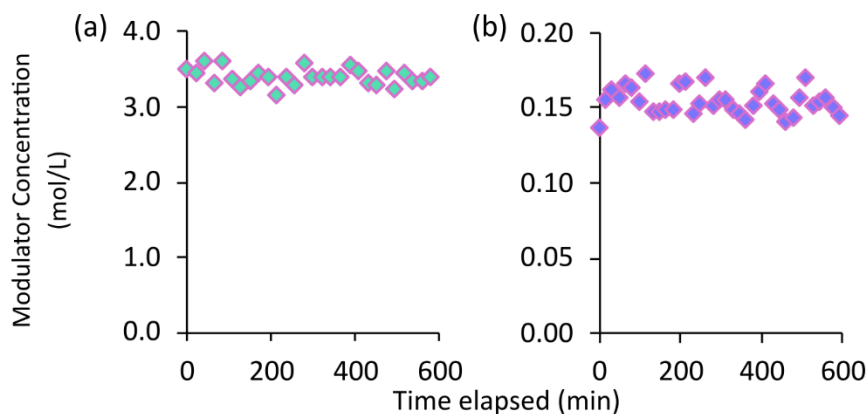


Figure 4.3 Concentrations of modulator in solution in the standard synthesis of UiO-66.
a) UiO-66-AA, b) UiO-66-BA.

These experiments were unable to elucidate much. The concentration of AA appeared to change very little over the course of the experiment (Figure 4.3 (a)), while the concentration of BA appeared to suggest a potentially slow downward trend (Figure 4.3 (b)), suggesting it was leaving solution more permanently. These differences may be due to the large difference in concentrations of AA vs. BA (Table 2.2 in Chapter 2). These preliminary data are intriguing but further experimentation could produce more nuanced insight into the role of modulator in MOF synthesis.

If one were to perform an experiment where they follow the pre-conditioning of $ZrCl_4$ in DMF and deuterated modulator in order to watch the cluster forming, then they could follow the concentration of modulator in solution as the sample is pre-conditioned. In this case, one would presumably see the concentration of modulator decrease over time as the nodes form and the modulators, out of necessity, coordinate to them. This may provide further insight into when the $Zr_6O_4(OH)_4$ forms in solution.

One could also perform the pre-conditioning process with deuterated modulator before the experiment, add linker, and then initiate the synthesis of UiO-66. In this case, one may see the modulator concentration increase over time as molecules of modulator begin to dissociate from the nodes and become replaced by linker. One could even add deuterated linker to this experiment (assuming its peaks do not overlap with the modulator's peaks) and expect to see linker concentration decrease as modulator concentration increases. This could help elucidate the acid-assisted dissociation mechanism that was hypothesized to be at play in the synthesis of UiO-66.

The research in this thesis provided significant evidence as to the idea that different modulators influence the reaction in different ways, but the exact nature of those differences are still unknown to us. What is so different about benzoic acid and acetic acid that, despite both being coordinating modulators, they cause different degrees of defectivity, differently shaped particles, and different induction periods (or lack thereof)? Further investigation into any of these queries would help elucidate what is, currently, a poorly understood component of MOF synthesis. Furthermore, if methodology to examine MOF formation can be determined via modulator alone, then it is possible to follow MOF formation for linkers that are too challenging to synthesize with ^2H groups.

4.2 Synthesizing phthalocyanine MOFs

The research involving the BzPcLinker and the BzPcMOF has now been passed through four sets of hands in our research group – it is a difficult topic of research by its very nature of involving a macrocycle that is difficult to manipulate. Knowing that future work will meet some of the same difficulties I encountered in my research, there are avenues of future work that will be optimal for further development of this MOF.

4.2.1 Experiments with pre-conditioning

The standard synthesis of BzPcMOF involves pre-conditioning ZrCl_4 in DMF and BA in the oven for 1 h before the addition of linker and HCl. Given what has been learned from the ^2H -NMR work in Chapter 2, there is abundant reason to suspect that chemical activity is occurring in the reaction mixture during this time. However, the breadth and depth of

this pre-conditioning process was not explored in this work. This is a shame, as there are many points of interest that arise from the pre-conditioning process.

First, the pre-conditioning of $ZrCl_4$ in DMF and BA was explored in Chapter 2, but only for the concentration specific to the synthesis of UiO-66-BA. There is a large difference in the concentration of BA in each of these syntheses (0.137 M in UiO-66-BA synthesis vs 0.602 M in BzPcMOF synthesis), so it would be advantageous to use D_2O to follow the pre-conditioning of $ZrCl_4$ in DMF and BA according to the BzPcMOF synthesis. This would provide insight into what is occurring in terms of pH and water activity during the pre-conditioning phase of the BzPcMOF synthesis, and whether the process is resolved within the 60 min timeframe.

That leads into the second point of interest: The D_2O data from the BA experiments in Chapter 2 implied that, during the process of pre-conditioning, some behaviour was taking place that lasted for ~500 min – this timeframe is a significant departure from the 60 min pre-conditioning process for the BzPcMOF. It is possible that the timeframe is related to the concentration of BA in solution, but even so, it would be advantageous to experiment with the time period for such pre-conditioning. It may be the case that 60 min is an insufficient amount of time to allow the node to form, and 500 min would produce a solution that contains more fully formed nodes. This may allow the self-assembly process to proceed even more slowly, which could aid in producing a larger crystalline product that could be characterized by single crystal X-ray diffraction.

Third, in the synthesis of the BzPcMOF, there was the distinct choice to add HCl to solution after the 1 h process of pre-conditioning $ZrCl_4$ in DMF and BA was complete. It may be

worth assessing the effects of adding HCl at the same time as BA, or perhaps even adding the HCl first, then the BA after the pre-conditioning. It may end up being the case that the hydrolysis of DMF and the behaviours of its hydrolysis products allow the synthesis of BzPcMOF to proceed at an accelerated rate. It is also possible that this change would decelerate the synthesis. It is impossible to say for sure without further experimentation, since the behaviours of the UiO-66 synthesis cannot necessarily be expected to occur in the synthesis of an entirely different MOF, despite the similarity of their reagents.

These are but a few ideas of how the pre-conditioning process could be probed. Even if there are no surface area increases or large single crystals produced as a result, it would still be advantageous to have a more robust understanding of what is occurring in solution.

4.2.2 Alternate solvents

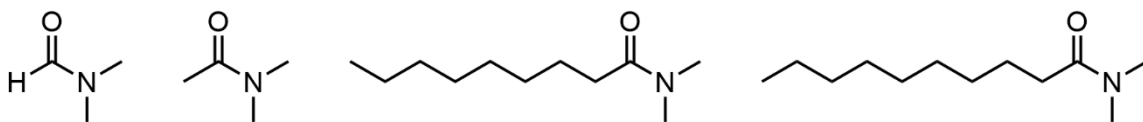


Figure 4.4 From left to right: *N,N*-dimethylformamide (DMF), *N,N*-dimethylacetamide (DMAc), *N,N*-dimethylnonanamide, *N,N*-dimethyldecanamide.

The experiment where DMAc was used to synthesize BzPcMOF instead of DMF made it plain that the choice of solvent has an impact on the appearance of the resulting MOF – to this end, other solvents or solvent systems could be explored (Figure 4.4). Given that DMF and DMAc have successfully been used to synthesize BzPcMOF, perhaps other dimethylamides will also prove effective. The chemical *N,N*-dimethylnonanamide is structurally similar to DMF, except that it has an eight-carbon alkyl chain in place of

DMF's single formyl proton. There are other similar derivatives of DMF, any of which could be a contender for the principal solvent or a co-solvent of the BzPcMOF synthesis. Some of these derivatives, such as *N,N*-dimethyldecanamide, are naturally derived, which would also provide the synthesis a green advantage if they could be used to success. These alternate solvents may produce samples of BzPcMOF with different appearances – perhaps even single crystals – and would alleviate the issues associated with the use of DMF (increasing regulation, challenging chemical waste).

In addition to these dimethylamides, there exist amides without dimethyl groups which may also be worth exploring. *N*-methyl-2-pyrrolidone (NMP) was used earlier in this work in the synthesis of the benzimidazole during the BzPcMOF work, but it was not explored as a solvent for BzPcMOF synthesis. In addition, *N,N*-diethylformamide (DEF) is used frequently in the syntheses of other MOFs, so it is also an excellent candidate. These or any other of the numerous amide solvents should also be explored in the synthesis of BzPcMOF.

4.2.3 Growing a single crystal of MOF

One of the goals of this project that was never fulfilled was the acquisition of the crystal structure of the BzPcMOF. Many attempts were made to do so both by direct collection and by reverse-engineering the structure from its powder X-ray diffractogram. Several samples of BzPcMOF were synthesized and then sifted through underneath a microscope in the hopes of finding a suitable crystal for single-crystal XRD, to no success.

It would be ideal to have a confirmed crystal structure of BzPcMOF (to inform stoichiometric ratios, to allow for the MOF to be registered with the CCDC, and to include when the MOF is, ideally, published one day), so future work on this project should still attempt to acquire this structure. Crystal growth, however, is famously stochastic and very few MOFs form large single crystals when synthesized. What efficiently grows single crystals for one MOF could completely stunt the growth of another MOF, so there is no universal approach to crystal growth.

Observations regarding the available headspace in a reaction vessel from Chapter 2 and literature precedent¹³³ suggest that, as headspace in a MOF reaction vessel decreases, the induction time increases. This concept of headspace as it relates to MOF kinetics is sorely underexplored and would make for an intriguing avenue of research for the BzPcMOF work. In the literature, this phenomenon is hypothesized to be related to the interactions between oxygen in the headspace and formyl protons in the solvent. Since BzPcMOF is synthesized in DMF, this trend could very well apply to the synthesis of the BzPcMOF. During the experiments with the optimization of the BzPcMOF synthesis, a single experiment with headspace was performed. However, in that experiment, the amount of headspace in the vessel was increased, not decreased, and the only analysis performed on the resulting MOF was on its surface area, which was not significantly different from the control. Thus, future experiments with headspace in the synthesis of BzPcMOF should seek to incrementally minimize the headspace and should analyse more than just the surface area of the resulting sample. In particular, it would be worth taking any samples beneath a microscope to look for single crystals.

Overall, through the work presented in this thesis, there is every reason to feel optimistic that the future of MOF chemistry will avail of the data offered by ^2H -NMR. Insight into MOF formation for a variety of known systems can be examined with ^2H -NMR, and this, in turn, may assist in the syntheses of novel MOFs such as BzPcMOF. Now that a reproducible synthesis of BzPcMOF is available, future chemists can further unravel the eccentricities of this material, including its potential applications, reactivity, and gas adsorption properties.

References

- (1) Somorjai, G. A. *Introduction to Surface Chemistry and Catalysis*, 2nd ed.; Wiley: Hoboken, N.J, 2010.
- (2) Yakukhnov, S. A.; Pentsak, E. O.; Galkin, K. I.; Mironenko, R. M.; Drozdov, V. A.; Likholobov, V. A.; Ananikov, V. P. Rapid “Mix-and-Stir” Preparation of Well-Defined Palladium on Carbon Catalysts for Efficient Practical Use. *ChemCatChem* **2018**, *10* (8), 1869–1873. <https://doi.org/10.1002/cctc.201700738>.
- (3) Cao, S.; Franklin (Feng) Tao; Tang, Y.; Li, Y.; Yu, J. Size- and Shape-Dependent Catalytic Performances of Oxidation and Reduction Reactions on Nanocatalysts. *Chemical Society Reviews* **2016**, *45* (17), 4747–4765. <https://doi.org/10.1039/C6CS00094K>.
- (4) Rougier, A.; Soiron, S.; Haihal, I.; Aymard, L.; Taouk, B.; Tarascon, J.-M. Influence of Grinding on the Catalytic Properties of Oxides. *Powder Technology* **2002**, *128* (2), 139–147. [https://doi.org/10.1016/S0032-5910\(02\)00191-2](https://doi.org/10.1016/S0032-5910(02)00191-2).
- (5) Dąbrowski, A. Adsorption — from Theory to Practice. *Advances in Colloid and Interface Science* **2001**, *93* (1), 135–224. [https://doi.org/10.1016/S0001-8686\(00\)00082-8](https://doi.org/10.1016/S0001-8686(00)00082-8).
- (6) Wu, Z.; Wee, V.; Ma, X.; Zhao, D. Adsorbed Natural Gas Storage for Onboard Applications. *Advanced Sustainable Systems* **2021**, *5* (4), 2000200. <https://doi.org/10.1002/adisu.202000200>.
- (7) Abbas, T.; Kajjumba, G. W.; Ejjada, M.; Masrura, S. U.; Marti, E. J.; Khan, E.; Jones-Lepp, T. L. Recent Advancements in the Removal of Cyanotoxins from Water Using Conventional and Modified Adsorbents—A Contemporary Review. *Water* **2020**, *12* (10), 2756. <https://doi.org/10.3390/w12102756>.
- (8) LaPotin, A.; Kim, H.; Rao, S. R.; Wang, E. N. Adsorption-Based Atmospheric Water Harvesting: Impact of Material and Component Properties on System-Level Performance. *Accounts of Chemical Research* **2019**, *52* (6), 1588–1597. <https://doi.org/10.1021/acs.accounts.9b00062>.
- (9) Sizmur, T.; Fresno, T.; Akgül, G.; Frost, H.; Moreno-Jiménez, E. Biochar Modification to Enhance Sorption of Inorganics from Water. *Bioresource Technology* **2017**, *246*, 34–47. <https://doi.org/10.1016/j.biortech.2017.07.082>.
- (10) Gibson, L. T. Mesosilica Materials and Organic Pollutant Adsorption: Part A Removal from Air. *Chemical Society Reviews* **2014**, *43* (15), 5163–5172. <https://doi.org/10.1039/C3CS60096C>.
- (11) Sowards, K.; Medina, H. Hierarchical Enhanced Surface Area Structures and Their Associated Applications with Titania. *Applied Materials Today* **2023**, *35*, 101962. <https://doi.org/10.1016/j.apmt.2023.101962>.
- (12) Leng, L.; Xiong, Q.; Yang, L.; Li, H.; Zhou, Y.; Zhang, W.; Jiang, S.; Li, H.; Huang, H. An Overview on Engineering the Surface Area and Porosity of Biochar. *Science of The Total Environment* **2021**, *763*, 144204. <https://doi.org/10.1016/j.scitotenv.2020.144204>.

- (13) Guisbiers, G.; Mejía-Rosales, S.; Leonard Deepak, F. Nanomaterial Properties: Size and Shape Dependencies. *Journal of Nanomaterials* **2012**, *2012* (1), 180976. <https://doi.org/10.1155/2012/180976>.
- (14) Pérez-Botella, E.; Valencia, S.; Rey, F. Zeolites in Adsorption Processes: State of the Art and Future Prospects. *Chemical Reviews* **2022**, *122* (24), 17647–17695. <https://doi.org/10.1021/acs.chemrev.2c00140>.
- (15) Azam, K.; Shezad, N.; Shafiq, I.; Akhter, P.; Akhtar, F.; Jamil, F.; Shafique, S.; Park, Y.-K.; Hussain, M. A Review on Activated Carbon Modifications for the Treatment of Wastewater Containing Anionic Dyes. *Chemosphere* **2022**, *306*, 135566. <https://doi.org/10.1016/j.chemosphere.2022.135566>.
- (16) Hong-Cai “Joe” Zhou; Kitagawa, S. Metal–Organic Frameworks (MOFs). *Chemical Society Reviews* **2014**, *43* (16), 5415–5418. <https://doi.org/10.1039/C4CS90059F>.
- (17) Freund, R.; Zaremba, O.; Arnauts, G.; Ameloot, R.; Skorupskii, G.; Dincă, M.; Bavykina, A.; Gascon, J.; Ejsmont, A.; Goscianska, J.; Kalmutzki, M.; Lächelt, U.; Ploetz, E.; Diercks, C. S.; Wuttke, S. The Current Status of MOF and COF Applications. *Angewandte Chemie International Edition* **2021**, *60* (45), 23975–24001. <https://doi.org/10.1002/anie.202106259>.
- (18) Chen, Z.; Kirlikovali, K. O.; Li, P.; Farha, O. K. Reticular Chemistry for Highly Porous Metal–Organic Frameworks: The Chemistry and Applications. *Accounts of Chemical Research* **2022**, *55* (4), 579–591. <https://doi.org/10.1021/acs.accounts.1c00707>.
- (19) Farha, O. K.; Eryazici, I.; Jeong, N. C.; Hauser, B. G.; Wilmer, C. E.; Sarjeant, A. A.; Snurr, R. Q.; Nguyen, S. T.; Yazaydin, A. Ö.; Hupp, J. T. Metal–Organic Framework Materials with Ultrahigh Surface Areas: Is the Sky the Limit? *Journal of the American Chemical Society* **2012**, *134* (36), 15016–15021. <https://doi.org/10.1021/ja3055639>.
- (20) Furukawa, H.; Cordova, K. E.; O’Keeffe, M.; Yaghi, O. M. The Chemistry and Applications of Metal–Organic Frameworks. *Science* **2013**, *341* (6149), 1230444. <https://doi.org/10.1126/science.1230444>.
- (21) Li, H.; Eddaoudi, M.; O’Keeffe, M.; Yaghi, O. M. Design and Synthesis of an Exceptionally Stable and Highly Porous Metal–Organic Framework. *Nature* **1999**, *402* (6759), 276–279. <https://doi.org/10.1038/46248>.
- (22) Troyano, J.; Carné-Sánchez, A.; Avci, C.; Imaz, I.; Maspoch, D. Colloidal Metal–Organic Framework Particles: The Pioneering Case of ZIF-8. *Chemical Society Reviews* **2019**, *48* (23), 5534–5546. <https://doi.org/10.1039/C9CS00472F>.
- (23) Hyeak Choe, J.; Kim, H.; Seop Hong, C. MOF-74 Type Variants for CO₂ Capture. *Materials Chemistry Frontiers* **2021**, *5* (14), 5172–5185. <https://doi.org/10.1039/D1QM00205H>.
- (24) Ming, Y.; Kumar, N.; Siegel, D. J. Water Adsorption and Insertion in MOF-5. *ACS Omega* **2017**, *2* (8), 4921–4928. <https://doi.org/10.1021/acsomega.7b01129>.
- (25) Kumar Gangu, K.; Maddila, S.; B. Jonnalagadda, S. The Pioneering Role of Metal–Organic Framework-5 in Ever-Growing Contemporary Applications – a Review. *RSC Advances* **2022**, *12* (22), 14282–14298. <https://doi.org/10.1039/D2RA01505F>.

- (26) Lawrence, M. C.; Katz, M. J. Analysis of the Water Adsorption Isotherms in UiO-Based Metal–Organic Frameworks. *The Journal of Physical Chemistry C* **2022**, *126* (2), 1107–1114. <https://doi.org/10.1021/acs.jpcc.1c05190>.
- (27) Mondloch, J. E.; Katz, M. J.; Planas, N.; Semrouni, D.; Gagliardi, L.; Hupp, J. T.; Farha, O. K. Are Zr₆-Based MOFs Water Stable? Linker Hydrolysis vs. Capillary-Force-Driven Channel Collapse. *Chemical Communications* **2014**, *50* (64), 8944–8946. <https://doi.org/10.1039/C4CC02401J>.
- (28) Cavka, J. H.; Jakobsen, S.; Olsbye, U.; Guillou, N.; Lamberti, C.; Bordiga, S.; Lillerud, K. P. A New Zirconium Inorganic Building Brick Forming Metal Organic Frameworks with Exceptional Stability. *Journal of the American Chemical Society* **2008**, *130* (42), 13850–13851. <https://doi.org/10.1021/ja8057953>.
- (29) Chang, P.-H.; Mukhopadhyay, R.; Zhong, B.; Yang, Q.-Y.; Zhou, S.; Tzou, Y.-M.; Sarkar, B. Synthesis and Characterization of PCN-222 Metal Organic Framework and Its Application for Removing Perfluorooctane Sulfonate from Water. *Journal of Colloid and Interface Science* **2023**, *636*, 459–469. <https://doi.org/10.1016/j.jcis.2023.01.032>.
- (30) Mondloch, J. E.; Bury, W.; Fairen-Jimenez, D.; Kwon, S.; DeMarco, E. J.; Weston, M. H.; Sarjeant, A. A.; Nguyen, S. T.; Stair, P. C.; Snurr, R. Q.; Farha, O. K.; Hupp, J. T. Vapor-Phase Metalation by Atomic Layer Deposition in a Metal–Organic Framework. *Journal of the American Chemical Society* **2013**, *135* (28), 10294–10297. <https://doi.org/10.1021/ja4050828>.
- (31) Furukawa, H.; Gándara, F.; Zhang, Y.-B.; Jiang, J.; Queen, W. L.; Hudson, M. R.; Yaghi, O. M. Water Adsorption in Porous Metal–Organic Frameworks and Related Materials. *Journal of the American Chemical Society* **2014**, *136* (11), 4369–4381. <https://doi.org/10.1021/ja500330a>.
- (32) Winarta, J.; Shan, B.; McIntyre, S. M.; Ye, L.; Wang, C.; Liu, J.; Mu, B. A Decade of UiO-66 Research: A Historic Review of Dynamic Structure, Synthesis Mechanisms, and Characterization Techniques of an Archetypal Metal–Organic Framework. *Crystal Growth & Design* **2020**, *20* (2), 1347–1362. <https://doi.org/10.1021/acs.cgd.9b00955>.
- (33) Cmarik, G. E.; Kim, M.; Cohen, S. M.; Walton, K. S. Tuning the Adsorption Properties of UiO-66 via Ligand Functionalization. *Langmuir* **2012**, *28* (44), 15606–15613. <https://doi.org/10.1021/la3035352>.
- (34) Zornoza, B.; Martinez-Joaristi, A.; Serra-Crespo, P.; Tellez, C.; Coronas, J.; Gascon, J.; Kapteijn, F. Functionalized Flexible MOFs as Fillers in Mixed Matrix Membranes for Highly Selective Separation of CO₂ from CH₄ at Elevated Pressures. *Chemical Communications* **2011**, *47* (33), 9522–9524. <https://doi.org/10.1039/C1CC13431K>.
- (35) Feng, Y.; Wang, R.; Li, M.; Wu, B. UiO-67-Typed Zr-MOFs Modified with Chiral Amine Alcohol Pendants for Adsorption Separation of Chiral Aromatic Alcohol Enantiomers. *Inorganic Chemistry* **2025**. <https://doi.org/10.1021/acs.inorgchem.5c00715>.

- (36) Marshall, R. J.; Forgan, R. S. Postsynthetic Modification of Zirconium Metal–Organic Frameworks. *European Journal of Inorganic Chemistry* **2016**, *2016* (27), 4310–4331. <https://doi.org/10.1002/ejic.201600394>.
- (37) Kouser, S.; Hezam, A.; Khadri, M. J. N.; Khanum, S. A. A Review on Zeolite Imidazole Frameworks: Synthesis, Properties, and Applications. *Journal of Porous Materials* **2022**, *29* (3), 663–681. <https://doi.org/10.1007/s10934-021-01184-z>.
- (38) Zhang, X.; Wasson, M. C.; Shayan, M.; Berdichevsky, E. K.; Ricardo-Noordberg, J.; Singh, Z.; Papazyan, E. K.; Castro, A. J.; Marino, P.; Ajoyan, Z.; Chen, Z.; Islamoglu, T.; Howarth, A. J.; Liu, Y.; Majewski, M. B.; Katz, M. J.; Mondloch, J. E.; Farha, O. K. A Historical Perspective on Porphyrin-Based Metal–Organic Frameworks and Their Applications. *Coordination Chemistry Reviews* **2021**, *429*, 213615. <https://doi.org/10.1016/j.ccr.2020.213615>.
- (39) Bennett, T. D.; Horike, S.; Mauro, J. C.; Smedskjaer, M. M.; Wondraczek, L. Looking into the Future of Hybrid Glasses. *Nature Chemistry* **2024**, *16* (11), 1755–1766. <https://doi.org/10.1038/s41557-024-01616-8>.
- (40) Lu, W.; Wei, Z.; Gu, Z.-Y.; Liu, T.-F.; Park, J.; Park, J.; Tian, J.; Zhang, M.; Zhang, Q.; Iii, T. G.; Bosch, M.; Zhou, H.-C. Tuning the Structure and Function of Metal–Organic Frameworks via Linker Design. *Chemical Society Reviews* **2014**, *43* (16), 5561–5593. <https://doi.org/10.1039/C4CS00003J>.
- (41) Yaghi, O. M.; O’Keeffe, M.; Ockwig, N. W.; Chae, H. K.; Eddaoudi, M.; Kim, J. Reticular Synthesis and the Design of New Materials. *Nature* **2003**, *423* (6941), 705–714. <https://doi.org/10.1038/nature01650>.
- (42) Wang, H.; Li, J. Microporous Metal–Organic Frameworks for Adsorptive Separation of C5–C6 Alkane Isomers. *Accounts of Chemical Research* **2019**, *52* (7), 1968–1978. <https://doi.org/10.1021/acs.accounts.8b00658>.
- (43) Guillerm, V.; Eddaoudi, M. The Importance of Highly Connected Building Units in Reticular Chemistry: Thoughtful Design of Metal–Organic Frameworks. *Accounts of Chemical Research* **2021**, *54* (17), 3298–3312. <https://doi.org/10.1021/acs.accounts.1c00214>.
- (44) Berdichevsky, E. K.; Downing, V. A.; Hooper, R. W.; Butt, N. W.; McGrath, D. T.; Donnelly, L. J.; Michaelis, V. K.; Katz, M. J. Ultrahigh Size Exclusion Selectivity for Carbon Dioxide from Nitrogen/Methane in an Ultramicroporous Metal–Organic Framework. *Inorganic Chemistry* **2022**, *61* (20), 7970–7979. <https://doi.org/10.1021/acs.inorgchem.2c00608>.
- (45) Breck, D. W. *Zeolite Molecular Sieves: Structure, Chemistry, and Use*; R.E. Krieger: Malabar, 1984.
- (46) Smirnova, O.; Ojha, S.; De, A.; Schneemann, A.; Haase, F.; Knebel, A. Tiny Windows in Reticular Nanomaterials for Molecular Sieving Gas Separation Membranes. *Advanced Functional Materials* **2024**, *34* (43), 2306202. <https://doi.org/10.1002/adfm.202306202>.
- (47) Gu, Z.-Y.; Yang, C.-X.; Chang, N.; Yan, X.-P. Metal–Organic Frameworks for Analytical Chemistry: From Sample Collection to Chromatographic Separation. *Accounts of Chemical Research* **2012**, *45* (5), 734–745. <https://doi.org/10.1021/ar2002599>.

- (48) Oh, H.; Hirscher, M. Quantum Sieving for Separation of Hydrogen Isotopes Using MOFs. *European Journal of Inorganic Chemistry* **2016**, *2016* (27), 4278–4289. <https://doi.org/10.1002/ejic.201600253>.
- (49) Li, Y.; Wang, Y.; Fan, W.; Sun, D. Flexible Metal–Organic Frameworks for Gas Storage and Separation. *Dalton Transactions* **2022**, *51* (12), 4608–4618. <https://doi.org/10.1039/D1DT03842G>.
- (50) Li, H.; Wang, K.; Sun, Y.; Lollar, C. T.; Li, J.; Zhou, H.-C. Recent Advances in Gas Storage and Separation Using Metal–Organic Frameworks. *Materials Today* **2018**, *21* (2), 108–121. <https://doi.org/10.1016/j.mattod.2017.07.006>.
- (51) Yan, C.; Jin, J.; Wang, J.; Zhang, F.; Tian, Y.; Liu, C.; Zhang, F.; Cao, L.; Zhou, Y.; Han, Q. Metal–Organic Frameworks (MOFs) for the Efficient Removal of Contaminants from Water: Underlying Mechanisms, Recent Advances, Challenges, and Future Prospects. *Coordination Chemistry Reviews* **2022**, *468*, 214595. <https://doi.org/10.1016/j.ccr.2022.214595>.
- (52) Yan, X.; Li, P.; Song, X.; Li, J.; Ren, B.; Gao, S.; Cao, R. Recent Progress in the Removal of Mercury Ions from Water Based MOFs Materials. *Coordination Chemistry Reviews* **2021**, *443*, 214034. <https://doi.org/10.1016/j.ccr.2021.214034>.
- (53) A. Goetjen, T.; Liu, J.; Wu, Y.; Sui, J.; Zhang, X.; T. Hupp, J.; K. Farha, O. Metal–Organic Framework (MOF) Materials as Polymerization Catalysts: A Review and Recent Advances. *Chemical Communications* **2020**, *56* (72), 10409–10418. <https://doi.org/10.1039/D0CC03790G>.
- (54) Hao, M.; Qiu, M.; Yang, H.; Hu, B.; Wang, X. Recent Advances on Preparation and Environmental Applications of MOF-Derived Carbons in Catalysis. *Science of The Total Environment* **2021**, *760*, 143333. <https://doi.org/10.1016/j.scitotenv.2020.143333>.
- (55) Duman, F. D.; S. Forgan, R. Applications of Nanoscale Metal–Organic Frameworks as Imaging Agents in Biology and Medicine. *Journal of Materials Chemistry B* **2021**, *9* (16), 3423–3449. <https://doi.org/10.1039/D1TB00358E>.
- (56) Bunzen, H.; Jiráček, D. Recent Advances in Metal–Organic Frameworks for Applications in Magnetic Resonance Imaging. *ACS Applied Materials & Interfaces* **2022**, *14* (45), 50445–50462. <https://doi.org/10.1021/acsami.2c10272>.
- (57) Cao, J.; Li, X.; Tian, H. Metal-Organic Framework (MOF)-Based Drug Delivery. *Current Medicinal Chemistry* **2020**, *27* (35), 5949–5969. <https://doi.org/10.2174/0929867326666190618152518>.
- (58) Ibrahim, M.; Sabouni, R.; Husseini, G. A. Anti-Cancer Drug Delivery Using Metal Organic Frameworks (MOFs). *Current Medicinal Chemistry* **2017**, *24* (2), 193–214. <https://doi.org/10.2174/0929867323666160926151216>.
- (59) Dissegna, S.; Epp, K.; Heinz, W. R.; Kieslich, G.; Fischer, R. A. Defective Metal–Organic Frameworks. *Advanced Materials* **2018**, *30* (37), 1704501. <https://doi.org/10.1002/adma.201704501>.
- (60) McGuire, C. V.; Forgan, R. S. The Surface Chemistry of Metal–Organic Frameworks. *Chemical Communications* **2015**, *51* (25), 5199–5217. <https://doi.org/10.1039/C4CC04458D>.

- (61) Ling, S.; Slater, B. Dynamic Acidity in Defective UiO-66. *Chemical Science* **2016**, *7* (7), 4706–4712. <https://doi.org/10.1039/C5SC04953A>.
- (62) Ren, J.; Musyoka, N. M.; Langmi, H. W.; North, B. C.; Mathe, M.; Pang, W.; Wang, M.; Walker, J. In-Situ IR Monitoring of the Formation of Zr-Fumarate MOF. *Applied Surface Science* **2017**, *404*, 263–267. <https://doi.org/10.1016/j.apsusc.2017.01.271>.
- (63) Daliran, S.; Reza Oveisi, A.; Kung, C.-W.; Sen, U.; Dhakshinamoorthy, A.; Chuang, C.-H.; Khajeh, M.; Erkartal, M.; T. Hupp, J. Defect-Enabling Zirconium-Based Metal–Organic Frameworks for Energy and Environmental Remediation Applications. *Chemical Society Reviews* **2024**, *53* (12), 6244–6294. <https://doi.org/10.1039/D3CS01057K>.
- (64) Li, S.; Han, W.; An, Q.-F.; Yong, K.-T.; Yin, M.-J. Defect Engineering of MOF-Based Membrane for Gas Separation. *Advanced Functional Materials* **2023**, *33* (38), 2303447. <https://doi.org/10.1002/adfm.202303447>.
- (65) Canivet, J.; Vandichel, M.; Farrusseng, D. Origin of Highly Active Metal–Organic Framework Catalysts: Defects? Defects! *Dalton Transactions* **2016**, *45* (10), 4090–4099. <https://doi.org/10.1039/C5DT03522H>.
- (66) Fang, Z.; Bueken, B.; De Vos, D. E.; Fischer, R. A. Defect-Engineered Metal–Organic Frameworks. *Angewandte Chemie International Edition* **2015**, *54* (25), 7234–7254. <https://doi.org/10.1002/anie.201411540>.
- (67) Feng, X.; Jena, H. S.; Krishnaraj, C.; Leus, K.; Wang, G.; Chen, H.; Jia, C.; Van Der Voort, P. Generating Catalytic Sites in UiO-66 through Defect Engineering. *ACS Applied Materials & Interfaces* **2021**, *13* (51), 60715–60735. <https://doi.org/10.1021/acsami.1c13525>.
- (68) Phan, P. T.; Hong, J.; Tran, N.; Le, T. H. The Properties of Microwave-Assisted Synthesis of Metal–Organic Frameworks and Their Applications. *Nanomaterials* **2023**, *13* (2), 352. <https://doi.org/10.3390/nano13020352>.
- (69) Araújo-Cordero, A. M.; Caddeo, F.; Mahmoudi, B.; Bron, M.; Wouter Maijenburg, A. Direct Electrochemical Synthesis of Metal-Organic Frameworks: Cu₃(BTC)₂ and Cu(TCPP) on Copper Thin Films and Copper-Based Microstructures. *ChemPlusChem* **2024**, *89* (3), e202300378. <https://doi.org/10.1002/cplu.202300378>.
- (70) Główniak, S.; Szczeńniak, B.; Choma, J.; Jaroniec, M. Mechanochemistry: Toward Green Synthesis of Metal–Organic Frameworks. *Materials Today* **2021**, *46*, 109–124. <https://doi.org/10.1016/j.mattod.2021.01.008>.
- (71) Vaitsis, C.; Sourkouni, G.; Argiris, C. Metal Organic Frameworks (MOFs) and Ultrasound: A Review. *Ultrasonics Sonochemistry* **2019**, *52*, 106–119. <https://doi.org/10.1016/j.ultsonch.2018.11.004>.
- (72) Al Obeidli, A.; Ben Salah, H.; Al Murisi, M.; Sabouni, R. Recent Advancements in MOFs Synthesis and Their Green Applications. *International Journal of Hydrogen Energy* **2022**, *47* (4), 2561–2593. <https://doi.org/10.1016/j.ijhydene.2021.10.180>.
- (73) Mondloch, J. E.; Karagiari, O.; Farha, O. K.; Hupp, J. T. Activation of Metal–Organic Framework Materials. *CrystEngComm* **2013**, *15* (45), 9258–9264. <https://doi.org/10.1039/C3CE41232F>.

- (74) Nelson, A. P.; Farha, O. K.; Mulfort, K. L.; Hupp, J. T. Supercritical Processing as a Route to High Internal Surface Areas and Permanent Microporosity in Metal–Organic Framework Materials. *Journal of the American Chemical Society* **2009**, *131* (2), 458–460. <https://doi.org/10.1021/ja808853q>.
- (75) Van Vleet, M. J.; Weng, T.; Li, X.; Schmidt, J. R. In Situ, Time-Resolved, and Mechanistic Studies of Metal–Organic Framework Nucleation and Growth. *Chemical Reviews* **2018**, *118* (7), 3681–3721. <https://doi.org/10.1021/acs.chemrev.7b00582>.
- (76) Jiang, D.; Huang, C.; Zhu, J.; Wang, P.; Liu, Z.; Fang, D. Classification and Role of Modulators on Crystal Engineering of Metal Organic Frameworks (MOFs). *Coordination Chemistry Reviews* **2021**, *444*, 214064. <https://doi.org/10.1016/j.ccr.2021.214064>.
- (77) Forgan, R. S. Modulated Self-Assembly of Metal–Organic Frameworks. *Chemical Science* **2020**, *11* (18), 4546–4562. <https://doi.org/10.1039/D0SC01356K>.
- (78) Diring, S.; Furukawa, S.; Takashima, Y.; Tsuruoka, T.; Kitagawa, S. Controlled Multiscale Synthesis of Porous Coordination Polymer in Nano/Micro Regimes. *Chemistry of Materials* **2010**, *22* (16), 4531–4538. <https://doi.org/10.1021/cm101778g>.
- (79) Atzori, C.; Shearer, G. C.; Maschio, L.; Civalleri, B.; Bonino, F.; Lamberti, C.; Svelle, S.; Lillerud, K. P.; Bordiga, S. Effect of Benzoic Acid as a Modulator in the Structure of UiO-66: An Experimental and Computational Study. *The Journal of Physical Chemistry C* **2017**, *121* (17), 9312–9324. <https://doi.org/10.1021/acs.jpcc.7b00483>.
- (80) Shearer, G. C.; Chavan, S.; Bordiga, S.; Svelle, S.; Olsbye, U.; Lillerud, K. P. Defect Engineering: Tuning the Porosity and Composition of the Metal–Organic Framework UiO-66 via Modulated Synthesis. *Chemistry of Materials* **2016**, *28* (11), 3749–3761. <https://doi.org/10.1021/acs.chemmater.6b00602>.
- (81) Ma, Y.; Li, A.; Wang, C. Experimental Study on Adsorption Removal of SO₂ in Flue Gas by Defective UiO-66. *Chemical Engineering Journal* **2023**, *455*, 140687. <https://doi.org/10.1016/j.cej.2022.140687>.
- (82) Semivrazhkaya, O. O.; Salionov, D.; Clark, A. H.; Casati, N. P. M.; Nachtegaal, M.; Ranocchiari, M.; Bjelić, S.; Verel, R.; van Bokhoven, J. A.; Sushkevich, V. L. Deciphering the Mechanism of Crystallization of UiO-66 Metal–Organic Framework. *Small* **2023**, *19* (52), 2305771. <https://doi.org/10.1002/sml.202305771>.
- (83) Salionov, D.; Semivrazhkaya, O. O.; Casati, N. P. M.; Ranocchiari, M.; Bjelić, S.; Verel, R.; van Bokhoven, J. A.; Sushkevich, V. L. Unraveling the Molecular Mechanism of MIL-53(Al) Crystallization. *Nature Communications* **2022**, *13* (1), 3762. <https://doi.org/10.1038/s41467-022-31294-4>.
- (84) Murphy, O. P.; Vashishtha, M.; Palanisamy, P.; Kumar, K. V. A Review on the Adsorption Isotherms and Design Calculations for the Optimization of Adsorbent Mass and Contact Time. *ACS Omega* **2023**, *8* (20), 17407–17430. <https://doi.org/10.1021/acsomega.2c08155>.

- (85) Brunauer, S.; Emmett, P. H.; Teller, E. Adsorption of Gases in Multimolecular Layers. *Journal of the American Chemical Society* **1938**, *60* (2), 309–319. <https://doi.org/10.1021/ja01269a023>.
- (86) Lowell, S.; Shields, J. E.; Thomas, M. A.; Thommes, M. Adsorption Mechanism. In *Characterization of Porous Solids and Powders: Surface Area, Pore Size and Density*; Lowell, S., Shields, J. E., Thomas, M. A., Thommes, M., Eds.; Springer Netherlands: Dordrecht, 2004; pp 15–57. https://doi.org/10.1007/978-1-4020-2303-3_4.
- (87) Rouquerol, J.; Rouquerol, F.; Llewellyn, P.; Maurin, G.; Sing, K. *Adsorption by Powders and Porous Solids*, 2nd ed.; Academic Press: New York, 2013.
- (88) Landers, J.; Gor, G. Yu.; Neimark, A. V. Density Functional Theory Methods for Characterization of Porous Materials. *Colloids and Surfaces A: Physicochemical and Engineering Aspects* **2013**, *437*, 3–32. <https://doi.org/10.1016/j.colsurfa.2013.01.007>.
- (89) Haouas, M.; Volkringer, C.; Loiseau, T.; Férey, G.; Taulelle, F. In Situ NMR, Ex Situ XRD and SEM Study of the Hydrothermal Crystallization of Nanoporous Aluminum Trimesates MIL-96, MIL-100, and MIL-110. *Chemistry of Materials* **2012**, *24* (13), 2462–2471. <https://doi.org/10.1021/cm300439e>.
- (90) Cravillon, J.; Nayuk, R.; Springer, S.; Feldhoff, A.; Huber, K.; Wiebcke, M. Controlling Zeolitic Imidazolate Framework Nano- and Microcrystal Formation: Insight into Crystal Growth by Time-Resolved In Situ Static Light Scattering. *Chemistry of Materials* **2011**, *23* (8), 2130–2141. <https://doi.org/10.1021/cm103571y>.
- (91) Shöâè, M.; Agger, J. R.; Anderson, M. W.; Attfield, M. P. Crystal Form, Defects and Growth of the Metal Organic Framework HKUST-1 Revealed by Atomic Force Microscopy. *CrystEngComm* **2008**, *10* (6), 646. <https://doi.org/10.1039/b718890k>.
- (92) Xu, H.; Sommer, S.; Broge, N. L. N.; Gao, J.; Iversen, B. B. The Chemistry of Nucleation: In Situ Pair Distribution Function Analysis of Secondary Building Units During UiO-66 MOF Formation. *Chemistry – A European Journal* **2019**, *25* (8), 2051–2058. <https://doi.org/10.1002/chem.201805024>.
- (93) Zavorotynska, O.; Åsland, A. C.; Dietzel, P. D. C.; Chavan, S. M. Exploring Cluster Formation in Zr-MOF Synthesis in Situ Using X-Ray Absorption Spectroscopy. *Physical Chemistry Chemical Physics* **2024**, *26* (42), 27019–27033. <https://doi.org/10.1039/D4CP01979B>.
- (94) Embrechts, H.; Kriesten, M.; Hoffmann, K.; Peukert, W.; Hartmann, M.; Distaso, M. Elucidation of the Formation Mechanism of Metal–Organic Frameworks via in-Situ Raman and FTIR Spectroscopy under Solvothermal Conditions. *The Journal of Physical Chemistry C* **2018**, *122* (23), 12267–12278. <https://doi.org/10.1021/acs.jpcc.8b02484>.
- (95) Günther, H. *NMR Spectroscopy: Basic Principles, Concepts and Applications in Chemistry*, 3rd ed.; John Wiley & Sons: Weinheim, Germany, 2013.
- (96) Jones, C. L.; Hughes, C. E.; Yeung, H. H.-M.; Paul, A.; Harris, K. D. M.; Easun, T. L. Exploiting in Situ NMR to Monitor the Formation of a Metal–Organic

- Framework. *Chemical Science* **2021**, *12* (4), 1486–1494. <https://doi.org/10.1039/D0SC04892E>.
- (97) Leger, M. E.; Guo, J.; MacMillan, B.; Titi, H. M.; Friščić, T.; Balcom, B.; Blight, B. A. In Situ Monitoring of Mechanochemical MOF Formation by NMR Relaxation Time Correlation. *Physical Chemistry Chemical Physics* **2023**, *26* (1), 543–550. <https://doi.org/10.1039/D3CP05555H>.
- (98) Cambridge Crystallographic Data Centre. Cambridge Structural Database. <https://library.bath.ac.uk/chemistry-software/ccdc> (accessed 2024-06-30).
- (99) Katz, M. J.; Brown, Z. J.; Colón, Y. J.; Siu, P. W.; Scheidt, K. A.; Snurr, R. Q.; Hupp, J. T.; Farha, O. K. A Facile Synthesis of UiO-66, UiO-67 and Their Derivatives. *Chemical Communications* **2013**, *49* (82), 9449–9451. <https://doi.org/10.1039/C3CC46105J>.
- (100) Schaate, A.; Roy, P.; Godt, A.; Lippke, J.; Waltz, F.; Wiebcke, M.; Behrens, P. Modulated Synthesis of Zr-Based Metal–Organic Frameworks: From Nano to Single Crystals. *Chemistry – A European Journal* **2011**, *17* (24), 6643–6651. <https://doi.org/10.1002/chem.201003211>.
- (101) Audu, C. O.; Nguyen, H. G. T.; Chang, C.-Y.; Katz, M. J.; Mao, L.; Farha, O. K.; Hupp, J. T.; Nguyen, S. T. The Dual Capture of AsV and AsIII by UiO-66 and Analogues. *Chemical Science* **2016**, *7* (10), 6492–6498. <https://doi.org/10.1039/C6SC00490C>.
- (102) Cliffe, M. J.; Wan, W.; Zou, X.; Chater, P. A.; Kleppe, A. K.; Tucker, M. G.; Wilhelm, H.; Funnell, N. P.; Coudert, F.-X.; Goodwin, A. L. Correlated Defect Nanoregions in a Metal–Organic Framework. *Nature Communications* **2014**, *5* (1), 4176. <https://doi.org/10.1038/ncomms5176>.
- (103) Han, Y.; Liu, M.; Li, K.; Zuo, Y.; Wei, Y.; Xu, S.; Zhang, G.; Song, C.; Zhang, Z.; Guo, X. Facile Synthesis of Morphology and Size-Controlled Zirconium Metal–Organic Framework UiO-66: The Role of Hydrofluoric Acid in Crystallization. *CrystEngComm* **2015**, *17* (33), 6434–6440. <https://doi.org/10.1039/C5CE00729A>.
- (104) Kaur, G.; Øien-Ødegaard, S.; Lazzarini, A.; Chavan, S. M.; Bordiga, S.; Lillerud, K. P.; Olsbye, U. Controlling the Synthesis of Metal–Organic Framework UiO-67 by Tuning Its Kinetic Driving Force. *Crystal Growth & Design* **2019**, *19* (8), 4246–4251. <https://doi.org/10.1021/acs.cgd.9b00916>.
- (105) Taddei, M.; Dümbgen, K. C.; Bokhoven, J. A. van; Ranocchiari, M. Aging of the Reaction Mixture as a Tool to Modulate the Crystallite Size of UiO-66 into the Low Nanometer Range. *Chemical Communications* **2016**, *52* (38), 6411–6414. <https://doi.org/10.1039/C6CC02517J>.
- (106) Kubo, M.; Miyoshi, Y.; Uchitomi, Y.; Shimada, M. Insights into the Spray Synthesis of UiO-66 and UiO-66-NH₂ Metal–Organic Frameworks: Effect of Zirconium Precursors and Process Parameters. *Crystals* **2024**, *14* (2), 116. <https://doi.org/10.3390/cryst14020116>.
- (107) Semrau, A. L.; Wannapaiboon, S.; Pujari, S. P.; Vervoorts, P.; Albada, B.; Zuilhof, H.; Fischer, R. A. Highly Porous Nanocrystalline UiO-66 Thin Films via Coordination Modulation Controlled Step-by-Step Liquid-Phase Growth. *Crystal*

- Growth & Design* **2019**, *19* (3), 1738–1747. <https://doi.org/10.1021/acs.cgd.8b01719>.
- (108) Bigdeli, F.; A. Fetzer, M. N.; Nis, B.; Morsali, A.; Janiak, C. Coordination Modulation: A Way to Improve the Properties of Metal–Organic Frameworks. *Journal of Materials Chemistry A* **2023**, *11* (41), 22105–22131. <https://doi.org/10.1039/D3TA03077F>.
- (109) Berenjian, N.; Utley, J. H. P. Leaving Group Abilities for the Cathodic Cleavage of P-Methoxycarbonylbenzyl Carboxylates. *Journal of the Chemical Society, Chemical Communications* **1979**, No. 12, 550–551. <https://doi.org/10.1039/C39790000550>.
- (110) Burrows, A. D.; Cassar, K.; Düren, T.; Friend, R. M. W.; Mahon, M. F.; Rigby, S. P.; Savarese, T. L. Syntheses, Structures and Properties of Cadmium Benzenedicarboxylate Metal–Organic Frameworks. *Dalton Transactions* **2008**, No. 18, 2465–2474. <https://doi.org/10.1039/B718947H>.
- (111) Wilkins, R. G. Substitution Reactions. In *Kinetics and Mechanism of Reactions of Transition Metal Complexes*; John Wiley & Sons, Ltd, 1991; pp 212–213. <https://doi.org/10.1002/3527600825.ch4>.
- (112) Lázaro, I. A. A Comprehensive Thermogravimetric Analysis Multifaceted Method for the Exact Determination of the Composition of Multifunctional Metal-Organic Framework Materials. *European Journal of Inorganic Chemistry* **2020**, *2020* (45), 4284–4294. <https://doi.org/10.1002/ejic.202000656>.
- (113) D. Gamelas, S. R.; C. Tomé, J. P.; C. Tomé, A.; O. Lourenço, L. M. Advances in Photocatalytic Degradation of Organic Pollutants in Wastewaters: Harnessing the Power of Phthalocyanines and Phthalocyanine-Containing Materials. *RSC Advances* **2023**, *13* (48), 33957–33993. <https://doi.org/10.1039/D3RA06598G>.
- (114) Grant, T. M.; Josey, D. S.; Sampson, K. L.; Mudigonda, T.; Bender, T. P.; Lessard, B. H. Boron Subphthalocyanines and Silicon Phthalocyanines for Use as Active Materials in Organic Photovoltaics. *The Chemical Record* **2019**, *19* (6), 1093–1112. <https://doi.org/10.1002/tcr.201800178>.
- (115) Lo, P.-C.; Rodríguez-Morgade, M. S.; Pandey, R. K.; Ng, D. K. P.; Torres, T.; Dumoulin, F. The Unique Features and Promises of Phthalocyanines as Advanced Photosensitisers for Photodynamic Therapy of Cancer. *Chemical Society Reviews* **2020**, *49* (4), 1041–1056. <https://doi.org/10.1039/C9CS00129H>.
- (116) de Siqueira, L. B. de O.; dos Santos Matos, A. P.; da Silva, M. R. M.; Pinto, S. R.; Santos-Oliveira, R.; Ricci-Júnior, E. Pharmaceutical Nanotechnology Applied to Phthalocyanines for the Promotion of Antimicrobial Photodynamic Therapy: A Literature Review. *Photodiagnosis and Photodynamic Therapy* **2022**, *39*, 102896. <https://doi.org/10.1016/j.pdpdt.2022.102896>.
- (117) Higgs, P. L.; McKinley, A. W.; Tuite, E. M. [Ru(Phen)₂ Dppz]²⁺ Luminescence Reveals Nanoscale Variation of Polarity in the Cyclodextrin Cavity. *Chemical Communications* **2016**, *52* (9), 1883–1886. <https://doi.org/10.1039/C5CC09755J>.
- (118) Holliman, P. J.; Mohsen, M.; Connell, A.; Davies, M. L.; Al-Salihi, K.; Pitak, M. B.; Tizzard, G. J.; Coles, S. J.; Harrington, R. W.; Clegg, W.; Serpa, C.; Fontes, O. H.; Charbonneau, C.; Carnie, M. J. Ultra-Fast Co-Sensitization and Tri-Sensitization

- of Dye-Sensitized Solar Cells with N719, SQ1 and Triarylamine Dyes. *Journal of Materials Chemistry* **2012**, *22* (26), 13318–13327. <https://doi.org/10.1039/C2JM31314F>.
- (119) Bezzu, C. G.; Helliwell, M.; Warren, J. E.; Allan, D. R.; McKeown, N. B. Heme-Like Coordination Chemistry Within Nanoporous Molecular Crystals. *Science* **2010**, *327* (5973), 1627–1630. <https://doi.org/10.1126/science.1184228>.
- (120) Abdelhameed, R. M.; El-Shahat, M.; Abd El-Ghaffar, M. A. Boosting the Photocatalytic Activity of Ti-MOF via Emerging with Metal Phthalocyanine to Degrade Hazard Textile Pigments. *Journal of Alloys and Compounds* **2022**, *896*, 162992. <https://doi.org/10.1016/j.jallcom.2021.162992>.
- (121) Dong, A.; Lin, Y.; Guo, Y.; Chen, D.; Wang, X.; Ge, Y.; Li, Q.; Qian, J. Immobilization of Iron Phthalocyanine on MOF-Derived N-Doped Carbon for Promoting Oxygen Reduction in Zinc-Air Battery. *Journal of Colloid and Interface Science* **2023**, *650*, 2056–2064. <https://doi.org/10.1016/j.jcis.2023.06.043>.
- (122) Zhao, X.; Jia, J.; Shi, H.; Li, S.; Xu, C. Strong Electronic Interaction Enhanced Electrocatalysis of Copper Phthalocyanine Decorated Co-MOF-74 toward Highly Efficient Oxygen Evolution Reaction. *RSC Advances* **2024**, *14* (54), 40173–40178. <https://doi.org/10.1039/D4RA05547K>.
- (123) Jia, H.; Yao, Y.; Zhao, J.; Gao, Y.; Luo, Z.; Du, P. A Novel Two-Dimensional Nickel Phthalocyanine-Based Metal–Organic Framework for Highly Efficient Water Oxidation Catalysis. *Journal of Materials Chemistry A* **2018**, *6* (3), 1188–1195. <https://doi.org/10.1039/C7TA07978H>.
- (124) Zhuge, W.; Liu, Y.; Huang, W.; Zhang, C.; Wei, L.; Peng, J. Conductive 2D Phthalocyanine-Based Metal–Organic Framework as a Photoelectrochemical Sensor for N-Acetyl-L-Cysteine Detection. *Sensors and Actuators B: Chemical* **2022**, *367*, 132028. <https://doi.org/10.1016/j.snb.2022.132028>.
- (125) Yi, J.-D.; Si, D.-H.; Xie, R.; Yin, Q.; Zhang, M.-D.; Wu, Q.; Chai, G.-L.; Huang, Y.-B.; Cao, R. Conductive Two-Dimensional Phthalocyanine-Based Metal–Organic Framework Nanosheets for Efficient Electroreduction of CO₂. *Angewandte Chemie* **2021**, *133* (31), 17245–17251. <https://doi.org/10.1002/ange.202104564>.
- (126) Chen, G.; Li, Z.; Huang, Z.; Lu, H.; Long, G.; Lezama Pacheco, J. S.; Tok, J. B.-H.; Gao, T. Z.; Lei, Y.; Zhou, J.; Bao, Z. Effects of Transition Metals on Metal–Octaaminophthalocyanine-Based 2D Metal–Organic Frameworks. *ACS Nano* **2023**, *17* (10), 9611–9621. <https://doi.org/10.1021/acsnano.3c03143>.
- (127) Wang, M.; Shi, H.; Zhang, P.; Liao, Z.; Wang, M.; Zhong, H.; Schwotzer, F.; Nia, A. S.; Zschech, E.; Zhou, S.; Kaskel, S.; Dong, R.; Feng, X. Phthalocyanine-Based 2D Conjugated Metal–Organic Framework Nanosheets for High-Performance Micro-Supercapacitors. *Advanced Functional Materials* **2020**, *30* (30), 2002664. <https://doi.org/10.1002/adfm.202002664>.
- (128) Nagatomi, H.; Yanai, N.; Yamada, T.; Shiraishi, K.; Kimizuka, N. Synthesis and Electric Properties of a Two-Dimensional Metal–Organic Framework Based on Phthalocyanine. *Chemistry – A European Journal* **2018**, *24* (8), 1806–1810. <https://doi.org/10.1002/chem.201705530>.

- (129) Zhong, H.; Ly, K. H.; Wang, M.; Krupskaya, Y.; Han, X.; Zhang, J.; Zhang, J.; Kataev, V.; Büchner, B.; Weidinger, I. M.; Kaskel, S.; Liu, P.; Chen, M.; Dong, R.; Feng, X. A Phthalocyanine-Based Layered Two-Dimensional Conjugated Metal–Organic Framework as a Highly Efficient Electrocatalyst for the Oxygen Reduction Reaction. *Angewandte Chemie International Edition* **2019**, *58* (31), 10677–10682. <https://doi.org/10.1002/anie.201907002>.
- (130) Ding, X.; Feng, X.; Saeki, A.; Seki, S.; Nagai, A.; Jiang, D. Conducting Metallophthalocyanine 2D Covalent Organic Frameworks: The Role of Central Metals in Controlling π -Electronic Functions. *Chemical Communications* **2012**, *48* (71), 8952–8954. <https://doi.org/10.1039/C2CC33929C>.
- (131) Matheu, R.; Gutierrez-Puebla, E.; Monge, M. Á.; Diercks, C. S.; Kang, J.; Prévot, M. S.; Pei, X.; Hanikel, N.; Zhang, B.; Yang, P.; Yaghi, O. M. Three-Dimensional Phthalocyanine Metal-Catecholates for High Electrochemical Carbon Dioxide Reduction. *Journal of the American Chemical Society* **2019**, *141* (43), 17081–17085. <https://doi.org/10.1021/jacs.9b09298>.
- (132) Shayan, M. The Synthesis of Shape-Persistent Macrocycles Towards the Rational Design of Stable Large- Pore Metal-Organic Frameworks. PhD, Memorial University of Newfoundland, St. John’s, NL, 2021.
- (133) Donovan, J. C.; Wright, K. R.; Matzger, A. J. Validation and Mechanistic Studies of the Headspace Effect in MOF Synthesis. *Angewandte Chemie International Edition* **64** (12), e202500531. <https://doi.org/10.1002/anie.202500531>.
- (134) Zahn, G.; Zerner, P.; Lippke, J.; L. Kempf, F.; Lilienthal, S.; A. Schröder, C.; M. Schneider, A.; Behrens, P. Insight into the Mechanism of Modulated Syntheses: In Situ Synchrotron Diffraction Studies on the Formation of Zr-Fumarate MOF. *CrystEngComm* **2014**, *16* (39), 9198–9207. <https://doi.org/10.1039/C4CE01095G>.
- (135) Wang, T. C.; Vermeulen, N. A.; Kim, I. S.; Martinson, A. B. F.; Stoddart, J. F.; Hupp, J. T.; Farha, O. K. Scalable Synthesis and Post-Modification of a Mesoporous Metal-Organic Framework Called NU-1000. *Nature Protocols* **2016**, *11* (1), 149–162. <https://doi.org/10.1038/nprot.2016.001>.
- (136) Hisaki, I.; Xin, C.; Takahashi, K.; Nakamura, T. Designing Hydrogen-Bonded Organic Frameworks (HOFs) with Permanent Porosity. *Angewandte Chemie International Edition* **2019**, *58* (33), 11160–11170. <https://doi.org/10.1002/anie.201902147>.
- (137) Colón, Y. J.; Gómez-Gualdrón, D. A.; Snurr, R. Q. Topologically Guided, Automated Construction of Metal–Organic Frameworks and Their Evaluation for Energy-Related Applications. *Crystal Growth & Design* **2017**, *17* (11), 5801–5810. <https://doi.org/10.1021/acs.cgd.7b00848>.
- (138) Koschnick, C.; Stäglich, R.; Scholz, T.; Terban, M. W.; von Mankowski, A.; Savasci, G.; Binder, F.; Schökel, A.; Etter, M.; Nuss, J.; Siegel, R.; Germann, L. S.; Ochsenfeld, C.; Dinnebier, R. E.; Senker, J.; Lotsch, B. V. Understanding Disorder and Linker Deficiency in Porphyrinic Zirconium-Based Metal–Organic Frameworks by Resolving the Zr_8O_6 Cluster Conundrum in PCN-221. *Nature Communications* **2021**, *12* (1), 3099. <https://doi.org/10.1038/s41467-021-23348-w>.

- (139) Ding, M.; Cai, X.; Jiang, H.-L. Improving MOF Stability: Approaches and Applications. *Chemical Science* **2019**, *10* (44), 10209–10230. <https://doi.org/10.1039/C9SC03916C>.

Appendix A

A.1 Peak width fits for UiO-66-BA

The time-resolved D₂O peak width data for the standard synthesis of UiO-66-BA appeared to be comprised of two peaks, so the data was fitted to a model of two Gaussian peaks in order to determine the parameters of each peak using the program fity.

Gaussian:

$$y = a_0 \exp \left[-\ln(2) \left(\frac{x - a_1}{a_2} \right)^2 \right] + b_0 \exp \left[-\ln(2) \left(\frac{x - b_1}{b_2} \right)^2 \right]$$

Where a_0 is the height of the peak, a_1 is the center of the peak, and a_2 is the half width at half maximum (HWHM = FWHM/2). The completed formula for the fit used is as follows:

$$y = 69 \cdot \exp \left[-\ln(2) \left(\frac{x - 171}{72} \right)^2 \right] + 15 \cdot \exp \left[-\ln(2) \left(\frac{x - 47}{29} \right)^2 \right]$$

Table A.1 Parameters and errors defining Gaussian fit for UiO-66-BA data.

	Height (a_0) (Hz)	Center (a_1) (min)	HWHM (a_2) (min)
Peak 1	69 ± 3	171 ± 3	72 ± 4
Peak 2	15 ± 4	47 ± 7	28 ± 8

A.2 Peak shift fits for UiO-66-HCl

The time-resolved D₂O peak shift data for UiO-66-HCl appeared to be comprised of two competing processes. The data was thus fitted to a mathematical model to show these processes. It should be noted that the equations chosen are not intended to have any chemical significance – they exist to demonstrate that the shape of the data can be explained if one supposes that two competing processes are taking places.

The equation chosen to describe these processes is as follows:

$$f = y_0 + (m \cdot x) + (a \cdot \exp[-b \cdot x]) - d^x$$

The D₂O shift data for DMF and HCl only appears to show one process for its initial region.

That process can be described with the equation:

$$f = 4.9896 + (0 \cdot x) + (0.268 \cdot \exp[-0.0975 \cdot x]) - 0^x$$

Table A.2 Parameters and errors for model describing D₂O shift of DMF+HCl.

y_0 (ppm)	a (ppm)	b (min ⁻¹)	d	m (ppm/min)
4.9896 ± 0.0011	0.268 ± 0.002	0.0975 ± 0.0017	-	-

The D₂O shift data for ZrCl₄, DMF, and HCl shows two competing processes. They can be described with the following equations:

$$1) f = y_0 + (m \cdot x) + (a \cdot \exp[-b \cdot x])$$

$$f = 5.601 + (-0.00407 \cdot x) + (0.597 \cdot \exp[-0.0928 \cdot x])$$

$$2) f = y_0 - d^x$$

$$f = 5.601 - 0.9850^x$$

These two equations combine to give:

$$f = 5.601 + (-0.00407 \cdot x) + (0.597 \cdot \exp[-0.0928 \cdot x]) - 0.9850^x$$

Table A.3 Parameters and errors for model describing D₂O shift of ZrCl₄, DMF, and HCl.

y ₀ (ppm)	a (ppm)	b (min ⁻¹)	d	m (ppm/min)
5.601 ±	0.597 ±	0.0928 ±	0.9850 ±	-0.00407 ±
0.058	0.057	0.0076	0.0022	0.00010

The D₂O shift data for the standard synthesis of UiO-66-HCl shows two competing processes. They can be described with the following equations:

$$1) f = y_0 + (m \cdot x) + (a \cdot \exp[-b \cdot x])$$

$$f = 5.392 + (-0.0012 \cdot x) + (0.964 \cdot \exp[-0.0779 \cdot x])$$

$$2) f = y_0 - d^x$$

$$f = 5.392 - 0.9530^x$$

These two equations combine to give:

$$f = 5.392 + (-0.0012 \cdot x) + (0.964 \cdot \exp[-0.0779 \cdot x]) - 0.9530^x$$

Table A.4 Parameters and errors for model describing D₂O shift of standard synthesis UiO-66-HCl.

y ₀ (ppm)	a (ppm)	b (min ⁻¹)	d	m (ppm/min)
5.392 ± 0.035	0.964 ± 0.036	0.0779 ± 0.0025	0.9530 ± 0.0037	-0.0012 ± 0.0004

Appendix B

B.1 Rate order of standard synthesis

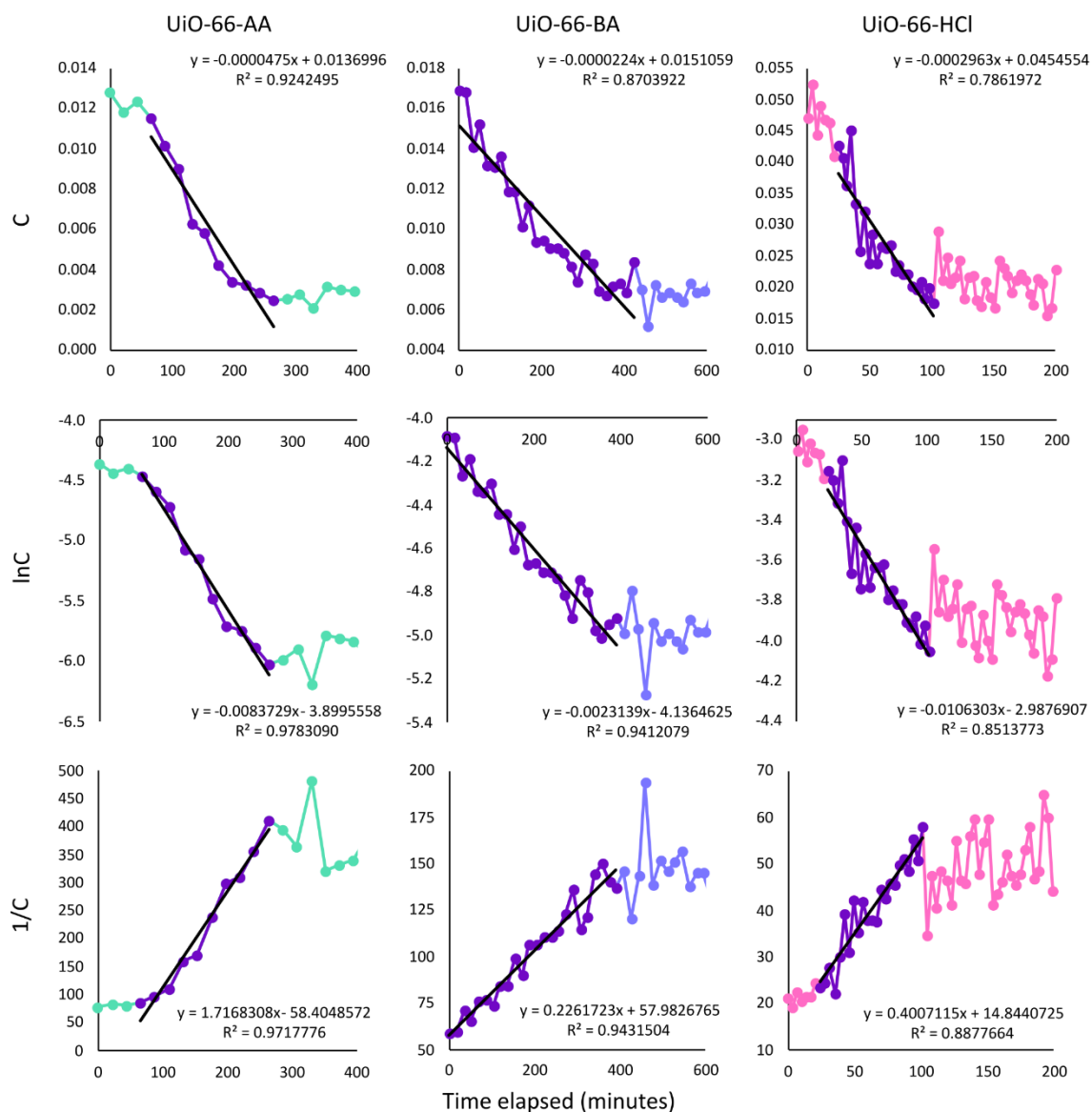


Figure B.1 Rate order graphs of the concentration of ligand in solution over time during the standard synthesis of UiO-66.

B.2 Rate order of synthesis with pre-conditioned DMF and modulator

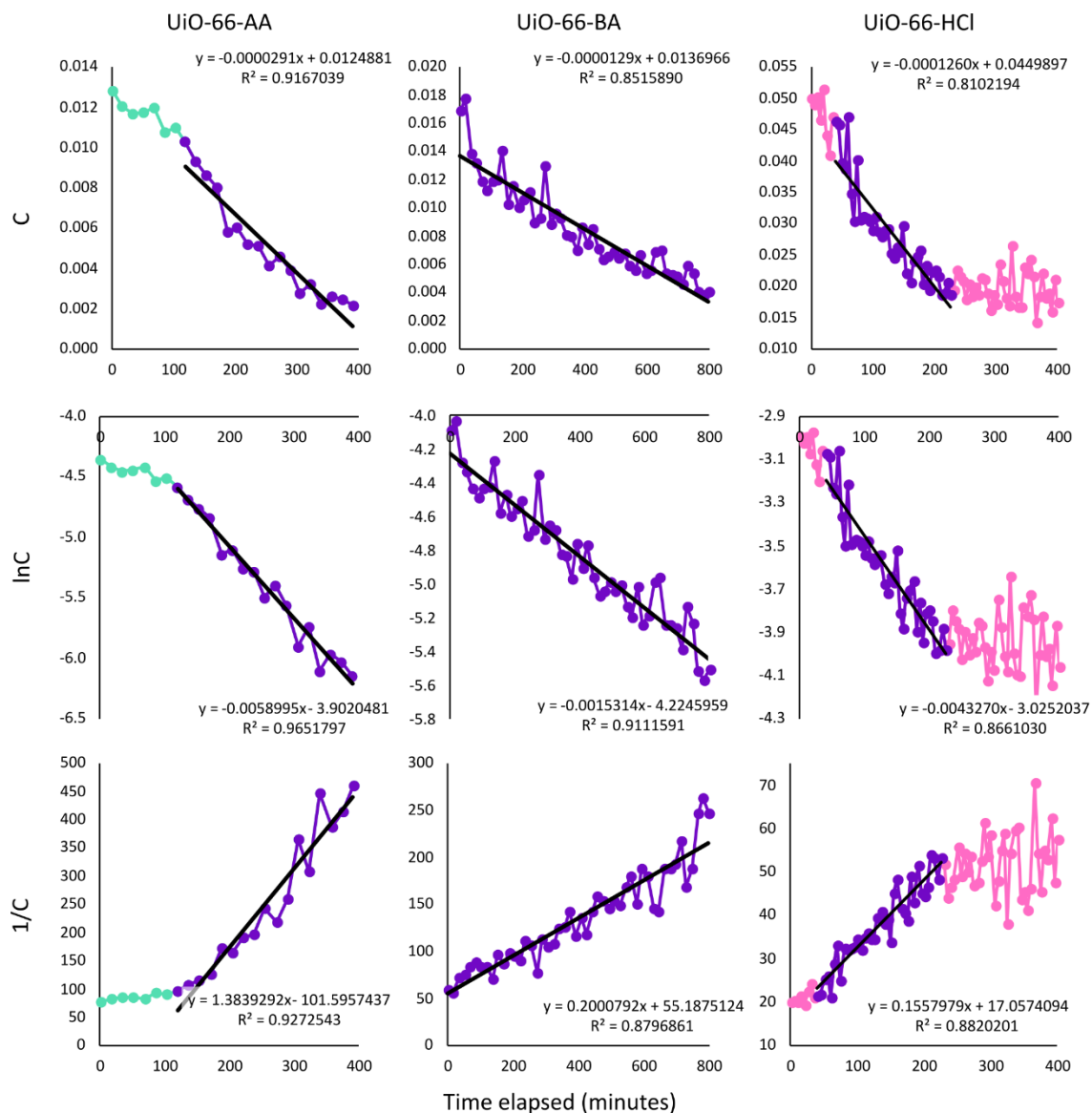


Figure B.2 Rate order graphs of the concentration of ligand in solution over time during the synthesis of UiO-66 using pre-conditioned DMF and modulator.

B.3 Rate order of synthesis with pre-conditioned $ZrCl_4$ in DMF and modulator

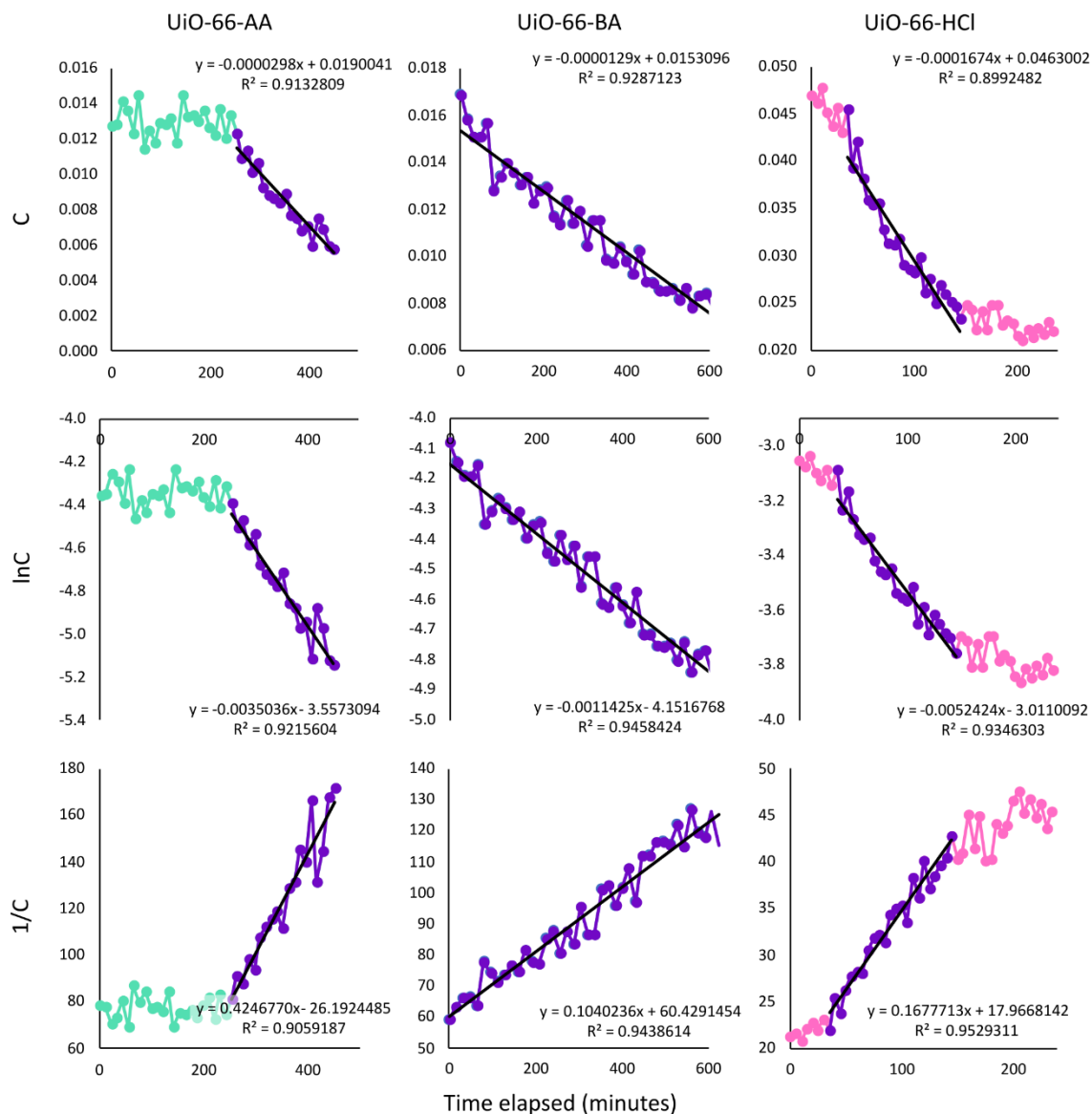
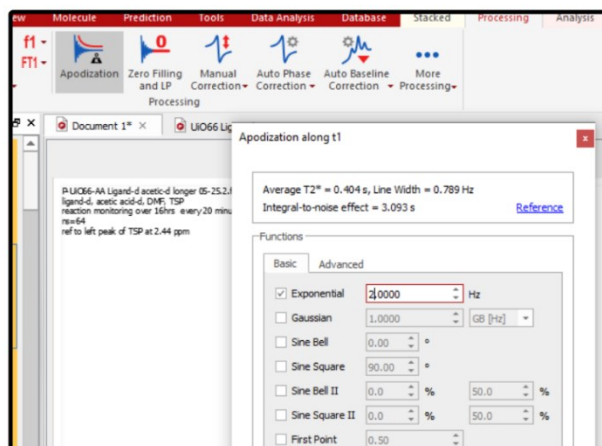


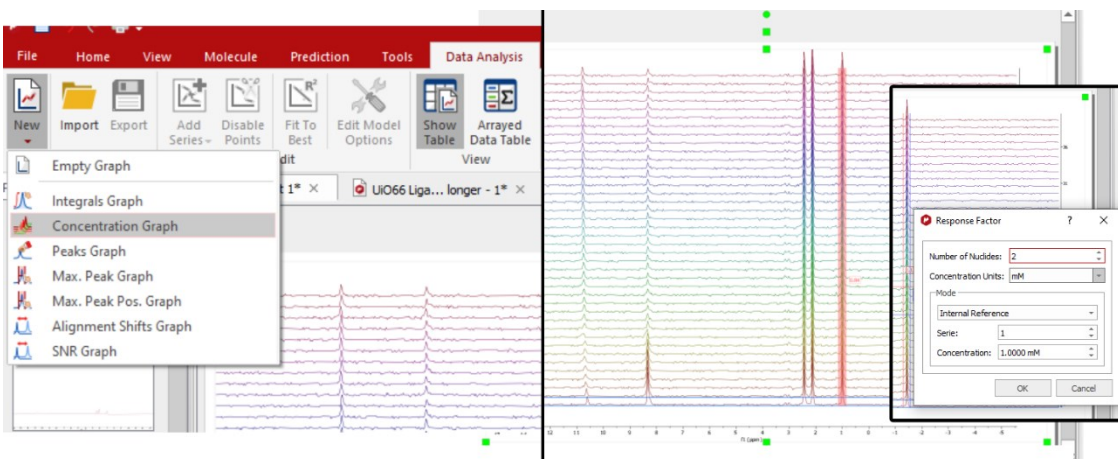
Figure B.3 Rate order graphs of the concentration of ligand in solution over time during the synthesis of UiO-66 using pre-conditioned $ZrCl_4$ in DMF and modulator.

Appendix C

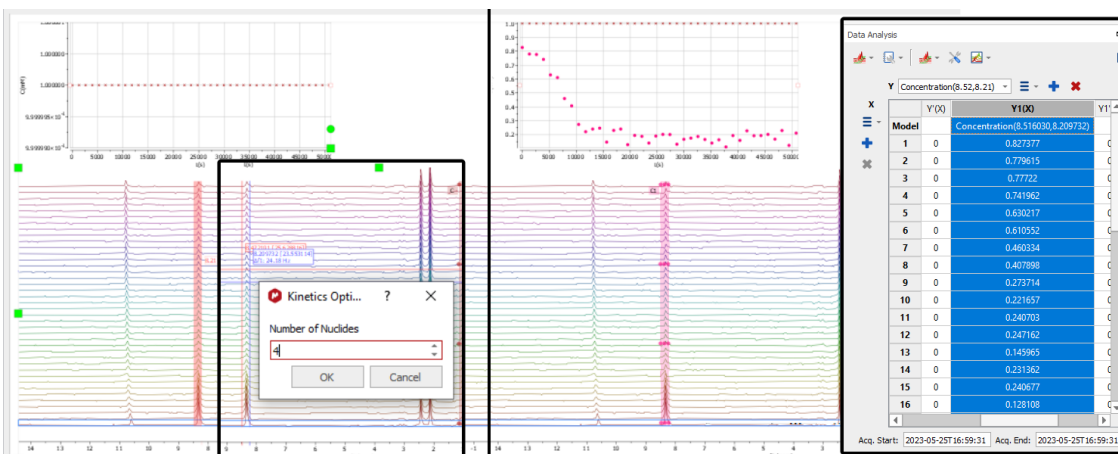
C.1 Process of applying $^2\text{H-NMR}$ to quantify linker concentration



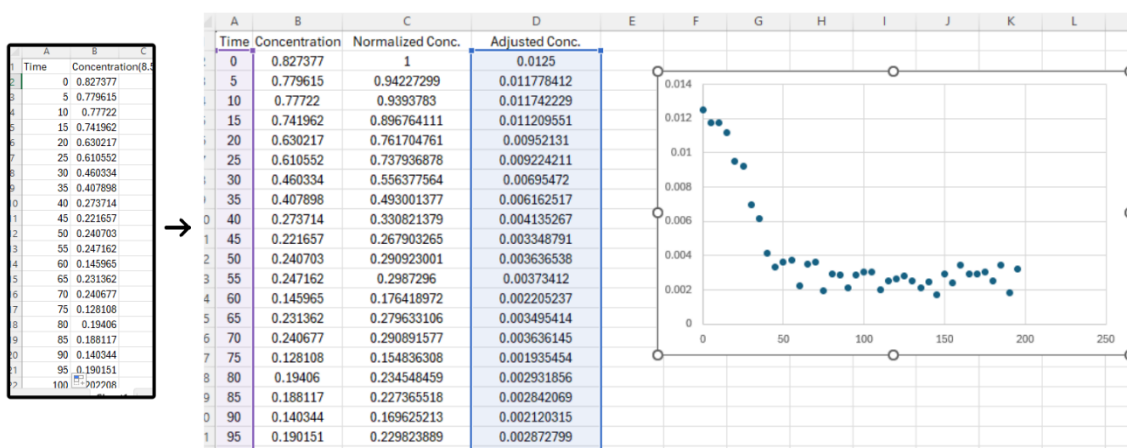
1. Spectra were imported into MestReNova, which had the Reaction Monitoring plugin installed. Typically, apodization with an Exponential value of 2.000 Hz was applied to all spectra. Spectra were then baseline corrected and phase corrected. Finally, the spectra were referenced to the leftmost peak from TMS- d_4 at 2.44 ppm, and then they were stacked.



2. From the stacked spectra, a new Concentration Graph was made. The first region selected contained the reference peak, which was typically the left TMSP- d_4 peak (which corresponded to 2 deuterons). If peaks from other compounds were present at a similar shift to the left peak of TMSP- d_4 (e.g., methyl deuterons from deuterated acetic acid), the right peak was used instead.



3. Then, the region containing the peak from the 4 linker deuterons was selected. The resulting data found in the Y1(X) column were then copied and pasted into Excel.



4. The corresponding time elapsed data were added to the concentration data points. For this work, the initial concentration of linker in solution at $t = 0$ was assumed to be equal to the calculated concentration of linker dissolved in solution at the start of the reaction (e.g., 0.0125 M for AA). The data were normalized and then scaled to fit the initial concentration.

Appendix D

D.1 Full LDI mass spectrum of BzPcLinker

